COOLING CURVE THERMAL ANALYSES AND OXYGEN ACTIVITY ANALYSES FOR THE ESTIMATION OF MICROSTRUCTURAL PROPERTIES OF NODULAR CAST IRON

A THESIS SUBMITTED TO
THE GRADUATE SCHOOL OF NATURAL AND APPLIED SCIENCES
OF
MIDDLE EAST TECHNICAL UNIVERSITY

BY
CANSIN ÇEHİZ

IN PARTIAL FULFILLMENT OF THE REQUIREMENTS
FOR
THE DEGREE OF MASTER OF SCIENCE
IN
METALLURGICAL AND MATERIALS ENGINEERING

JULY 2019

Approval of the thesis:

COOLING CURVE THERMAL ANALYSES AND OXYGEN ACTIVITY ANALYSES FOR THE ESTIMATION OF MICROSTRUCTURAL PROPERTIES OF NODULAR CAST IRON

submitted by **CANSIN ÇEHİZ** in partial fulfillment of the requirements for the degree of **Master of Science in Metallurgical and Materials Engineering Department, Middle East Technical University** by,

Prof. Dr. Halil Kalıpçılar
Dean, Graduate School of **Natural and Applied Sciences** _____

Prof. Dr. Cemil Hakan Gür
Head of Department, **Met. and Mat. Eng.** _____

Prof. Dr. Ali Kalkanlı
Supervisor, **Met. and Mat. Eng., METU** _____

Assist. Prof. Dr. Bilge İmer
Co-Supervisor, **Met. and Mat. Eng., METU** _____

Examining Committee Members:

Prof. Dr. Vedat Akdeniz
Met. and Mat. Eng., METU _____

Prof. Dr. Ali Kalkanlı
Met. and Mat. Eng., METU _____

Assist. Prof. Dr. Bilge İmer
Met. and Mat. Eng., METU _____

Assist. Prof. Dr. Batur Ercan
Met. and Mat. Eng., METU _____

Assist. Prof. Dr. Erkan Konca
Met. and Mat. Eng., Atılım University _____

Date: 26.07.2019

I hereby declare that all information in this document has been obtained and presented in accordance with academic rules and ethical conduct. I also declare that, as required by these rules and conduct, I have fully cited and referenced all material and results that are not original to this work.

Name, Surname: Cansın Çehiz

Signature:

ABSTRACT

COOLING CURVE THERMAL ANALYSES AND OXYGEN ACTIVITY ANALYSES FOR THE ESTIMATION OF MICROSTRUCTURAL PROPERTIES OF NODULAR CAST IRON

Çehiz, Cansın
Master of Science, Metallurgical and Materials Engineering
Supervisor: Prof. Dr. Ali Kalkanlı
Co-Supervisor: Assist. Prof. Dr. Bilge İmer

July 2019, 108 pages

Although nodular cast iron grades have mechanical properties competitive with plain carbon steel grades, they have advantage in terms of price due to relatively low raw material and energy costs. Therefore, they are widely used in various industries, especially in automotive, machinery, piping and wind power industries.

High number of process variables affecting the solidification behavior of nodular cast iron melt makes it difficult to ensure the resulting microstructure, thus the performance of nodular cast iron products. Cooling curve thermal analysis and oxygen activity analysis are two industrially applicable methods which are considered to have a potential of providing information on the solidification behavior of nodular cast iron melt.

In this study, chemical composition, cooling curve thermal analysis and oxygen activity analysis data were collected from the usual production process of Ferromatrix NV iron foundry in Kortrijk, Belgium. The collected samples were subjected to metallographic evaluation and tensile test in order to obtain data on the resulting microstructure and mechanical performance. The alloy EN-GJS-400-18 which is a ferritic nodular cast iron grade with high ductility, and the alloy EN-GJS-600-10C

which is a solution strengthened ferritic nodular cast iron grade with both high strength and high ductility were examined. By processing the collected data, conclusions on the relation of the parameters with each other and their variation between the two alloy grades and between different inoculant additions were done.

Keywords: Nodular Cast Iron, Cooling Curve, Thermal Analysis, Oxygen Activity

ÖZ

KÜRESEL GRAFİTLİ DÖKME DEMİRDE MİKROYAPISAL ÖZELLİKLERİN TAHMİNİNE YÖNELİK SOĞUMA EĞRİSİ ISIL ANALİZLERİ VE OKSİJEN AKTİVİTESİ ANALİZLERİ

Çehiz, Cansın
Yüksek Lisans, Metalurji ve Malzeme Mühendisliği
Tez Danışmanı: Prof. Dr. Ali Kalkanlı
Ortak Tez Danışmanı: Dr. Öğr. Üyesi Bilge İmer

Temmuz 2019, 108 sayfa

Küresel grafitli dökme demirler, yalın karbon çelikleriyle kıyaslanabilir mekanik özelliklerine karşın, nispeten düşük ham madde ve enerji maliyetleri sayesinde fiyat avantajı sağlamaktalar. Bu yüzden de, başta otomotiv, makina, tesisat ve rüzgar enerjisi sanayileri olmak üzere çeşitli alanlarda yaygın olarak kullanılmaktalar.

Küresel grafitli dökme demir ergiyiğinin katılaşma davranımını etkileyen proses değişkenlerinin çokluğu, sonuçta elde edilecek ürünün mikroyapısını, dolayısıyla da performansını kontrol altında tutmayı güçleştirmektedir. Soğuma eğrisi ısıl analizi ve oksijen aktivitesi analizi, küresel grafitli dökme demir ergiyiğinin katılaşma davranımı üzerine bilgi sağlama potansiyeli bulunan, sanayide kullanıma uygun analiz yöntemleridir.

Bu çalışmada, Kortrijk, Belçika'da bulunan Ferromatrix NV dökümhanesinin günlük üretim prosesinden kimyasal bileşim, soğuma eğrisi ısıl analizi ve oksijen aktivitesi analizi verileri toplanmıştır. Elde edilen numuneler metalografik inceleme ve çekme testine tabi tutularak sonuçta elde edilen mikroyapı ve mekanik performans üzerine veriler elde edilmiştir. Ferritik bir küresel grafitli dökme demir olan ve yüksek süneklik sağlayan EN-GJS-400-18 alaşımı ve katı çözelti sertleşmesiyle

mukavemetlendirilmiş ferritik bir küresel grafitli dökme demir olan ve yüksek mukavemet ve sünekliği bir arada sağlayan EN-GJS-600-10C alaşımı çalışma kapsamında incelendi. Elde edilen veriler doğrultusunda, parametrelerin birbirleriyle ilişkileri, iki alaşım tipi arasında ve farklı aşı ilaveleriyle gösterdikleri değişkenlikler hakkında çıkarımlar yapıldı.

Anahtar Kelimeler: Küresel Grafitli Dökme Demir, Soğuma Eğrisi, Isıl Analiz, Oksijen Aktivitesi

To cast iron, the well-known material with lots of unknowns…

ACKNOWLEDGEMENTS

The study which is the subject of this thesis was conducted at the Department of Metallurgical and Materials Engineering of Middle East Technical University, at my employer Heraeus Electro-Nite Intl. NV and at the foundry Ferromatrix NV.

Firstly, I am grateful to Graduate School of Natural and Applied Sciences and the Department of Metallurgical and Materials Engineering of Middle East Technical University for giving me the opportunity to conduct a Master of Science study. I am more than glad for being able to work under the supervision of Prof. Dr. Ali Kalkanlı, and I would like to thank to him for all the guidance, supports and encouragement to the enrichment of this work.

This study would not be present without the continuous improvement seeking approach of my employer. Thanks to this constructive approach of Heraeus Electro-Nite Intl. NV providing enormous support both in material aid and in spiritual manner. I would like to thank to my dear colleagues; Koen Carlier, Frank Seutens, Wolfgang Baumgart, Danny Van Dooren, Joao Cunha, Francisco Costa Lopes, Monika Westphalen and Haluk Güldür for their kind supports.

All the field work creating the basis of this study was conducted at the foundry Ferromatrix NV. Therefore, I would like to thank to them, especially to Frederik Smet for his interest and collaboration.

My deepest thanks go to my entire family for their regardless, lifelong support, particularly to my parents Levent and Nevin Çehiz.

TABLE OF CONTENTS

ABSTRACT v

ÖZ vii

ACKNOWLEDGEMENTS x

TABLE OF CONTENTS xi

LIST OF TABLES xiii

LIST OF FIGURES xiv

CHAPTERS

1. INTRODUCTION 1

2. LITERATURE SURVEY 3

2.1. Cast Irons 3

2.2. Nodular Cast Irons 6

2.3. Production of Nodular Cast Iron 10

2.4. Solidification Mechanisms of Nodular Cast Iron 13

2.5. Cooling Curve Thermal Analysis of Nodular Cast Iron 21

2.6. Active Oxygen Amount in Nodular Cast Iron 33

3. EQUIPMENTS, SAMPLES AND METHODOLOGY 37

3.1. Nodular Cast Iron Production Process 37

3.2. Active Oxygen Amount Measurement in Nodular Cast Iron Melt 40

3.3. Cooling Curve Thermal Analysis of Nodular Cast Iron Melt 42

3.4. Metallographic Evaluation 51

3.5. Tensile Test 53

3.6. Optical Emission Spectroscopy 54

3.7. Data Correlation 54
4. RESULTS AND DISCUSSION 57
4.1. Chemical Analysis 57
4.2. Tensile Test 63
4.3. Cooling Curve Thermal Analysis 65
4.4. Metallographic Image Analysis 77
4.5. Regression Analysis 85
5. CONCLUSIONS 101
REFERENCES 105

LIST OF TABLES

TABLES

Table 2.1. Nodular cast iron grades and their main mechanical properties from tensile test according to DIN EN1563-3:2012. [10].....9
Table 2.2. Nomenclature and definition of the main points on a nodular cast iron cooling curve and its first and second derivatives. [27].....24
Table 3.1. Chemical composition of the cored wire with Mg master alloy. 39
Table 3.2. Chemical composition of the cored wire with inoculation master alloy...39
Table 3.3. Description and nomenclature of the cooling curve parameters identified by MeltControl2020™. [39] 45
Table 3.4. Chemical composition of the inoculants which were used as additives at the cup ingate. 46
Table 3.5. List of the cooling curve thermal analysis samples. 47
Table 4.1. Chemical analysis results obtained by OES and Celox Foundry™ conducted after the Mg treatment. 57
Table 4.2. Tensile test results of the specimens obtained from each ladle. 63
Table 4.3. The main results of cooling curve thermal analysis indicating contents of the analysis cups (Content types; 1-Spherix™ inoculant, 2-Sperix-Plus™ inoculant, 3-SMW605™ inoculant, 4-Te and S). 65
Table 4.4. The main results of metallographic image analysis indicating contents of the analysis cups (Content types; 1-Spherix™ inoculant, 2-Sperix-Plus™ inoculant, 3-SMW605™ inoculant, 4-Te and S). 77

LIST OF FIGURES

FIGURES

Figure 2.1. Classification of the graphite forms according to the DIN-EN-ISO 9445-1:2008. [5] 5
Figure 2.2. a) As-polished nodular cast iron microstructure via light microscope; b) Graphite nodule in etched nodular cast iron microstructure via scanning electron microscope. [8] 6
Figure 2.3. Number of graphite nodules per unit area in nodular cast iron samples with different section thickness and inoculation methods. [2] 7
Figure 2.4. Schematic representation of the treatment station for Mg cored wire treatment. [15] 12
Figure 2.5. Fe-C equilibrium phase diagram. [11] 14
Figure 2.6. Effect of silicon content on the stable and metastable eutectic transformation temperatures of Fe-C phase diagram. [2] 16
Figure 2.7. Effect of some alloying elements on the stable and metastable eutectic transformation temperatures of Fe-C phase diagram. [20] 17
Figure 2.8. Schematic representation of the grain structure of an ingot casting. [2] . 18
Figure 2.9. a) Schematic representation of the complex, multi-layer sulphide-oxide inclusion acting as nucleation site for graphite in nodular cast iron; b) A duplex sulfide-oxide inclusion in nodular cast iron captured via transmission electron microscope. [23] 19
Figure 2.10. Schematic representation of envelopment of graphite nodules by austenite phase during solidification of nodular cast iron. [22] 20
Figure 2.11. Illustration of the cooling curve of nodular cast iron melt with the first and second derivatives indicating the main points. [27] 23
Figure 2.12. Representative cooling curves for the solidification of hypoeutectic, eutectic and hypereutectic nodular cast iron melts. [29] 26

Figure 2.13. Representative cooling curves for a hypoeutectic cast iron solidifying in different graphite shapes (FG-lamellar graphite; CG-compacted graphite; SG-nodular graphite). TEU and TER represent the lower and upper eutectic temperatures of the CG curve. [2].....27
Figure 2.14. Representative cooling curves for the nodular cast iron melts with higher and lower nodularity. [31].....28
Figure 2.15. Correlation between a cooling curve parameter (ASE II) and resulting nodularity found by I. G. Chen and D. M. Stefanescu. [32].....29
Figure 2.16. a) Representative cooling curves for the nodular cast iron melts in different inoculation states; b) representative cooling curves revealing the difference between cooling curves of poorly inoculated (red) and well inoculated (green) nodular cast iron melts and the resulting micrographs. [16].....31
Figure 2.17. Schematic representation of the effect of cup sample thickness and state of inoculation on the shape of the cooling curve of eutectic nodular cast iron melt. [33] 32
Figure 2.18. The relation between active oxygen content of the nodular cast iron melt and the resulting nodularity found by F. Mampaey et al. via the investigation of 3 different nodular cast iron melts. [37].....35
Figure 3.1. Schematic representation of the process cycle applied for each ladle.....40
Figure 3.2. Schematic representation of Celox Foundry^{TM} equipment. [38].....41
Figure 3.3. Drawing of the QuiKCup Cover^{TM} cut by the vertical middle plan (units: mm). 1- Shell sand body; 2- Shell sand cover; 3- Tapes holding the inoculant at the ingate. [39].....43
Figure 3.4. Illustration for the mixing of the additives inserted to the ingate of QuiKCup Cover^{TM}. a) Right before the molten metal contacts to the cover; b) During the filling; c) Filled sample with homogeneously mixed additive. [39].....43
Figure 3.5. Drawing the QuiKCup Cover^{TM} sample and scheme showing how the sample was cut (units: mm). [39].....53
Figure 3.6. Schematic representation of a tensile test specimen (units: mm). [41] ...54
Figure 4.1. Active oxygen amount (aO) versus alloy grade. 62

Figure 4.2. Liquidus temperature (TL) versus alloy grade. 71
Figure 4.3. Upper eutectic temperature (TEmax) versus alloy grade for plain and inoculated analysis cups separately. 73
Figure 4.4. Time difference between the end of freezing and lower eutectic (TF_t – TEmin_t) versus alloy grade. 74
Figure 4.5. Liquidus temperature (TL) versus content of the analysis cup. 75
Figure 4.6. Lower eutectic temperature (TEmin) versus content of the analysis cup. 76
Figure 4.7. Graphite phase area percentage versus alloy grade 82
Figure 4.8. Graphite nodule count per unit area versus content of the analysis cup . 83
Figure 4.9. Graphite shape nodularity percentage versus content of the analysis cup 85
Figure 4.10. Ferrite phase area percentage versus graphite nodule count per unit area graph indicating the alloy grades and linear regression found for the grade EN-GJS-400-18. 86
Figure 4.11. Micrographs of some of the etched specimens at 100X magnification. a) Specimen from cup number 5. b) Specimen from cup number 8. c) Specimen from cup number 23. d) Specimen from cup number 24. e) Specimen from cup number 35. f) Specimen from cup number 36. 88
Figure 4.12. Lower eutectic temperature (TEmin) versus graphite nodule count per unit area graph for the grade EN-GJS-400-18 indicating content of the analysis cup and logistic function fit. 91
Figure 4.13. Lower eutectic temperature (TEmin) versus graphite nodule count per unit area graph for the grade EN-GJS-600-10C indicating content of the analysis cup and logistic function fit. 92
Figure 4.14. Lower eutectic temperature calculated by logistic function fit versus measured lower eutectic temperature graph for the grade EN-GJS-400-18. 93
Figure 4.15. Lower eutectic temperature calculated by logistic function fit versus measured lower eutectic temperature graph for the grade EN-GJS-600-10C. 94

Figure 4.16. Micrographs of some of the unetched specimens at 100X magnification. a) Specimen from cup number 29. b) Specimen from cup number 30. c) Specimen from cup number 31. d) Specimen from cup number 32. e) Specimen from cup number 93. f) Specimen from cup number 94. g) Specimen from cup number 95. h) Specimen from cup number 96.
Figure 4.17. Graphite shape nodularity percentage of the specimens from plain cups versus active oxygen amount (aO) measured in the ladle graph indicating the alloy grades. 98
Figure 4.18. Micrographs of some of the unetched specimens at 100X magnification. a) Specimen from cup number 45. b) Specimen from cup number 57. c) Specimen from cup number 24. d) Specimen from cup number 108. e) Specimen from cup number 120. f) Specimen from cup number 112. 100

CHAPTER 1

INTRODUCTION

As the demand for nodular cast iron increases, many foundries take actions to increase their production capacities in nodular cast iron product range.

When it is compared with lamellar graphite cast iron, nodular cast iron production is more complex due to the higher number of process parameters that needs to be controlled and the lower castability.

Especially, to produce ferritic or solution strengthened ferritic nodular cast iron grades, which are widely used in the applications where ductility is significant, as many process variables as possible needs to be controlled properly in order achieve the performance requirements.

To have chemical analysis by using optical emission spectroscopy (OES) and by combustion analysis (LECO) is quite common in foundries. Although chemical composition influences the resulting properties, it gives a very limited information on the solidification behavior which is controlled by various thermodynamic and kinetic considerations defining the resulting microstructure, thus the performance.

Cooling curve thermal analysis is a method letting us observe temperature versus time graphs of the samples from the melt while they are cooling and solidifying which can provide various information on solidification behavior of the melt on the melt-shop floor in just a few minutes. Therefore, it has a potential to evaluate the melt quality during the production, and to provide information that can be used to adjust the process parameters dynamically during the production.

Another useful method is the oxygen activity analysis providing information on the content of active oxygen, which is the oxygen found in elemental form (not chemically

bonded), in the nodular cast iron melt. Since the content of active oxygen has an important effect on the thermodynamic stability of nodular shape of the graphite particles found in nodular cast iron structure, it has a potential to provide information on the resulting structure.

It is known as a fundamental of Materials Engineering that the process defines the microstructure, and the microstructure defines the performance. Due to the high number of variables involved in each stage of the process, it is difficult to ensure the resulting microstructure, therefore the performance of nodular cast iron products.

The aim of this study is to find a scientific method, which is applicable to the industry, to estimate the resulting microstructural properties of nodular cast iron products by analyzing the treated nodular cast iron melt. In order to reach this aim, cooling curve thermal analysis and oxygen activity analysis were applied to the treated nodular cast iron melts of one ferritic nodular cast iron grade EN-GJS-400-18 and one solution strengthened ferritic nodular cast iron grade EN-GJS-600-10C. Metallographic evaluation and tensile tests were also conducted in order to observe the resulting microstructure and mechanical performance of the collected samples.

CHAPTER 2

LITERATURE SURVEY

2.1. Cast Irons

Although the earliest iron casting found belongs to the 6th century BC, industrial scale production of it started at the 18th century in England [1, 2].

At the present day, cast irons are the basic structural materials widely used in many industries such as automotive, machinery, piping and wind power industries, and they form 75% of the world production of cast raw products of all metals and alloys [2, 3].

Cast irons are the ferrous alloys containing Carbon (C) more than the solubility limit in austenite at the eutectic transformation temperature which is 2.14wt% and a considerable amount of Silicon (Si) [4]. Since the carbon content is higher than the solubility limit, it forms either graphite with the stable eutectic transformation or cementite (Fe_3C) with the metastable eutectic transformation [2]. Chemical composition has a significant effect on the microstructure, mechanical properties and corrosion behavior of cast irons. Therefore, alloying elements such as Copper (Cu), Manganese (Mn), Tin (Sn), Molybdenum (Mo) and Nickel (Ni) are used to obtain cast iron products with the desired properties.

With respect to the eutectic transformation type, cast irons can be divided into two main groups as Grey Cast Iron where stable eutectic transformation resulting carbon dissociation as graphite occurs and White Cast Iron where metastable transformation resulting cementite (Fe_3C) formation occurs. Their names were originated from the appearance of their fracture surface. Cementite in White Cast Iron results in brittle fracture with white and smooth fracture surface where Grey Cast Iron reveals some deformation prior to fracture, so it has a grey and rougher fracture surface. Therefore,

Grey Cast Iron is more favorable in structural applications where White Cast Iron may result in a catastrophic failure.

Grey Cast Iron is divided into further subgroups. Depending on the shape of graphite formed during the crystallization, there are three main groups of Grey Cast Iron; 1) Lamellar Graphite Cast Iron (abbreviated as GJL in EN Standards), 2) Compacted Graphite Cast Iron (abbreviated as GJV in EN Standards), 3) Nodular Graphite Cast Iron (abbreviated as GJS in EN Standards) also known as ductile iron [3]. According to EN-ISO-9445, there are 6 forms of graphite shape which are revealed in Figure 2.1 [5]. Form I represents the main graphite shape for Lamellar Graphite Cast Iron. Form III represents the main graphite shape for Compacted Graphite Cast Iron. Form VI represents the main graphite shape for Nodular Graphite Cast Iron, and the other forms are the intermediate graphite shapes.

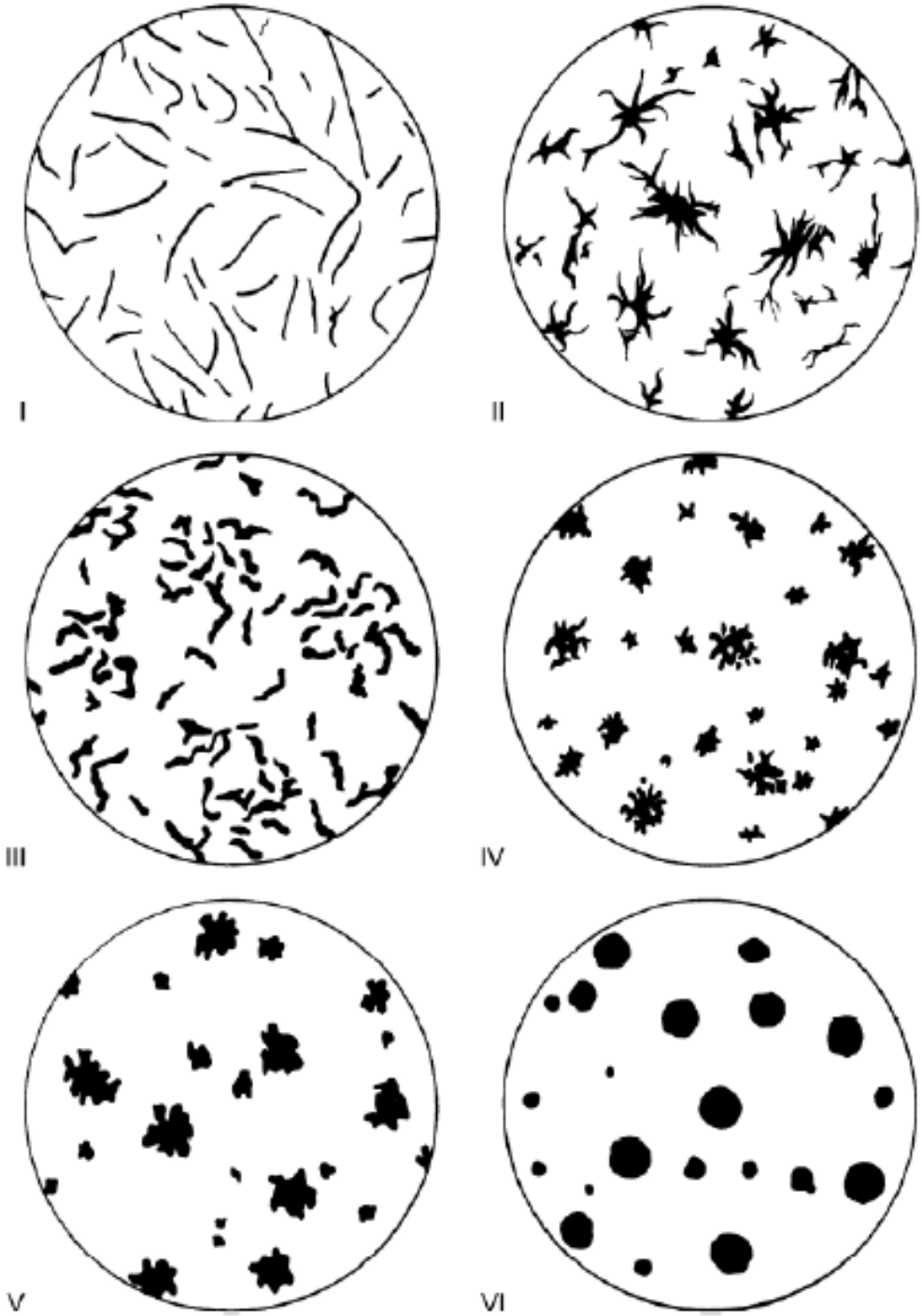

Figure 2.1. Classification of the graphite forms according to the DIN-EN-ISO 9445-1:2008. [5]

2.2. Nodular Cast Irons

Although industrial production of nodular cast iron has started only 70 years ago, it represents approximately 25% of the world production of cast raw products of all metals and alloys [6, 7].

As one can expect from its name, the main characteristic of nodular cast iron is nodule-shaped graphite particles observed among the matrix (see Figure 2.2) [8].

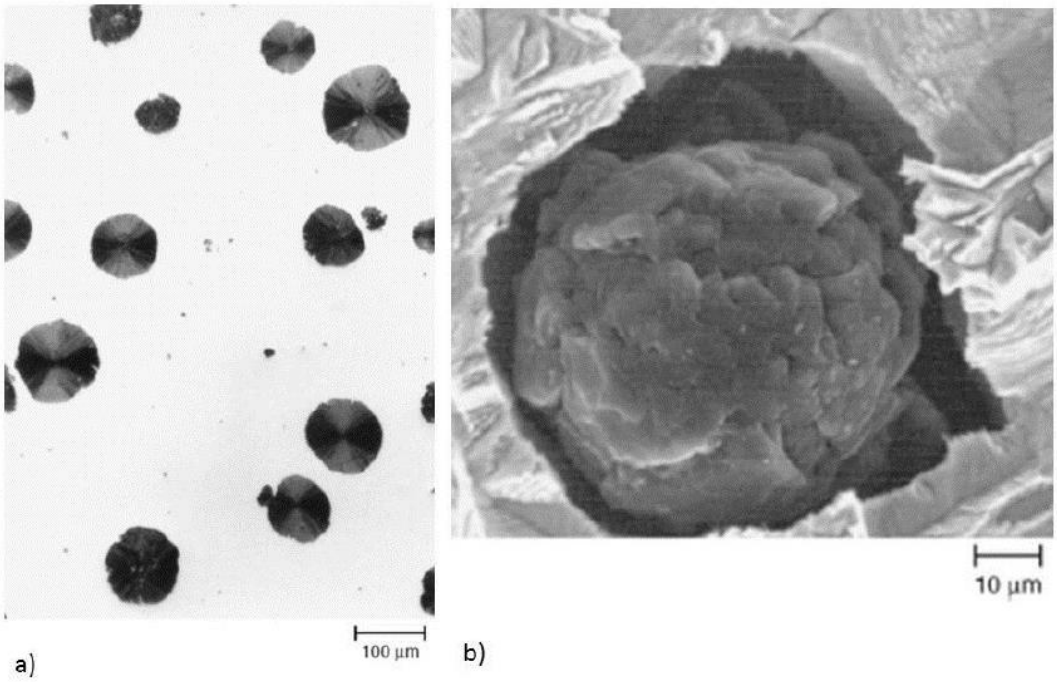

Figure 2.2. a) As-polished nodular cast iron microstructure via light microscope; b) Graphite nodule in etched nodular cast iron microstructure via scanning electron microscope. [8]

Size and number of the graphite nodules are determined mainly by cooling rate and amount of heterogeneous nucleation sites [2, 9]. The effect of section thickness, which defines the cooling rate, and the inoculation method, which affects the amount of heterogeneous nucleation sites, on the nodule count is represented in Figure 2.3.

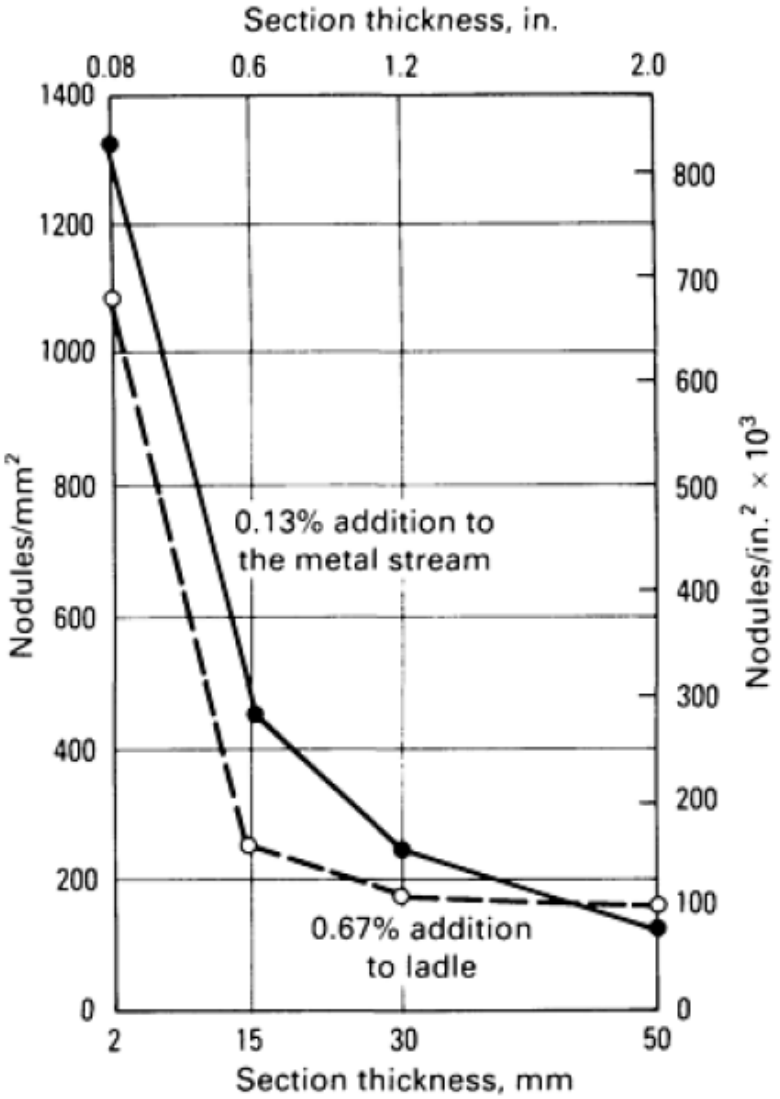

Figure 2.3. Number of graphite nodules per unit area in nodular cast iron samples with different section thickness and inoculation methods. [2]

Mechanical properties of the nodular cast iron depend on shape, size and number of graphite nodules, but also content of the matrix [2, 10]. The matrix can be fully ferritic, fully pearlitic or somewhere in between. The matrix structure is determined mainly by alloying elements, cooling rate and graphite particle density [2, 8]. Since for some applications strength is the main concern where it is elongation for some others, there are different nodular cast iron grades providing different mechanical properties. A list of those grades according to EN ISO 1563 is revealed in Table 2.1.

Table 2.1. *Nodular cast iron grades and their main mechanical properties from tensile test according to DIN EN1563-3:2012. [10]*

Material Designation	**Decisive Wall Thickness (mm)**	**Min. Yield Strength (MPa)**	**Min. Tensile Strength (MPa)**	**Min. Elongation (%)**
EN-GJS-350-22-LT	$t \leq 30$	220	350	22
	$30 < t \leq 60$	210	330	18
	$60 < t \leq 200$	200	320	15
EN-GJS-350-22-RT	$t \leq 30$	220	350	22
	$30 < t \leq 60$	220	330	18
	$60 < t \leq 200$	210	320	15
EN-GJS-350-22	$t \leq 30$	220	350	22
	$30 < t \leq 60$	220	330	18
	$60 < t \leq 200$	210	320	15
EN-GJS-400-18-LT	$t \leq 30$	240	400	18
	$30 < t \leq 60$	230	380	15
	$60 < t \leq 200$	220	360	12
EN-GJS-400-18-RT	$t \leq 30$	250	400	18
	$30 < t \leq 60$	250	390	15
	$60 < t \leq 200$	240	370	12
EN-GJS-400-18	$t \leq 30$	250	400	18
	$30 < t \leq 60$	250	390	15
	$60 < t \leq 200$	240	370	12
EN-GJS-400-15	$t \leq 30$	250	400	15
	$30 < t \leq 60$	250	390	14
	$60 < t \leq 200$	240	370	11
EN-GJS-450-10	$t \leq 30$	310	450	10
	$30 < t \leq 60$	to be agreed between manufacturer and buyer		
	$60 < t \leq 200$			
EN-GJS-500-7	$t \leq 30$	320	500	7
	$30 < t \leq 60$	300	450	7
	$60 < t \leq 200$	290	420	5
EN-GJS-600-3	$t \leq 30$	370	600	3
	$30 < t \leq 60$	360	600	2
	$60 < t \leq 200$	340	550	1
	$t \leq 30$	420	700	2

EN-GJS-700-2	30 < t ≤ 60	400	700	2
	60 < t ≤ 200	380	650	1
EN-GJS-800-2	t ≤ 30	480	800	2
	30 < t ≤ 60	to be agreed between manufacturer and buyer		
	60 < t ≤ 200			
EN-GJS-900-2	t ≤ 30	600	900	2
	30 < t ≤ 60	to be agreed between manufacturer and buyer		
	60 < t ≤ 200			

Although nodular cast iron grades provide a wide range of mechanical properties, their thermal conductivity varies between 33.5 W/m•K and 36.5 W/m•K (at 100°C) which is not sufficient for some applications like engine blocks, cylinder heads and brake discs [2].

2.3. Production of Nodular Cast Iron

Nodular cast iron production process has 3 main metallurgical steps which are melting, treating and pouring. For each of these steps, there are different methods being used in the industry, and each step has a significant effect on the resulting properties.

The first step is melting of the raw materials. Melting can be performed by electrical induction furnaces, electrical arc furnaces or cupola furnaces. Since it provides certain advantages like ease of operation, flexibility of production, cleaner melt and lower environmental impact, electrical induction furnace is the most commonly used one. The charge materials to produce base iron with electrical induction furnaces are typically pig iron, nodular cast iron returns of the plant to recycle and steel scrap to lower the carbon content. A special quality pig iron with the requirements; S<0.03%, P<0.08% and Mn<0.5% needs to be used for nodular cast iron production [11]. In the case of cupola melting furnace, resulting sulphur content is above the limit due to nature of the process, and a desulphurization process needs to be conducted typically by using calcium carbide (CaC_2) or Mg addition to the ladle [2]. Desulphurization

process needs to be controlled well since at least 0.008% of sulphur content is needed to create heterogeneous nucleation sites for the graphite particles by inoculation [12]. After melting the raw materials, the alloying additions may be needed to achieve the aimed chemical composition for the desired alloy grade.

The second step is treating the melt by a high oxygen affinity element, typically Mg. The aim is to nodularize the graphite shape by decreasing the content of surface-active elements which are O and S. Tundish cover, wire treatment, sandwich and Georg Fischer converter are the common methods for Mg treatment. Mg has a boiling point of 1090°C where the base iron to be treated is generally at above 1400°C, and this leads to a very aggressive reaction [2]. Therefore, pure Mg usage is not common unless Georg Fischer converter is the method. Georg Fischer converter has a design ensuring a safe treatment process even with pure metallic Mg, and it is mostly used in the plants with cupola furnace for a simultaneous desulfurization and Mg treatment [2]. For the other methods, Mg ferroalloys with varying Mg contents are commonly used. The main idea of the methods tundish cover and sandwich is to place the Mg ferroalloy in a pocket at the bottom of ladle before tapping the base iron from the furnace to the ladle. Wire treatment method is also getting more and more popular due to its highly automatized nature which fits to Industry 4.0 concept. Its main idea is feeding Mg ferroalloy containing cored wire into the melt by using a wire feeder machine (see Figure 2.4). Another advantage of wire treatment is the ability of calculation of the treatment alloy addition ratio accurately. Since the treatment alloy is fed after the melt is tapped into the ladle, it is possible to measure the exact weight of the melt and to calculate the addition amount accordingly which is not the case for the other treatment methods. In terms of Mg yield, wire treatment has a disadvantage such that it has a Mg yield in range of 40% to 60% which is 60% to 80% for tundish cover and sandwich methods [13, 14].

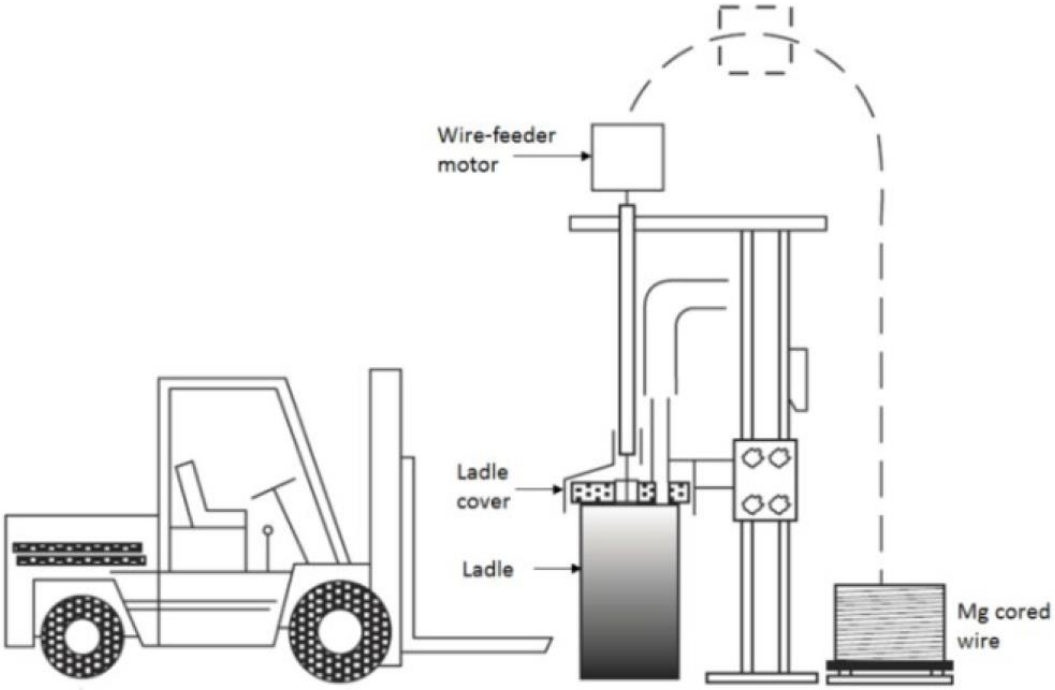

Figure 2.4. Schematic representation of the treatment station for Mg cored wire treatment. [15]

The last step is pouring the treated melt into the molds. To provide heterogeneous nucleation sites favoring the graphite nucleation, inoculant alloy particles needs to be added into the ladle, into the mold or into the stream in between. There are various types of inoculant with different chemical compositions and particle sizes depending on the application place. For example, the inoculants containing Ba as active element have relatively low inoculation effect, but they have a high fading resistance which makes them good for ladle application where the ones containing Sr have very strong inoculation effect with very limited fading resistance which makes them good for stream application [16].

2.4. Solidification Mechanisms of Nodular Cast Iron

It is significant to understand the solidification mechanisms to have a good control on the resulting microstructure, therefore the properties. As can be seen on the Fe-C equilibrium phase diagram (see Figure 2.5), the maximum carbon content that can be solved in austenite phase is 2.11wt%. Since cast irons have a carbon content higher than this limit, they undergo a eutectic transformation ending up with austenite and graphite (or cementite) phases. The eutectic composition includes 4.3wt% of carbon. Therefore, the alloys with carbon content lower than 4.3wt% are called hypoeutectic where the ones with higher than 4.3wt% are called hypereutectic. There are two possible equilibrium temperatures for the eutectic transformation of cast iron. In the case of stable (grey) eutectic transformation, austenite and graphite phases are formed, and equilibrium eutectic transformation temperature is 1152°C where it is 1145°C for metastable (white) eutectic transformation resulting in austenite and cementite formation [11].

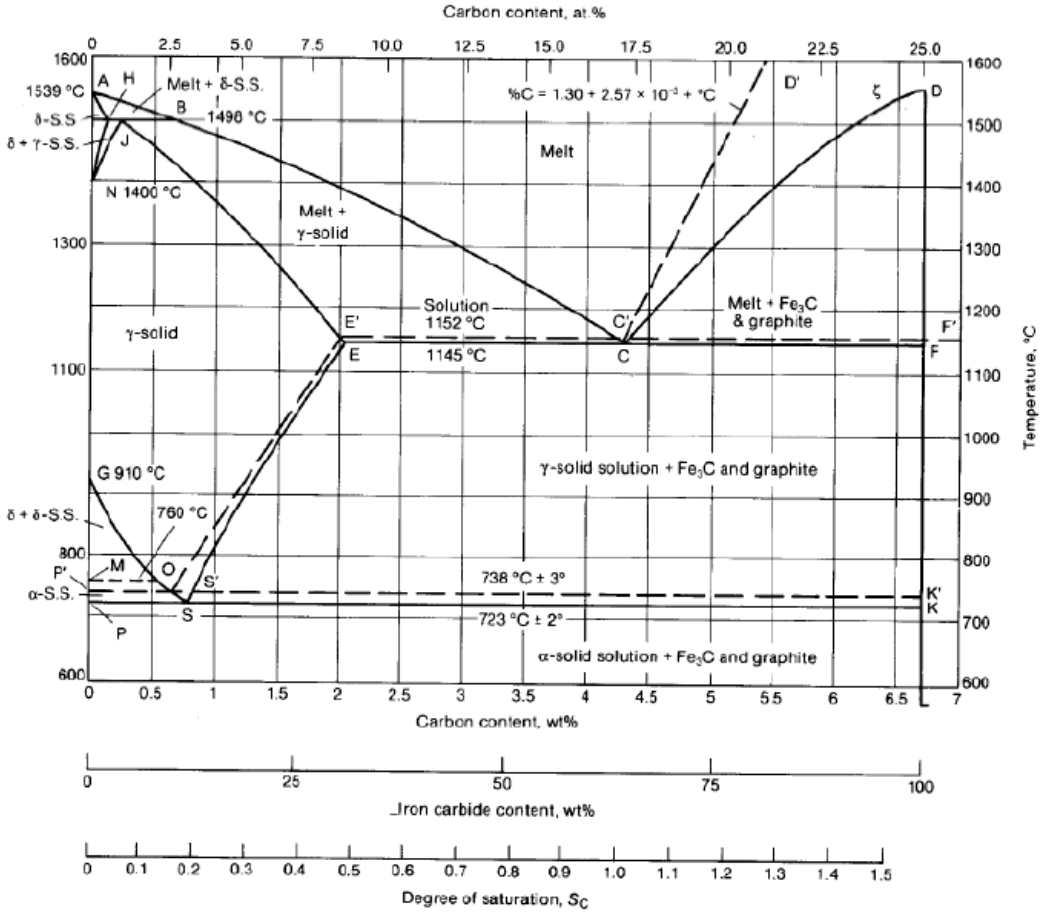

Figure 2.5. Fe-C equilibrium phase diagram. [11]

For the melts with hypoeutectic composition, once the liquidus temperature is reached, solidification starts with nucleation and growth of primary (pro-eutectic) austenite dendrites. As temperature decreases from the liquidus temperature through the eutectic transformation temperature, content of the primary austenite phase increases. Since carbon content of the austenite phase is lower than the melt, carbon content of the liquid phase increases as austenite dendrites grow. When the eutectic transformation temperature is reached, carbon content of the liquid phase reaches to the eutectic composition, and it solidifies as austenite and graphite (or cementite) by eutectic transformation [17]. If the melt has eutectic composition, once the eutectic

transformation temperature is reached, entire melt solidifies by eutectic transformation. For the ones with hypereutectic composition, solidification starts at liquidus temperature as in hypoeutectic but this time with nucleation and growth of primary graphite instead of austenite. As a result of further temperature decrease, primary graphite content increases, and carbon content of the liquid phase decreases. At eutectic transformation temperature, carbon content of the liquid phase becomes equal to the eutectic composition, and it solidifies by eutectic transformation.

Fe-C equilibrium phase diagram applies for iron carbon binary systems, but cast iron includes many elements other than iron and carbon. Most of these elements are commonly in small portions, but the content of silicon is significantly high since it favors the stable (grey) solidification. This situation requires the use of a ternary Fe-C-Si phase diagram. It was discovered that increasing silicon content reduces the carbon content at eutectic point and carbon solubility in austenite phase. Therefore, with a correction factor applied to the carbon content, Fe-C binary phase diagram can be used for cast iron alloys. This corrected carbon content replacing the carbon content on the X-axis of the diagram is called as Carbon Equivalent (C.E.), and it is calculated by Equation 2.1 [19]. In addition, the empirical formula (Equation 2.2) based on the effect of carbon, silicon and phosphor contents on Fe-C binary phase diagram was created by Heraeus Electro-Nite Intl. NV by using the liquidus temperatures obtained by cooling curve thermal analysis and the chemical analysis results obtained by combustion (LECO) analysis [18].

Equation 2.1. C.E. [%] = C [%] + (Si [%] + P [%]) / 3

Equation 2.2. C.E.L. [%] = C [%] + (Si [%]) / 4 + (P [%]) / 2

Silicon and some other elements have an effect on stable (grey) and metastable (white) eutectic transformation temperatures (see Figure 2.6 and 2.7). For a cast iron melt to have a metastable eutectic transformation, it needs to have an undercooling equal to the difference between stable and metastable eutectic transformation temperatures. Therefore, the elements increasing this difference by increasing the stable eutectic temperature and decreasing the metastable one favor the stable (grey) solidification, and they are called graphitizing elements. Silicon, nickel, cobalt and copper are the common examples for graphitizing elements. On the other hand, the elements decreasing the difference between stable and metastable eutectic temperatures by reducing the stable eutectic temperature and increasing the metastable one favor the metastable (white) solidification, and they are called carbide formers. Chromium, titanium and vanadium are the common examples for carbide formers. Although they give us some idea about the solidification sequence, it is important to remind that equilibrium phase diagrams are based on thermodynamic calculations, and they apply at equilibrium conditions which cannot be met in industrial scale.

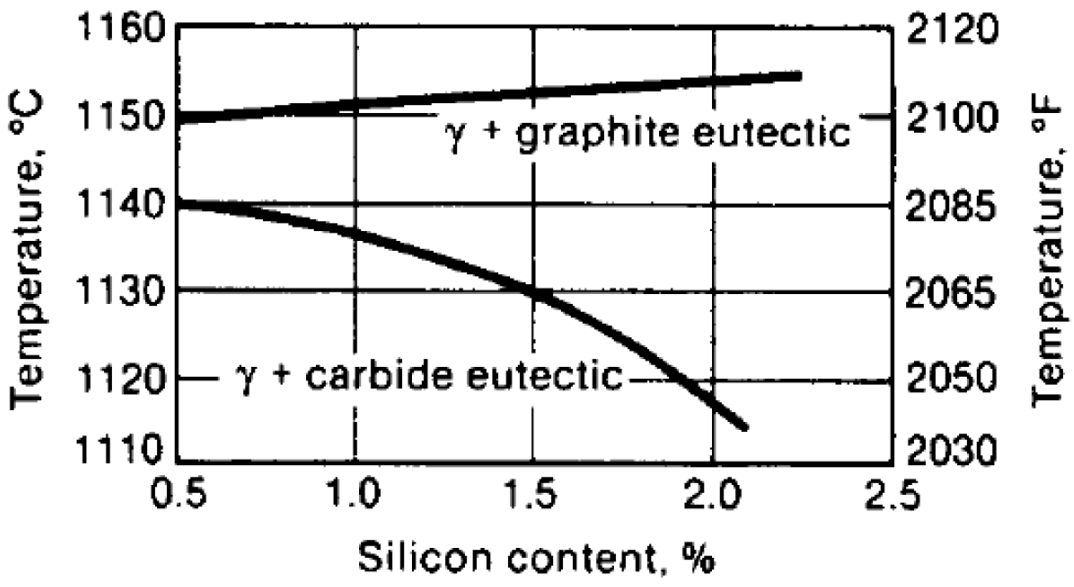

Figure 2.6. Effect of silicon content on the stable and metastable eutectic transformation temperatures of Fe-C phase diagram. [2]

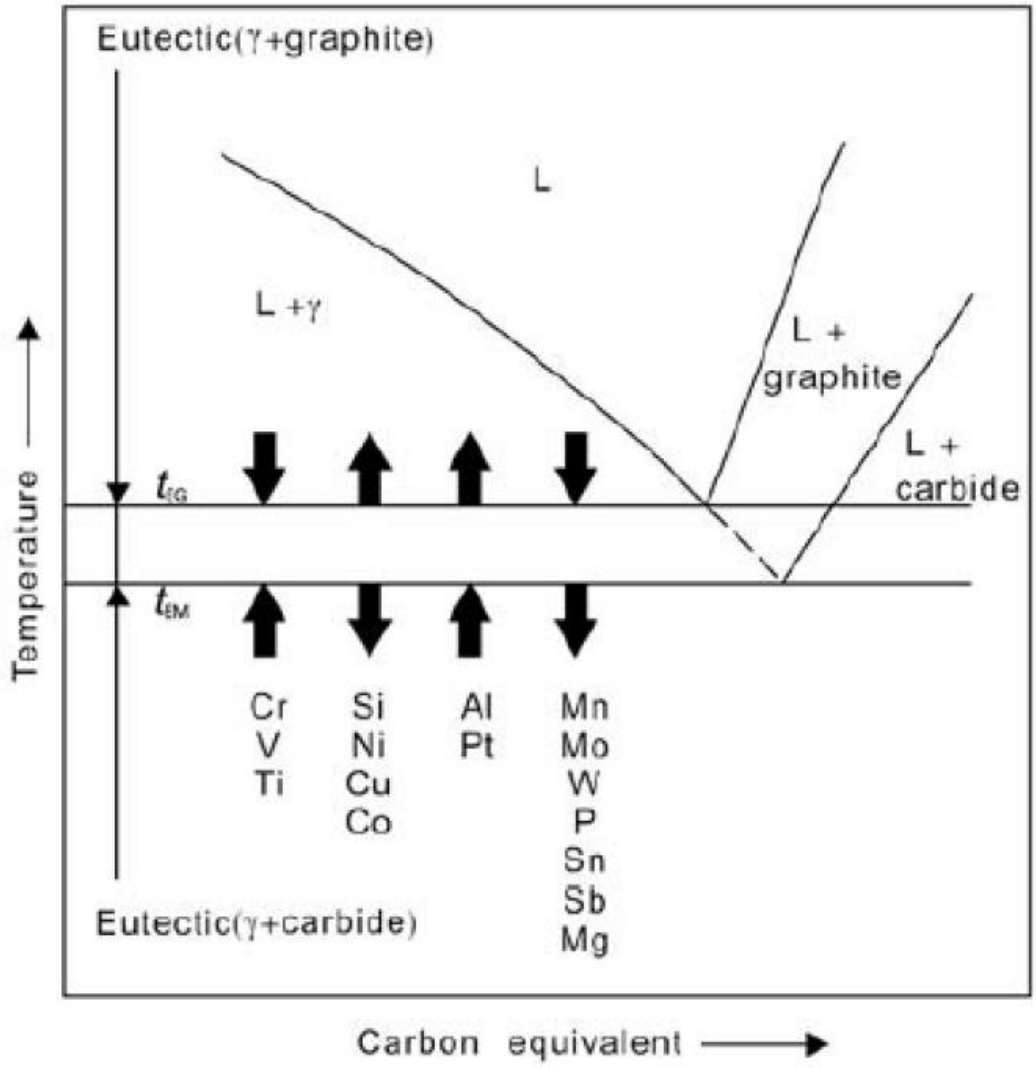

Figure 2.7. Effect of some alloying elements on the stable and metastable eutectic transformation temperatures of Fe-C phase diagram. [20]

Nucleation of primary (pro-eutectic) austenite occurs heterogeneously on the interface of some solid particles like oxides and carbides with liquid phase [21]. Then, it is followed by the growth with a non-planar solidification interface such as columnar or equiaxed dendritic depending on the required nucleation undercooling and the magnitude of constitutional undercooling [2, 22]. For a typical ingot casting (see Figure 2.8), the nucleus formed on the mould wall heterogeneously are likely to have columnar growth towards the center of mould which is the opposite direction of heat flow, then their growth might be terminated by the equiaxed grains if the undercooling needed for the nucleation of equiaxed grains is less than the constitutional undercooling ahead of the growing columnar grains [2, 22].

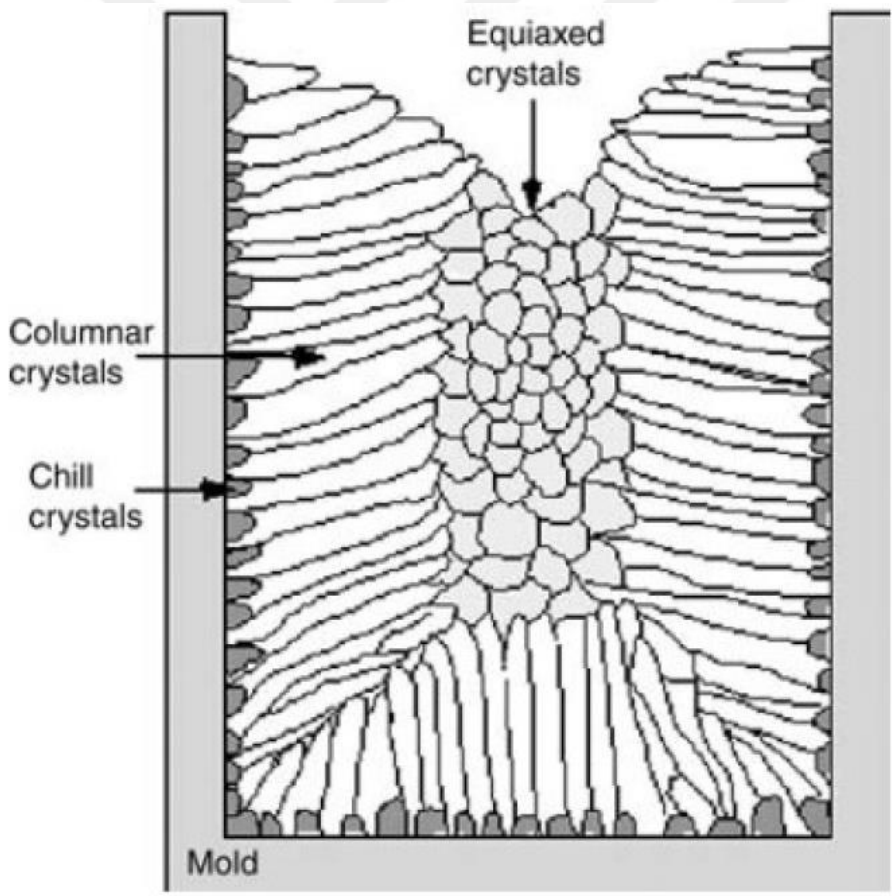

Figure 2.8. Schematic representation of the grain structure of an ingot casting. [2]

The graphite phase also nucleates heterogeneously on the interface of some solid particles with liquid phase, since it is more feasible in terms of energy [2]. The most well accepted theory for graphite nuclei which was introduced by T. Skaland et al. claims that a complex, multi-layer sulphide-oxide inclusion with a diameter of approximately 1 µm acts as nucleation site for the graphite particles [23]. These inclusions have sulphides like MgS in their core which are covered by Mg silicates like $MgO.SiO_2$ in the first layer and some hexagonal silicate molecules of some elements like Al, Ca, Sr and Ba on the surface providing low interface energy for the nucleation of graphite phase (see Figure 2.9) [23]. Therefore, these elements forming hexagonal silicates are considered as active elements of inoculant alloys. Since the melt is treated by Mg, O and S content is quite low, and the interface energy between graphite and liquid iron is high which leads graphite to grow with minimum surface area to volume ratio resulting in a spherical shape [24].

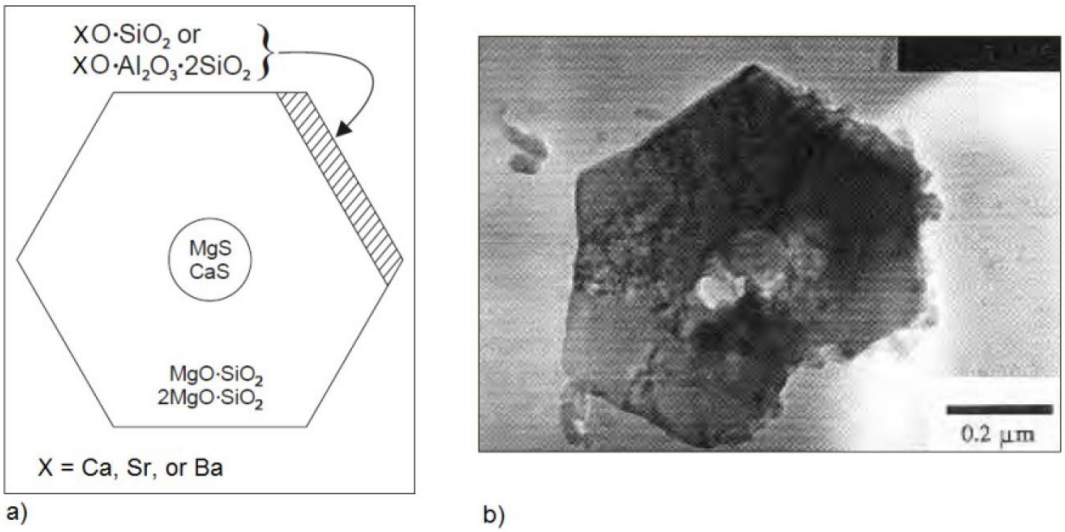

Figure 2.9. a) Schematic representation of the complex, multi-layer sulphide-oxide inclusion acting as nucleation site for graphite in nodular cast iron; b) A duplex sulfide-oxide inclusion in nodular cast iron captured via transmission electron microscope. [23]

Eutectic phase mixture of grey cast iron alloys consists of austenite and graphite. Eutectic transformation of nodular cast iron occurs by nucleation followed by divorced eutectic growth which leads two solid phases to grow separately in liquid phase without any direct solute exchange between two solid phases [2, 25]. Nucleation and growth mechanisms of eutectic austenite and graphite phases are same as the pro-eutectic ones until a certain point. When the diameter of graphite nodule exceeds a certain value (roughly 10 to 15 µm), it gets surrounded by austenite dendrite arms terminating its contact with liquid phase, and that limits further growth of graphite nodule by the limited rate of solid state diffusion (see Figure 2.10) [22, 26]. Since during the austenite envelopment, the parts of the graphite nodule which have not been enveloped will be in contact with liquid and will grow much faster than the enveloped parts, the speed that graphite nodule gets enveloped has a significant effect on the graphite shape [26]. Higher cooling rate and better inoculation practice favor the faster austenite envelopment and better nodule shape of graphite where the presence of some elements like Bi, Sb and Pb favors the slower envelopment and worse nodule shape [26].

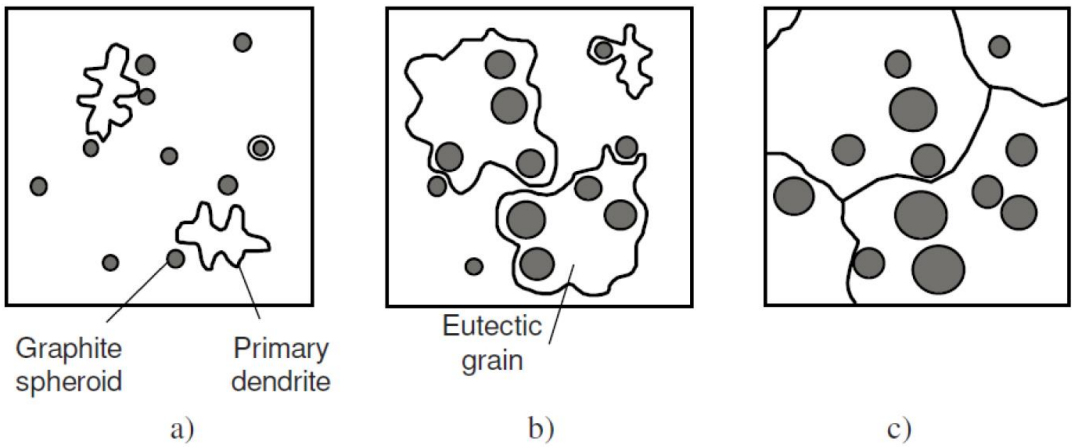

Figure 2.10. Schematic representation of envelopment of graphite nodules by austenite phase during solidification of nodular cast iron. [22]

2.5. Cooling Curve Thermal Analysis of Nodular Cast Iron

Although thermal analysis is a general term including all the analysis methods measuring a change in a specific property of a substance as a result of a change in temperature, in foundry industry cooling curve thermal analysis method is the most practical one. Cooling curve thermal analysis is conducted by sampling certain amount of liquid metal into a thermocouple inserted mould which lets us observe the cooling curve of the sample during cooling, solidification and solid-state transformations by means of temperature versus time graph. The obtained cooling curve is a result of heat balance between the sample and its surroundings. When there is no phase transformation, cooling curve represents the cooling of a liquid or solid substance, and it has a constant negative slope indicating the cooling rate which depends on heat transport conditions, mass and heat capacity of the substance. In the case of a phase transformation, cooling curve is affected by the thermal consequences of the transformation, and the change in slope depends on enthalpy of transformation and the fraction of the transformed substance. If the transformation is a solidification, the enthalpy change will be negative, so certain amount of heat will be evolved, and slope of the cooling curve will move from its negative value in positive direction with a magnitude determined by the latent heat of solidification and fraction of the transformed substance.

Cooling curve of cast iron reveals various peculiarities letting us name the critical points on cooling curve which may indicate some information on the sample properties. It was observed in literature that nomenclature of these points varies highly. The company OCC GmbH has one of the most informative description of nomenclature of the points on the cooling curve and its first and second derivatives with respect to time. Therefore, it can be a good example to understand the structure of the cooling curve of cast iron. The critical points on the cooling curve were revealed in Figure 2.11, and descriptions of the nomenclature were listed in Table 2.2 [27]. The first derivative and second derivative curves are used to determine the critical points so that zero points on the first derivative curve represent the arrests on the cooling

curve, and zero points on the second derivative curve represent the inflection points on the cooling curve [27].

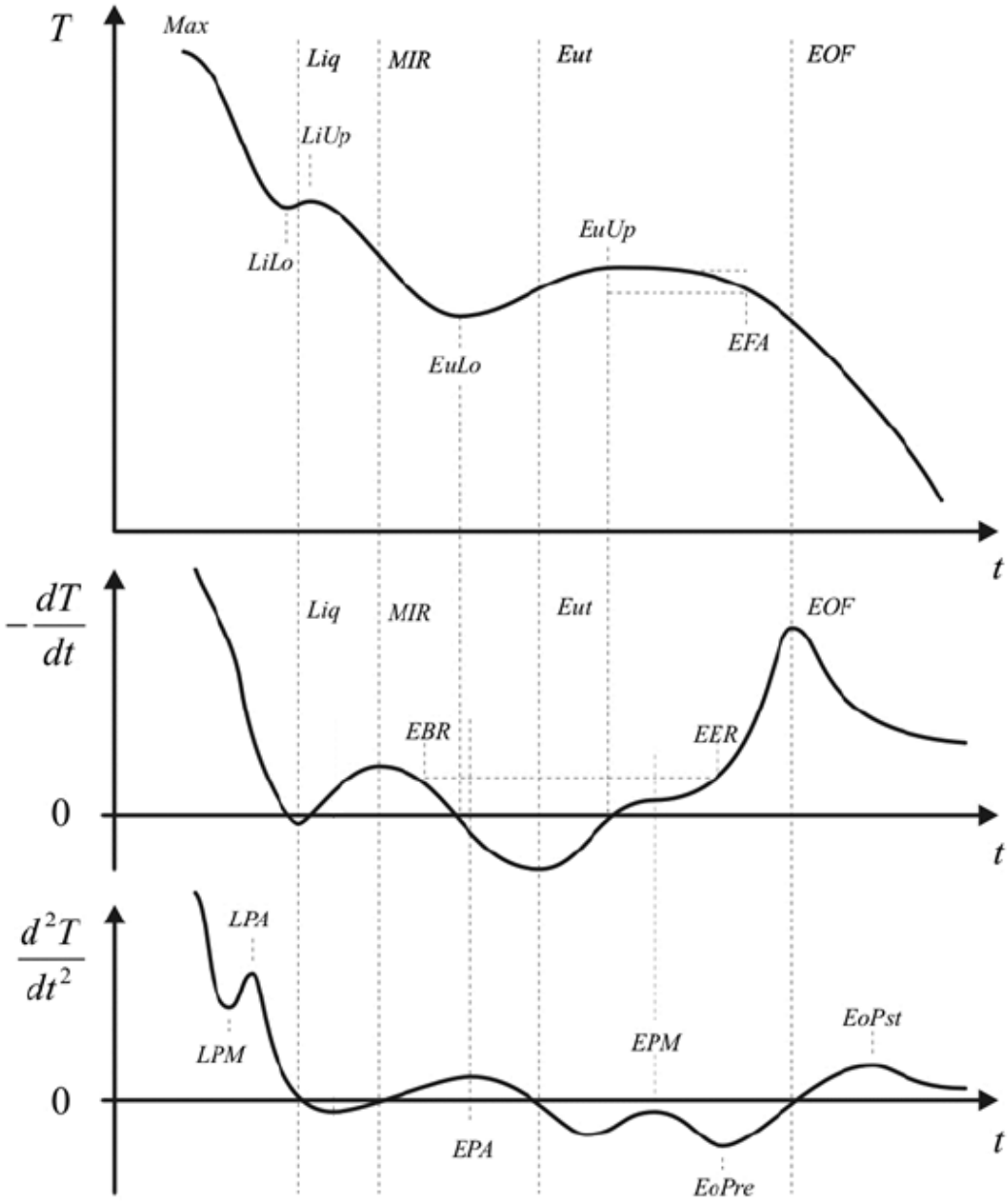

Figure 2.11. Illustration of the cooling curve of nodular cast iron melt with the first and second derivatives indicating the main points. [27]

Table 2.2. *Nomenclature and definition of the main points on a nodular cast iron cooling curve and its first and second derivatives. [27]*

Designation	Unit	Signification
Max	°C	Maximum temperature measured
LPM	°C/s²	Maximum at second derivative before liquidus
LPA	°C/s²	Highest temperature acceleration before liquidus
LiLo	°C	Minimum temperature measured before liquidus
Liq	°C	Liquidus temperature
LiUp	°C	Maximum temperature measured after liquidus
MIR	°C	Temperature with highest cooling rate before eutectic
EPA	°C/s²	Highest temperature acceleration before eutectic
EuLo	°C	Minimum temperature measured before eutectic
Eut	°C	Eutectic temperature
EuUp	°C	Maximum temperature measured after eutectic
EPM	°C/s²	Smallest temperature acceleration after eutectic
EBR	°C	Temperature at beginning of eutectic transformation
EER	°C	Temperature at end of eutectic transformation
EFA	°C	Temperature at fade of eutectic transformation
EoPre	°C/s²	Maximum temperature acceleration before EoF
EoF	°C	Temperature at end of solidification
EoPst	°C/s²	Minimum temperature acceleration after EoF

The early studies on cooling curve thermal analysis of cast iron revealed that composition of cast iron has an effect on its cooling curve. For instance, it was observed by Loper et al. that temperature of the first arrest on the cooling curve decreases by increasing carbon equivalent until a certain point, and beyond this point it starts increasing back, so that the first arrest represents the liquidus and the second arrest represents the eutectic transformation [28]. Based on this knowledge, it was proven by further studies that carbon equivalent value of hypo-eutectic alloys can be calculated by using the liquidus temperature obtained from the cooling curve, and carbon content can be calculated for those alloys by using liquidus and metastable eutectic transformation temperatures obtained from the cooling curve of white solidification [18].

With the state-of-art technology, it is convenient to recognize the difference between cooling curve characteristics of composition dependent solidification types. In Figure 2.12, the representative cooling curves and the correspondence with the phase diagram for 3 different compositions are given [29]. The cooling curve on the left belongs to hypoeutectic composition. The one on the right has hypereutectic composition, and the one at the bottom is with eutectic or near-eutectic composition. On the cooling curve of hypoeutectic nodular cast iron, the first arrest occurs at liquidus by the nucleation and growth of austenite dendrites [27]. The second arrest represents the eutectic transformation by the nucleation and growth of austenite-graphite eutectic phase mixture [27]. Since nucleation of graphite requires excess energy, undercooling is observed, and eutectic transformation occurs at a temperature lower than the equilibrium transformation temperature which is seen on phase diagram [27]. Once graphite growth starts, an increase in temperature is observed due to the released energy as a result of carbon dissociation [27]. This phenomenon is named as recalescence. Hypereutectic nodular cast iron also has a liquidus arrest, but unlike hypoeutectic, it reveals undercooling and recalescence at liquidus because here graphite nucleation and growth starts at liquidus instead of eutectic [27]. At eutectic transformation, it doesn’t reveal undercooling and recalescence because almost all graphite nucleation occurs between liquidus and eutectic [27]. Cooling curve of eutectic or near-eutectic nodular cast iron does not reveal a liquidus arrest because the solidification occurs only by the eutectic transformation [27].

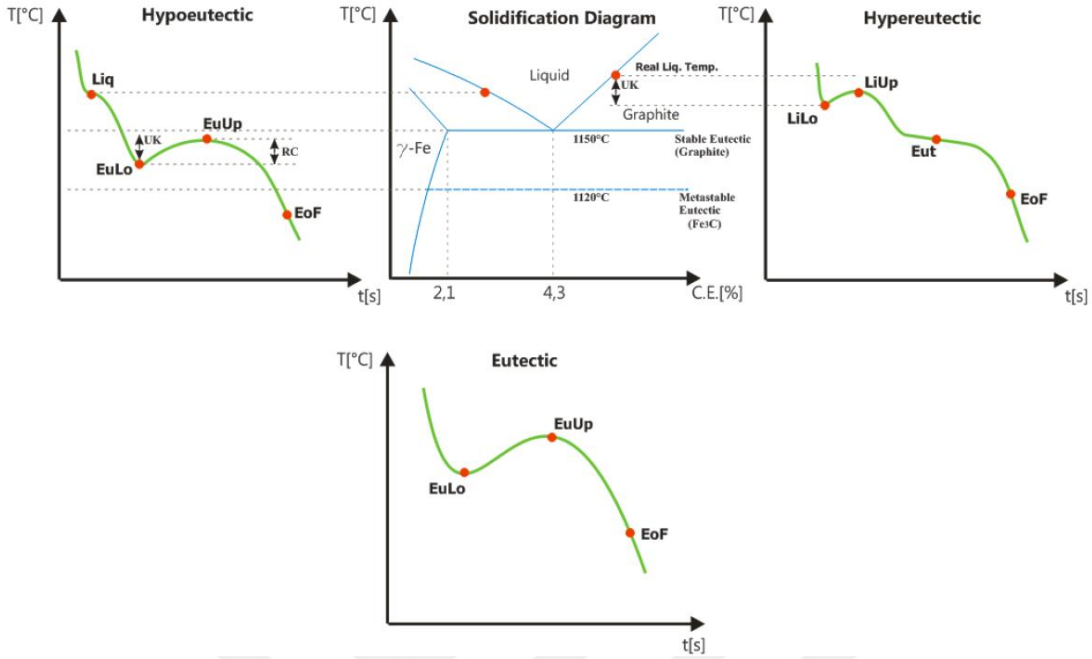

Figure 2.12. Representative cooling curves for the solidification of hypoeutectic, eutectic and hypereutectic nodular cast iron melts. [29]

Other than the composition dependent solidification types, grey cast iron categories with different graphite shapes also has different characteristics by means of their cooling curves (see Figure 2.13). For instance, compacted graphite cast iron reveals greater undercooling and recalescence than that lamellar and nodular graphite cast irons do [30].

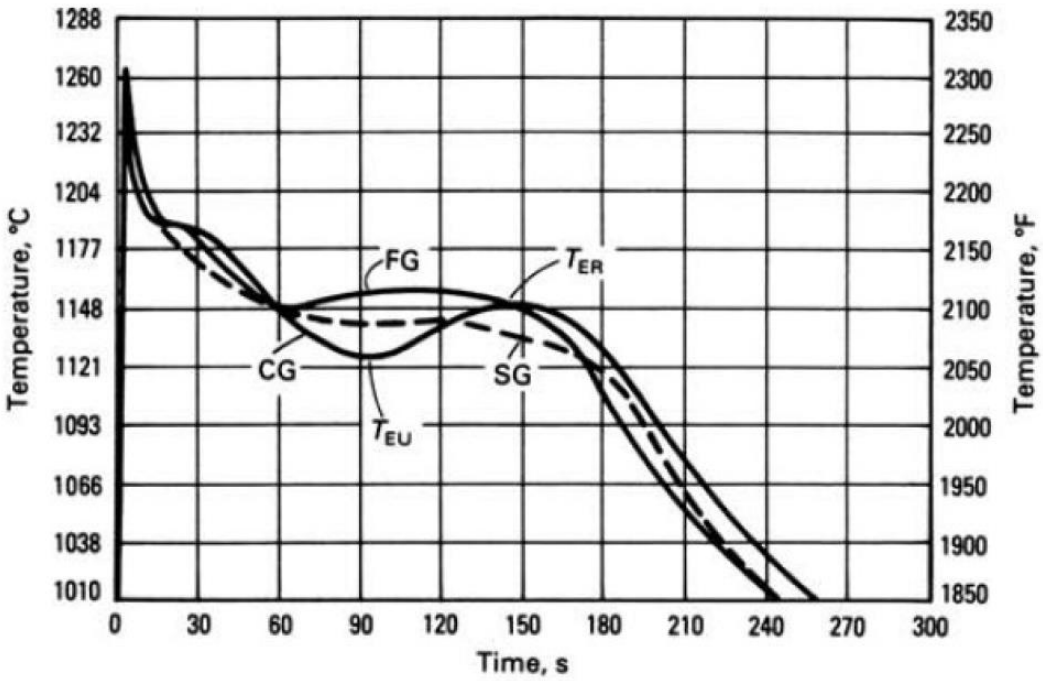

Figure 2.13. Representative cooling curves for a hypoeutectic cast iron solidifying in different graphite shapes (FG-lamellar graphite; CG-compacted graphite; SG-nodular graphite). TEU and TER represent the lower and upper eutectic temperatures of the CG curve. [2]

If we investigate the nodular cast iron category, it was presented by the company OCC GmbH that the microstructures with higher nodularity reveal a lower recalescence value in eutectic part of their cooling curves (see Figure 2.14) [31].

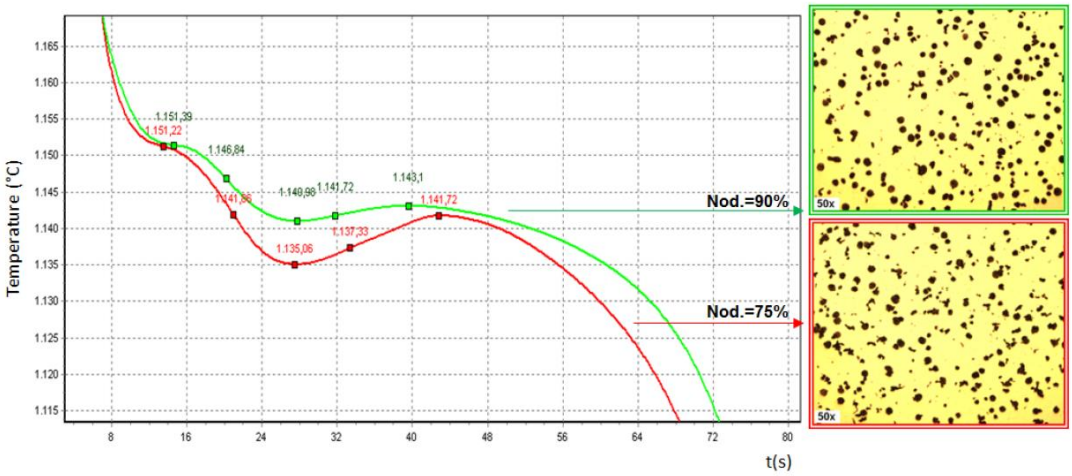

Figure 2.14. Representative cooling curves for the nodular cast iron melts with higher and lower nodularity. [31]

A diverse study, giving some clues about the relation of thermal analysis variables with the resulting nodularity of graphite particles in the microstructure of nodular cast iron, was conducted by I. G. Chen and D. M. Stefanescu [32]. ASE II is the average slope of the second stage of eutectic transformation [32]. The found correlation is shown in Figure 2.15. Although it is obvious that there is a correlation, neither equation of the correlation curve nor the correlation coefficient was published.

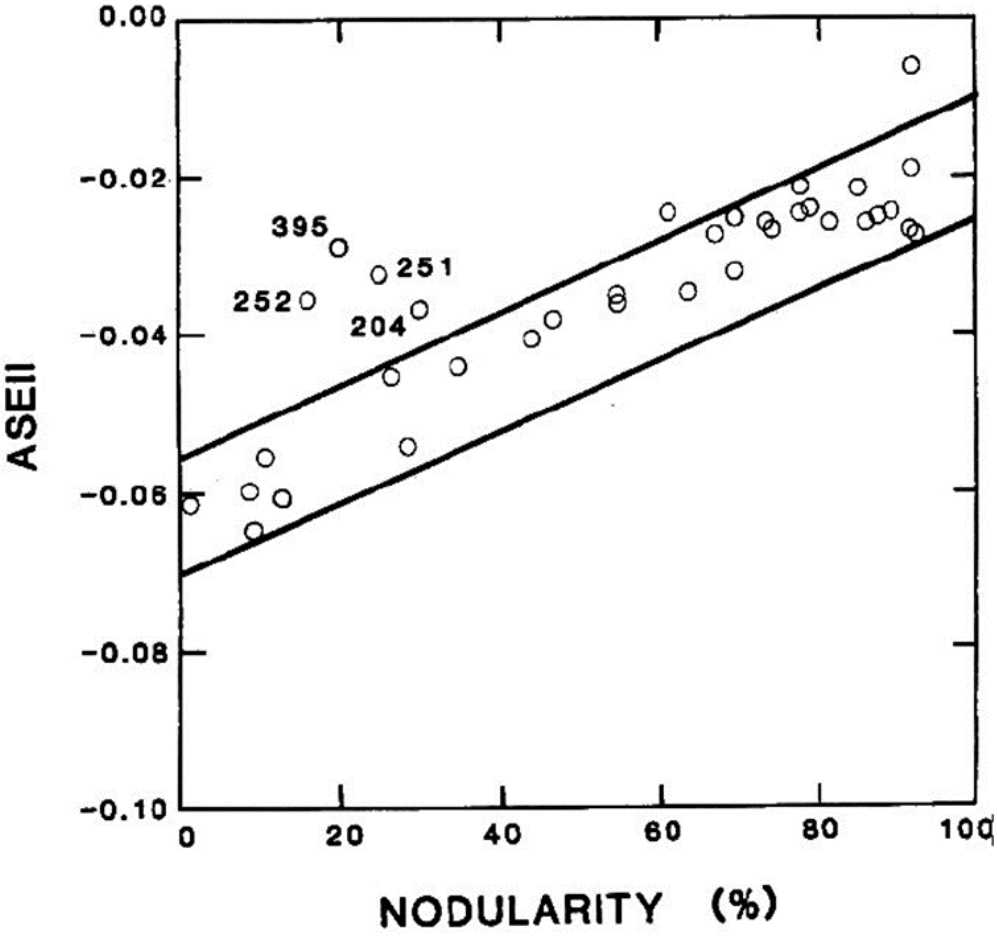

Figure 2.15. Correlation between a cooling curve parameter (ASE II) and resulting nodularity found by I. G. Chen and D. M. Stefanescu. [32]

Another microstructural property affecting the mechanical performance of nodular cast iron significantly is nodule count, and it is controlled by introducing heterogeneous nucleation sites (inoculant alloy particles) to the melt. As extra heterogeneous nucleation sites are introduced to the system, the amount of energy needed for nucleation reduces, and the amount of undercooling needed for eutectic transformation reduces [16, 27]. Therefore, eutectic transformation temperature observed on the cooling curve moves from metastable transformation temperature through stable transformation temperature as inoculation level of the melt increases.

In Figure 2.16, the effect of inoculation level of the melt on its cooling curve and the resulting microstructure was represented, and it is possible to mention that as inoculation level of the melt increases, the amount of undercooling seen on the cooling curve decreases, and the resulting graphite nodule count observed in the microstructure increases.

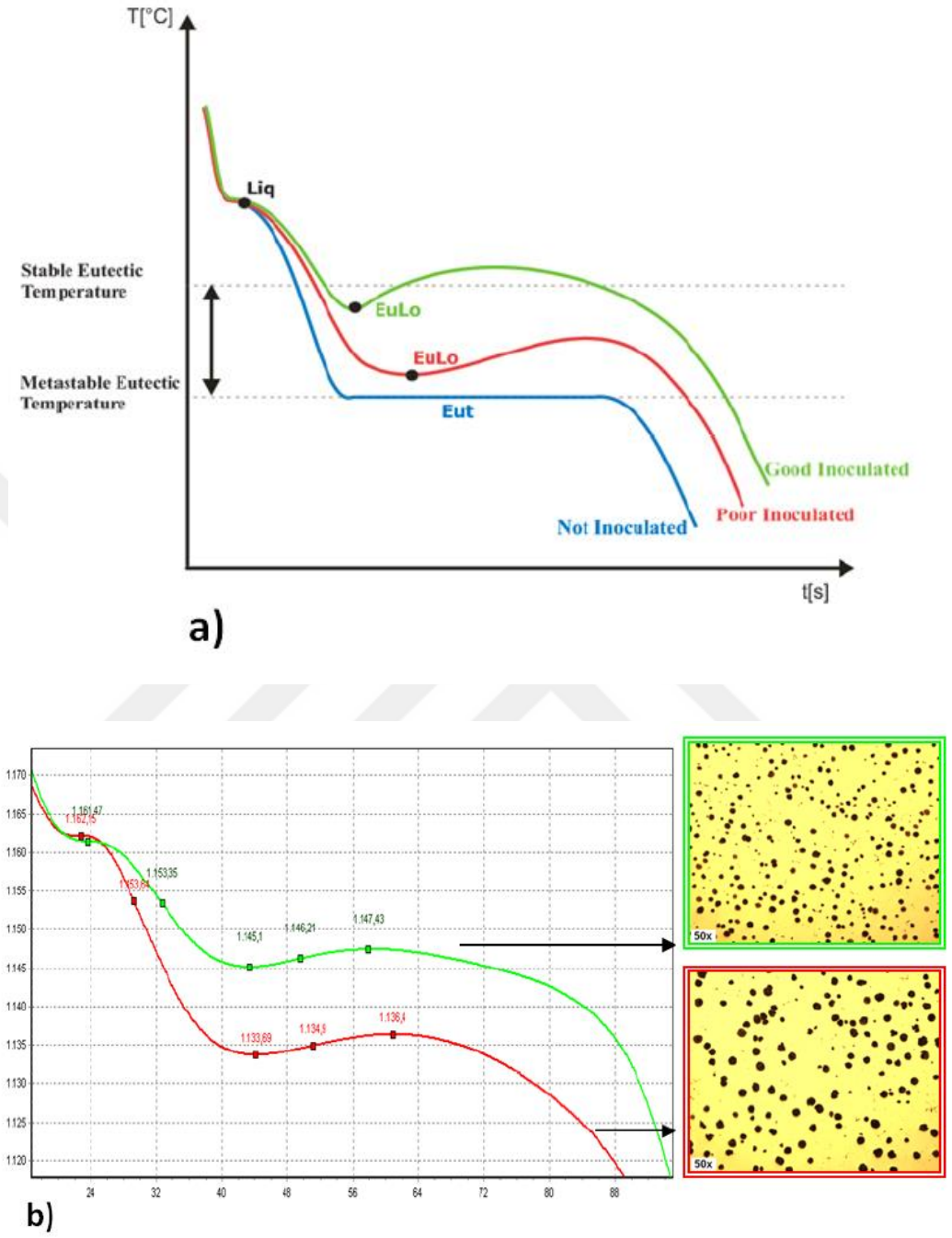

Figure 2.16. a) Representative cooling curves for the nodular cast iron melts in different inoculation states; b) representative cooling curves revealing the difference between cooling curves of poorly inoculated (red) and well inoculated (green) nodular cast iron melts and the resulting micrographs. [16]

A cooling curve thermal analysis cup is simply a thermocouple inserted mould (typically made of sand by using a binder) which lets us observe temperature versus time graph of the sample during cooling and solidification. The shape of the cooling curve is determined by the balance between the latent heat liberated during solidification and the heat lost to the surroundings [33]. Therefore, the design of the test cup has a significant effect on the results and their interpretation [33]. As shown in Figure 2.17, as the thickness of the cup sample decreases, undercooling increases due to the increasing cooling rate as a result of decreasing modulus [33]. Therefore, the effect of inoculation is more noticeable on the smaller size cups [33].

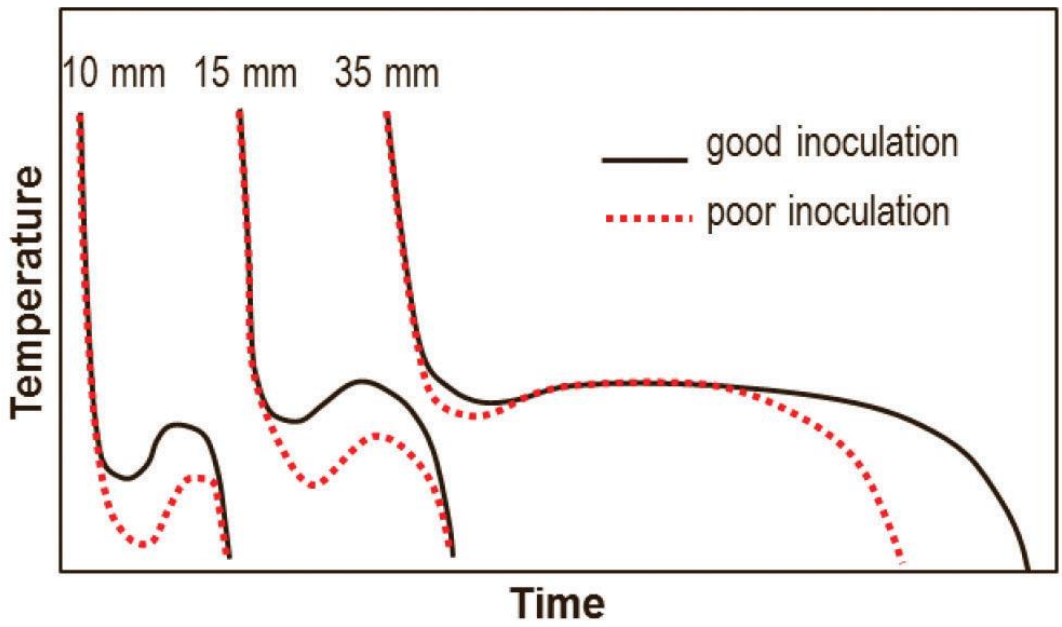

Figure 2.17. Schematic representation of the effect of cup sample thickness and state of inoculation on the shape of the cooling curve of eutectic nodular cast iron melt. [33]

2.6. Active Oxygen Amount in Nodular Cast Iron

Oxygen found in nodular cast iron melt can be divided into two main groups which are the oxygen content found in elemental form (also called active oxygen) and the oxygen content found in chemical compounds (also called chemically bonded oxygen) [34, 35]. Chemically bonded oxygen amount corresponds to the number of oxide particles acting as heterogeneous nucleation sites for the graphite particles where active oxygen amount relates the surface tension of iron and its interfacial energy with graphite [36]. Therefore, in the nodular cast iron melt, too less oxygen content leads to lack of heterogeneous nucleation sites for the graphite particles, and results in an undesired microstructure where too high oxygen content leads to low interfacial energy between iron and graphite which also results in an undesired microstructure [36]. For this reason, oxygen content of the nodular cast iron melt needs to be optimized for the desired microstructural properties.

Total amount of oxygen in a nodular cast iron specimen can be analyzed by combustion analysis (LECO) tools. It is possible to measure the active oxygen amount in nodular cast iron melt by special sensors with an electrochemical cell and a Pt-PtRh (S-type) thermocouple [37]. The cell contains $Cr\text{-}Cr_2O_3$ as solid reference cell in contact with MgO-stabilized ZrO_2 solid-state electrolyte [37]. When the sensor is immersed into the bath, an electrode made of iron contacts with the melt, and an electro-voltaic cell is formed in between the reference cell and the melt [37]. A device collecting the potential difference produced by the cell calculates the oxygen activity [37].

The formula given in Equation 2.3 was established by the manufacturer (Heraeus Electro-Nite Intl. NV) by modifying the Nernst equation with the known partial pressure of oxygen in the reference cell [38].

Equation 2.3. $\log aO = 8.62 - \{13580 - 10.08\,(E + 24)\} / T$

Where aO is the oxygen activity of the melt, and it is considered as equal to the active oxygen amount (in ppm), E is the electrical potential (in mV) produced by the cell, and T is temperature (in °C) of the melt measured by Pt-PtRh thermocouple embedded to the sensor [38].

A comprehensive study, aimed to find a relation between oxygen activity of the treated nodular cast iron melt and the resulting microstructural properties, was conducted by F. Mampaey et al. [37]. The results for three different melts are revealed in Figure 2.18. Although it is obvious that there is a correlation, neither equation of the correlation curve nor the correlation coefficient was published.

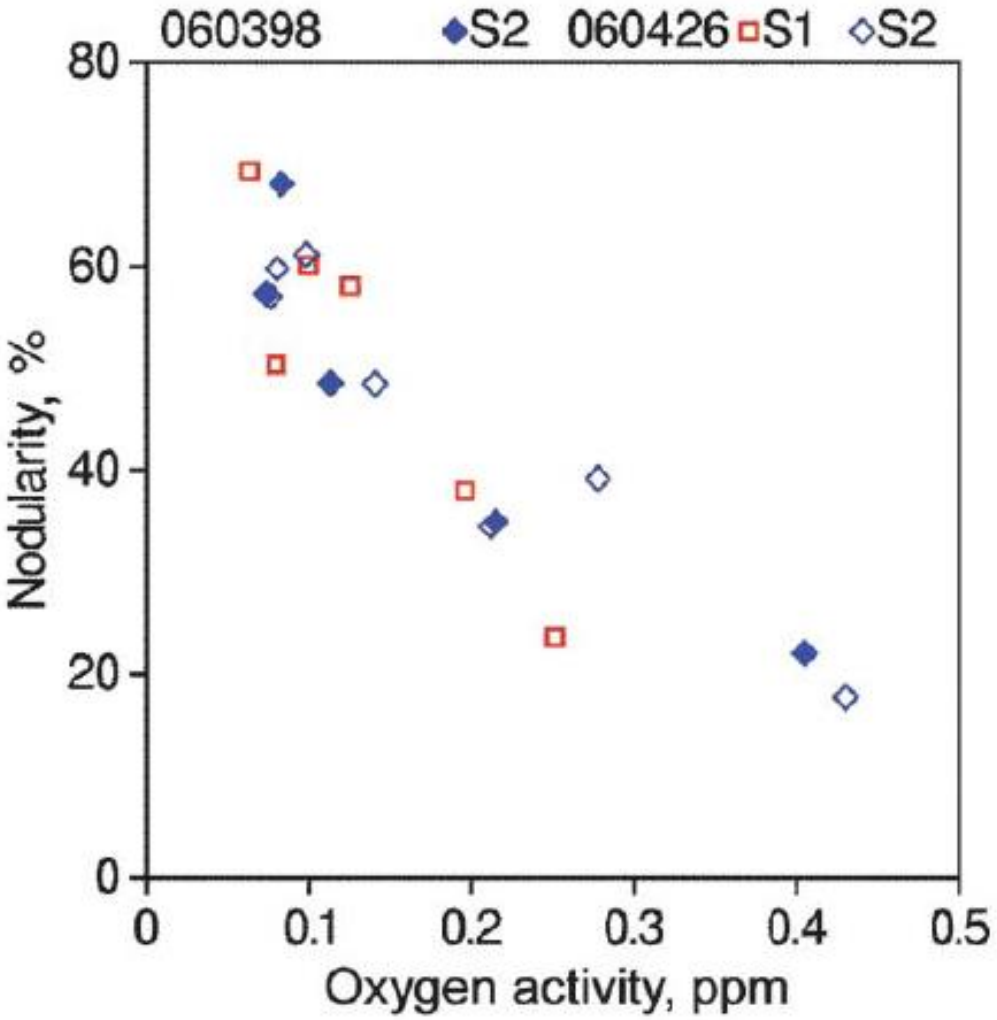

Figure 2.18. The relation between active oxygen content of the nodular cast iron melt and the resulting nodularity found by F. Mampaey et al. via the investigation of 3 different nodular cast iron melts. [37]

CHAPTER 3

EQUIPMENTS, SAMPLES AND METHODOLOGY

3.1.Nodular Cast Iron Production Process

Mechanical performance of the fully ferritic nodular cast iron grades is highly dependent on the nodularity and the nodule count which are much more difficult to control than that the pearlite content is. Therefore, two fully ferritic nodular cast iron grades which are EN-GJS-400-15 and EN-GJS-600-10C were investigated. EN-GJS-600-10C is one of the new generation solution strengthened ferritic ductile iron (SSFDI) grades which has mechanical properties competitive with medium-carbon-steel grades, and a dedicated process control method is needed to ensure its resulting performance.

Because they are highly preferred in the industry, the investigations were made on hypoeutectic compositions.

To obtain results which are applicable to the industry, experimental data were collected from the usual production of the foundry Ferromatrix NV.

Approximately 4 tons of base iron for nodular cast iron was prepared by using a medium frequency induction furnace by charging pig iron for nodular cast iron which has a sulphur content less than 0.02wt%, steel scrap to decrease the carbon content, nodular cast iron returns to recycle and ferroalloys to achieve the aimed chemical composition of the grades. To achieve the desired graphite shape while keeping the inoculation potential above the critical state, sulphur content of the base iron was kept at a degree of 0.01wt%. To keep the solidification shrinkage at a low level without introducing tendency for undesired graphite forms, carbon equivalent of the base iron was kept at a degree of 4.2wt% which is near to the upper limit of hypoeutectic composition. The melting process was repeated 23

times (11 times for the alloy EN-GJS-400-18 and 12 times for the alloy EN-GJS-600-10C).

After the charge was melted and reached to a temperature around 1500°C, approximately 2000 kg of base iron is tapped to a preheated ladle, and a forklift brought it to the ladle station for the Mg treatment. At the ladle station, open top of the ladle was closed with a refractory lined steel cover which prevents splashing and lowers the loss in heat, also the alloying elements in gas form. On the ladle cover, there were three channels. One inlet for the cored wire with Mg master alloy, one inlet for the cored wire with inoculant master alloy and one outlet for the gas products of the reactions. The ladle is weighed by scale integrated to the forklift and the net liquid base iron is calculated by subtracting the tare. The cored wires with Mg and inoculant master alloys were fed by two electric motors simultaneously. The length of the cored wires was calculated such that 0.42wt% percent of Mg master alloy and 0.30wt% of inoculant master alloy were introduced. After the treatment was completed, the ladle was moved to the deslagging station. Fluidity of the slag which floats on the surface of liquid iron was increased with the help of a flux (limestone), then deslagging was performed to prevent dross inclusions. The ladle process was repeated 40 times (20 ladles for the alloy EN-GJS-400-18 and 20 ladles for the alloy EN-GJS-600-10C) so that 20 heats for each grade were investigated. Chemical compositions of the cored wires with Mg and inoculant mater alloys were revealed in Table 3.1 and Table 3.2 respectively.

Table 3.1. *Chemical composition of the cored wire with Mg master alloy.*

Cored Wire (g/m): 410			
Unit Powder (Core) (g/m): 252			
Content of the Core:			
Si (%)	Mg (%)	Ca (%)	Others (%)
50.4	25.8	4.2	19.6
Content per unit length:			
Si (g/m)	Mg (g/m)	Ca (g/m)	Others (g/m)
127.0	65.0	10.7	49.3

Table 3.2. *Chemical composition of the cored wire with inoculation master alloy.*

Cored Wire (g/m): 436					
Unit Powder (Core) (g/m): 266					
Content of the Core:					
Si (%)	Ca (%)	Bi (%)	Al (%)	Rare Earth (%)	Others (%)
67.2	1.4	0.9	0.8	0.7	29.0
Content per unit length					
Si (g/m)	Ca (g/m)	Bi (g/m)	Al (g/m)	Rare Earth (g/m)	Others (g/m)
178.8	3.7	2.4	2.1	1.9	77.1

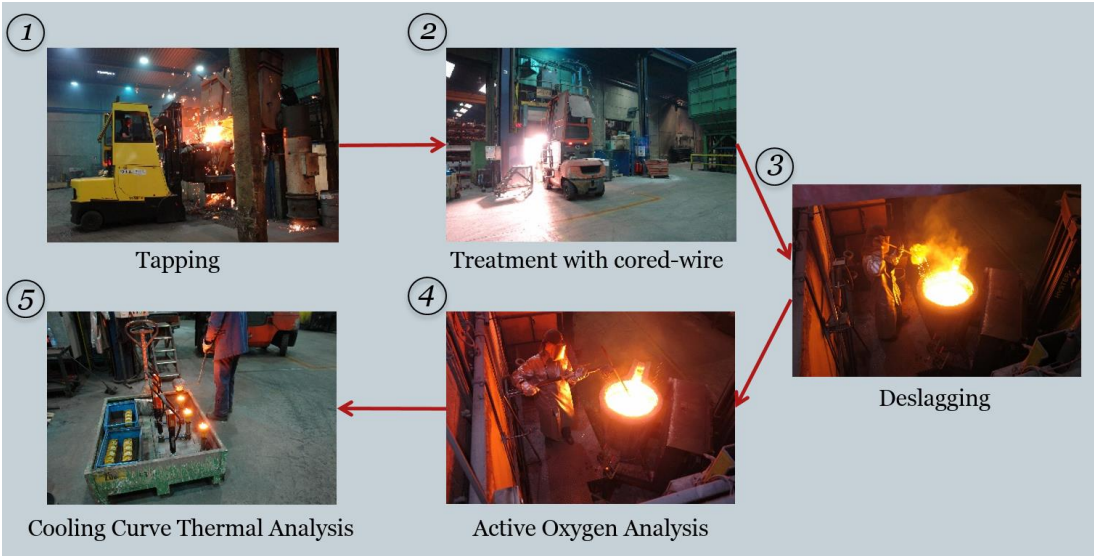

Figure 3.1. Schematic representation of the process cycle applied for each ladle.

3.2. Active Oxygen Amount Measurement in Nodular Cast Iron Melt

For the active oxygen amount measurement in liquid cast iron, Celox Foundry™ disposable sensors provided by Heraeus Electro-Nite Intl. NV were used. The sensor contains an electro-voltaic cell and an S-type (Pt-PtRh10) thermocouple [37]. The electro-voltaic cell contains an anode electrode made of molybdenum connected to a closed end tube filled with Cr-Cr_2O_3 mixture as oxygen reference material in contact with magnesia stabilized zirconia (MSZ) as a solid-state electrolyte [37]. When the sensor is immersed in the bath, the cathode electrode which is made of iron contacts with the melt, and an electro-voltaic cell is formed between the oxygen reference cell and the melt [37].

A dedicated vibration lance for the accurate measurement of quite low oxygen activities which are typical for Mg treated cast iron and a CF LabE-IV™ device (provided by Heraeus Electro-Nite Intl. NV) collecting the potential differences produced by the electrochemical cell and calculating the oxygen activity by a formula based on Nernst equation was used [37]. The system was always calibrated before the use.

Active oxygen amount measurement of treated nodular cast iron melt was performed in the ladle right after the deslagging. In total, 40 active oxygen amount measurements (1 for each heat, 20 for each alloy grade) were performed.

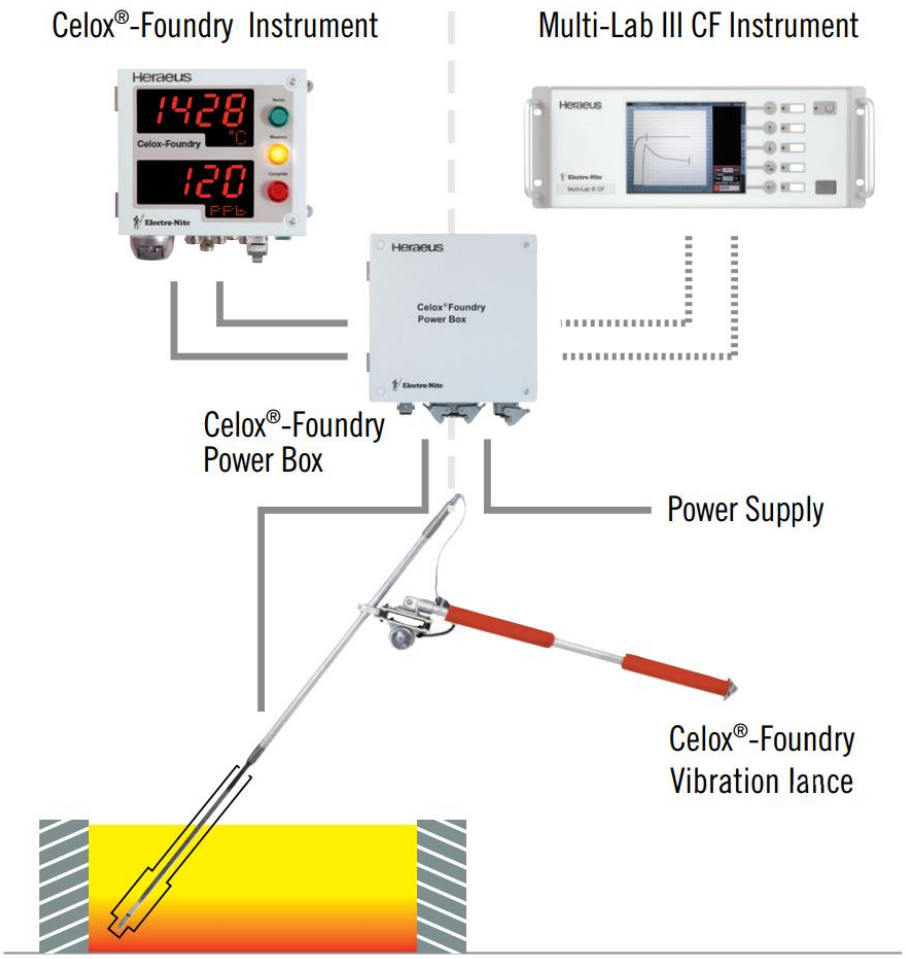

Figure 3.2. Schematic representation of Celox Foundry™ equipment. [38]

3.3. Cooling Curve Thermal Analysis of Nodular Cast Iron Melt

For the cooling curve thermal analysis of nodular cast iron melt, recently developed thermal analysis cups QuiKCup Cover™ provided by Heraeus Electro-Nite Intl. NV were used (see Figure 3.3). QuiKCup Cover™ is a closed cup with a cover on top which ensures the consistency of sample volume and cooling conditions and decreases eventual variations in the results [39]. The ingate between cover and cup chamber is closed by tapes from both inner and outer side, so that it is possible to insert additives such as inoculant between those two tapes, and those additives are dissolved homogeneously by the liquid alloy flowing through the ingate (see Figure 3.4) [39]. QuiKCup Cover™ has a 12 mm of sample thickness which is less than half of that the conventional cups do, and decreased sample thickness ensures a more obvious and comparable eutectic undercooling which is normally quite low for the solidification of inoculated nodular cast iron melt [39]. QuiKCup Cover™ contains a K-type (Chromel-Alumel) thermocouple with an accuracy of +/- 0.2°C which is five times more accurate than the conventional cups, and higher thermocouple accuracy promises more accurate experimental data [39].

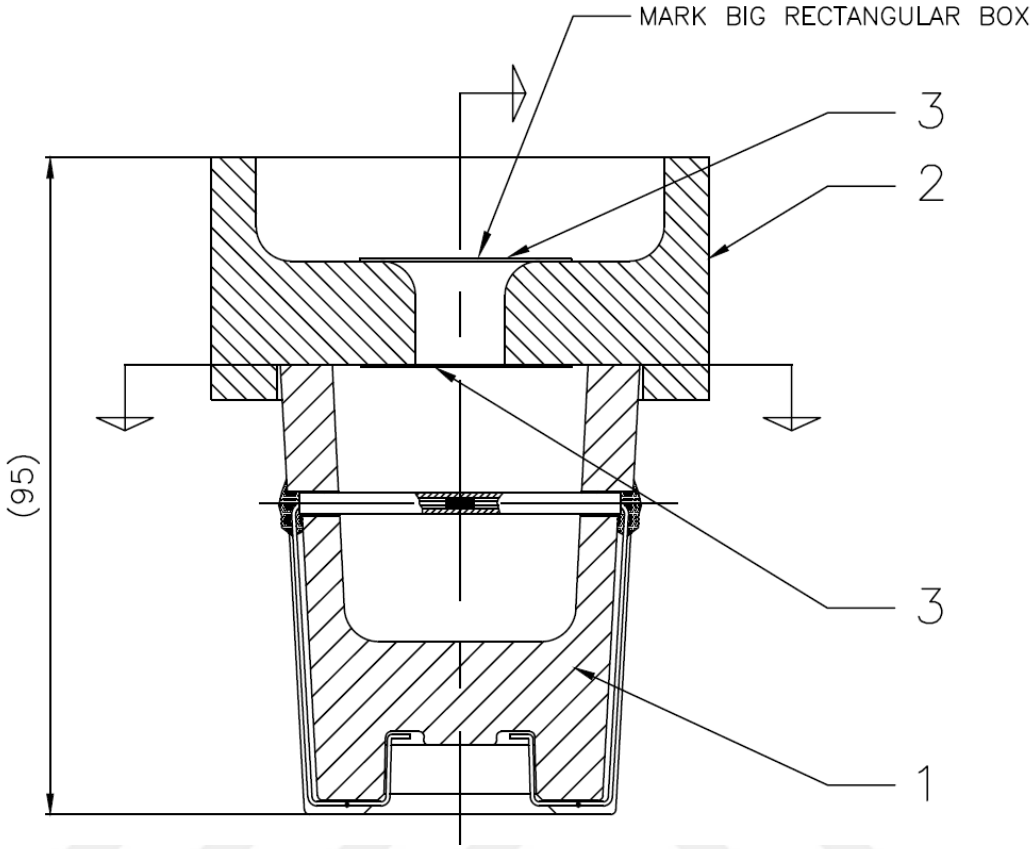

Figure 3.3. Drawing of the QuiKCup Cover™ cut by the vertical middle plan (units: mm). 1- Shell sand body; 2- Shell sand cover; 3- Tapes holding the inoculant at the ingate. [39]

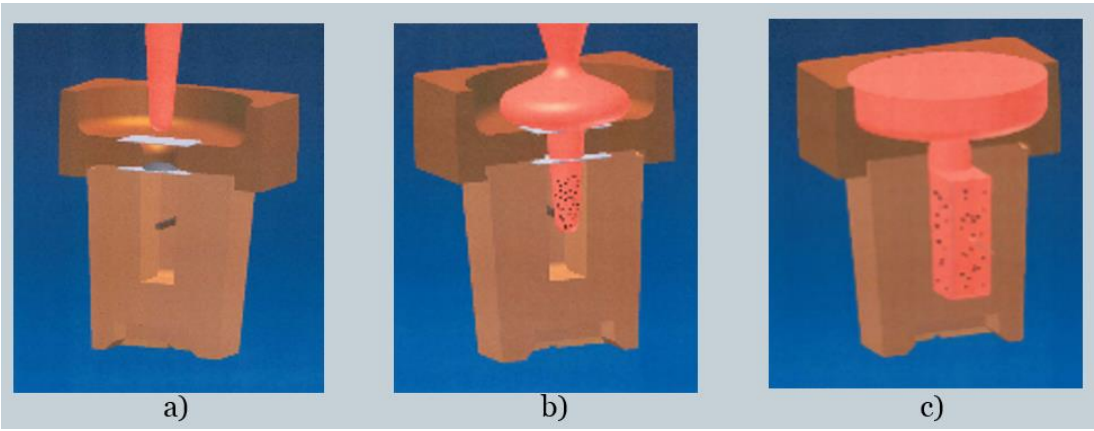

Figure 3.4. Illustration for the mixing of the additives inserted to the ingate of QuiKCup Cover™. a) Right before the molten metal contacts to the cover; b) During the filling; c) Filled sample with homogeneously mixed additive. [39]

QuiKLabE-IV™ devices (provided by Heraeus Electro-Nite Intl. NV) collecting the potential differences produced by the thermocouple in the cup, converting them to the corresponding temperature values and sending to the computer via Ethernet connection were used [39]. The system was always calibrated before the use.

On the computer, a software MeltControl2020™ (provided by Heraeus Electro-Nite Intl. NV) processing the incoming raw data, constructing temperature versus time graph and its first derivative by applying a curve smoothing algorithm and identifying the peculiarities on the curve was used [39]. The description and nomenclature of the cooling curve parameters identified by the software were listed in Table 3.3. The software saves all curves in a database and allows the export of the saved data to MS Office Excel for further data evaluation.

Table 3.3. *Description and nomenclature of the cooling curve parameters identified by MeltControl2020™. [39]*

Abbreviation	Unit	Signification
TP	(°C)	Maximum temperature measured by the thermocouple
TP_dT	(°C/s)	Cooling rate at TP point
TP_t	(s)	Time at TP point
TL	(°C)	Liquidus temperature corresponding to the local minimum at the derivative curve
TL_dT	(°C/s)	Cooling rate at TL point
TL_t	(s)	Time at TL point
TI	(°C)	Temperature between the liquidus and eutectic point with the highest cooling rate
TI_dT	(°C/s)	Cooling rate at TI point
TI_t	(s)	Time at TI point
TEmin	(°C)	Minimum temperature measured before the eutectic point
TEmin_t	(s)	Time at TEmin point
TEmax	(°C)	Maximum temperature measured after the eutectic point
TEmax_t	(s)	Time at TEmax point
TE	(°C)	Eutectic temperature corresponding to the local minimum in the derivative curve
TE_dT	(°C/s)	Cooling rate at TE point
TE_t	(s)	Time at TE point
TS	(°C)	Eutectic temperature (in the case of white solidification)
TF	(°C)	End of solidification temperature corresponding to the maximum cooling rate
TF_dT	(°C/s)	Cooling rate at TF point
TF_t	(s)	Time at TF point
DT	(°C)	Eutectic undercooling (1150°C - TEmin)
DTM	(°C)	Eutectic recalescence (TEmax - TEmin)
DTM_t	(s)	Eutectic recalescence duration (TEmax_t - TEmin_t)
TE_A	(°)	The angle between ITEmin,TEmaxI line and X-axis (arctan(DTM/DTM_t))
TE_Z	(°C*s)	Area of the eutectic recalescence triangle (DTM * DTM_t / 2)
FL_t	(s)	Duration of solidification (TF_t - TL_t)

To obtain varied cooling curves and microstructural properties, thermal analysis cups with different additive contents were used. Two sets of data were collected. For the first dataset, there were four thermal analysis stations for each heat; 1) Plain cup, 2) The cup containing 0.05wt% Spherix^{TM} inoculant (provided by FerroAtlantica SL), 3) The cup containing 0.05wt% Spherix-Plus^{TM} inoculant (provided by FerroAtlantica SL) and 4) The cup containing 0.05wt% SMW 605^{TM} inoculant (provided by ASK Chemicals GmbH). For the second dataset, there were five thermal analysis stations for each heat; 1) Plain cup, 2) The cup containing 0.05wt% Spherix^{TM} inoculant (provided by FerroAtlantica SL), 3) The cup containing 0.10wt% Spherix^{TM} inoculant, 4) The cup containing 0.15wt% Spherix^{TM} inoculant and 5) The cup containing 0.4wt% Te and 0.3wt% S providing white (metastable) solidification to obtain eutectic transformation temperature of white solidification which might be useful to eliminate the effect of Si content on the curve parameters. To ensure the homogeneous mixing of the inoculants at the cup ingate, the inoculants were sieved, and the ones in a size range of 125 µ and 355 µ were used. Chemical compositions of the inoculants which were used as additives at the cup ingate are revealed in Table 3.4. In total, 160 cooling curves thermal analysis of grey (stable) solidification (4 for each heat, 80 for each alloy grade) and 20 cooling curve thermal analysis of white solidification (1 for each heat of the second dataset, 10 for each alloy grade) were conducted (see Table 3.5).

Table 3.4. *Chemical composition of the inoculants which were used as additives at the cup ingate.*

Inoculant	*Spherix*	*Spherix-plus*	*SMW605*
Si (%)	67.2	67.5	65.1
Ca (%)	1.4	1.6	2.1
Bi (%)	0.9	-	1.0
Al (%)	0.8	0.8	0.8
Rare Earth (%)	0.7	0.7	1.0
Sb (%)	-	0.9	-
Others (%)	29.0	28.5	30.0

Table 3.5. *List of the cooling curve thermal analysis samples.*

Alloy ID	Charge #	Ladle #	Cup #	Content ID	Content (%)
EN-GJS-400-18	1	1	1	Spherix	0.05
EN-GJS-400-18	1	1	2	Spherix+	0.05
EN-GJS-400-18	1	1	3	SMW605	0.05
EN-GJS-400-18	1	1	4	-	-
EN-GJS-400-18	2	2	5	Spherix	0.05
EN-GJS-400-18	2	2	6	Spherix+	0.05
EN-GJS-400-18	2	2	7	SMW605	0.05
EN-GJS-400-18	2	2	8	-	-
EN-GJS-400-18	2	3	9	Spherix	0.05
EN-GJS-400-18	2	3	10	Spherix+	0.05
EN-GJS-400-18	2	3	11	SMW605	0.05
EN-GJS-400-18	2	3	12	-	-
EN-GJS-400-18	3	4	13	Spherix	0.05
EN-GJS-400-18	3	4	14	Spherix+	0.05
EN-GJS-400-18	3	4	15	SMW605	0.05
EN-GJS-400-18	3	4	16	-	-
EN-GJS-400-18	4	5	17	Spherix	0.05
EN-GJS-400-18	4	5	18	Spherix+	0.05
EN-GJS-400-18	4	5	19	SMW605	0.05
EN-GJS-400-18	4	5	20	-	-
EN-GJS-400-18	4	6	21	Spherix	0.05
EN-GJS-400-18	4	6	22	Spherix+	0.05
EN-GJS-400-18	4	6	23	SMW605	0.05
EN-GJS-400-18	4	6	24	-	-
EN-GJS-400-18	5	7	25	Spherix	0.05
EN-GJS-400-18	5	7	26	Spherix+	0.05
EN-GJS-400-18	5	7	27	SMW605	0.05
EN-GJS-400-18	5	7	28	-	-
EN-GJS-400-18	5	8	29	Spherix	0.05
EN-GJS-400-18	5	8	30	Spherix+	0.05
EN-GJS-400-18	5	8	31	SMW605	0.05
EN-GJS-400-18	5	8	32	-	-
EN-GJS-400-18	6	9	33	Spherix	0.05
EN-GJS-400-18	6	9	34	Spherix+	0.05
EN-GJS-400-18	6	9	35	SMW605	0.05
EN-GJS-400-18	6	9	36	-	-

EN-GJS-400-18	6	10	37	Spherix	0.05
EN-GJS-400-18	6	10	38	Spherix+	0.05
EN-GJS-400-18	6	10	39	SMW605	0.05
EN-GJS-400-18	6	10	40	-	-
EN-GJS-400-18	7	11	41	-	-
EN-GJS-400-18	7	11	42	Spherix	0.05
EN-GJS-400-18	7	11	43	Spherix	0.10
EN-GJS-400-18	7	11	44	Spherix	0.15
EN-GJS-400-18	7	11	W1	Te + S	0.4 + 0.3
EN-GJS-400-18	7	12	45	-	-
EN-GJS-400-18	7	12	46	Spherix	0.05
EN-GJS-400-18	7	12	47	Spherix	0.10
EN-GJS-400-18	7	12	48	Spherix	0.15
EN-GJS-400-18	7	12	W2	Te + S	0.4 + 0.3
EN-GJS-400-18	8	13	49	-	-
EN-GJS-400-18	8	13	50	Spherix	0.05
EN-GJS-400-18	8	13	51	Spherix	0.10
EN-GJS-400-18	8	13	52	Spherix	0.15
EN-GJS-400-18	8	13	W3	Te + S	0.4 + 0.3
EN-GJS-400-18	8	14	53	-	-
EN-GJS-400-18	8	14	54	Spherix	0.05
EN-GJS-400-18	8	14	55	Spherix	0.10
EN-GJS-400-18	8	14	56	Spherix	0.15
EN-GJS-400-18	8	14	W4	Te + S	0.4 + 0.3
EN-GJS-400-18	9	15	57	-	-
EN-GJS-400-18	9	15	58	Spherix	0.05
EN-GJS-400-18	9	15	59	Spherix	0.10
EN-GJS-400-18	9	15	60	Spherix	0.15
EN-GJS-400-18	9	15	W5	Te + S	0.4 + 0.3
EN-GJS-400-18	9	16	61	-	-
EN-GJS-400-18	9	16	62	Spherix	0.05
EN-GJS-400-18	9	16	63	Spherix	0.10
EN-GJS-400-18	9	16	64	Spherix	0.15
EN-GJS-400-18	9	16	W6	Te + S	0.4 + 0.3
EN-GJS-400-18	10	17	65	-	-
EN-GJS-400-18	10	17	66	Spherix	0.05
EN-GJS-400-18	10	17	67	Spherix	0.10
EN-GJS-400-18	10	17	68	Spherix	0.15
EN-GJS-400-18	10	17	W7	Te + S	0.4 + 0.3

EN-GJS-400-18	10	18	69	-	-
EN-GJS-400-18	10	18	70	Spherix	0.05
EN-GJS-400-18	10	18	71	Spherix	0.10
EN-GJS-400-18	10	18	72	Spherix	0.15
EN-GJS-400-18	10	18	W8	Te + S	0.4 + 0.3
EN-GJS-400-18	11	19	73	-	-
EN-GJS-400-18	11	19	74	Spherix	0.05
EN-GJS-400-18	11	19	75	Spherix	0.10
EN-GJS-400-18	11	19	76	Spherix	0.15
EN-GJS-400-18	11	19	W9	Te + S	0.4 + 0.3
EN-GJS-400-18	11	20	77	-	-
EN-GJS-400-18	11	20	78	Spherix	0.05
EN-GJS-400-18	11	20	79	Spherix	0.10
EN-GJS-400-18	11	20	80	Spherix	0.15
EN-GJS-400-18	11	20	W10	Te + S	0.4 + 0.3
EN-GJS-600-10C	12	21	81	Spherix	0.05
EN-GJS-600-10C	12	21	82	Spherix+	0.05
EN-GJS-600-10C	12	21	83	SMW605	0.05
EN-GJS-600-10C	12	21	84	-	-
EN-GJS-600-10C	13	22	85	Spherix	0.05
EN-GJS-600-10C	13	22	86	Spherix+	0.05
EN-GJS-600-10C	13	22	87	SMW605	0.05
EN-GJS-600-10C	13	22	88	-	-
EN-GJS-600-10C	13	23	89	Spherix	0.05
EN-GJS-600-10C	13	23	90	Spherix+	0.05
EN-GJS-600-10C	13	23	91	SMW605	0.05
EN-GJS-600-10C	13	23	92	-	-
EN-GJS-600-10C	14	24	93	Spherix	0.05
EN-GJS-600-10C	14	24	94	Spherix+	0.05
EN-GJS-600-10C	14	24	95	SMW605	0.05
EN-GJS-600-10C	14	24	96	-	-
EN-GJS-600-10C	15	25	97	Spherix	0.05
EN-GJS-600-10C	15	25	98	Spherix+	0.05
EN-GJS-600-10C	15	25	99	SMW605	0.05
EN-GJS-600-10C	15	25	100	-	-
EN-GJS-600-10C	15	26	101	Spherix	0.05
EN-GJS-600-10C	15	26	102	Spherix+	0.05
EN-GJS-600-10C	15	26	103	SMW605	0.05
EN-GJS-600-10C	15	26	104	-	-

EN-GJS-600-10C	16	27	105	Spherix	0.05
EN-GJS-600-10C	16	27	106	Spherix+	0.05
EN-GJS-600-10C	16	27	107	SMW605	0.05
EN-GJS-600-10C	16	27	108	-	-
EN-GJS-600-10C	17	28	109	Spherix	0.05
EN-GJS-600-10C	17	28	110	Spherix+	0.05
EN-GJS-600-10C	17	28	111	SMW605	0.05
EN-GJS-600-10C	17	28	112	-	-
EN-GJS-600-10C	17	29	113	Spherix	0.05
EN-GJS-600-10C	17	29	114	Spherix+	0.05
EN-GJS-600-10C	17	29	115	SMW605	0.05
EN-GJS-600-10C	17	29	116	-	-
EN-GJS-600-10C	18	30	117	Spherix	0.05
EN-GJS-600-10C	18	30	118	Spherix+	0.05
EN-GJS-600-10C	18	30	119	SMW605	0.05
EN-GJS-600-10C	18	30	120	-	-
EN-GJS-600-10C	19	31	121	-	-
EN-GJS-600-10C	19	31	122	Spherix	0.05
EN-GJS-600-10C	19	31	123	Spherix	0.10
EN-GJS-600-10C	19	31	124	Spherix	0.15
EN-GJS-600-10C	19	31	W11	Te + S	0.4 + 0.3
EN-GJS-600-10C	19	32	125	-	-
EN-GJS-600-10C	19	32	126	Spherix	0.05
EN-GJS-600-10C	19	32	127	Spherix	0.10
EN-GJS-600-10C	19	32	128	Spherix	0.15
EN-GJS-600-10C	19	32	W12	Te + S	0.4 + 0.3
EN-GJS-600-10C	20	33	129	-	-
EN-GJS-600-10C	20	33	130	Spherix	0.05
EN-GJS-600-10C	20	33	131	Spherix	0.10
EN-GJS-600-10C	20	33	132	Spherix	0.15
EN-GJS-600-10C	20	33	W13	Te + S	0.4 + 0.3
EN-GJS-600-10C	20	34	133	-	-
EN-GJS-600-10C	20	34	134	Spherix	0.05
EN-GJS-600-10C	20	34	135	Spherix	0.10
EN-GJS-600-10C	20	34	136	Spherix	0.15
EN-GJS-600-10C	20	34	W14	Te + S	0.4 + 0.3
EN-GJS-600-10C	21	35	137	-	-
EN-GJS-600-10C	21	35	138	Spherix	0.05
EN-GJS-600-10C	21	35	139	Spherix	0.10

EN-GJS-600-10C	21	35	140	Spherix	0.15
EN-GJS-600-10C	21	35	W15	Te + S	0.4 + 0.3
EN-GJS-600-10C	21	36	141	-	-
EN-GJS-600-10C	21	36	142	Spherix	0.05
EN-GJS-600-10C	21	36	143	Spherix	0.10
EN-GJS-600-10C	21	36	144	Spherix	0.15
EN-GJS-600-10C	21	36	W16	Te + S	0.4 + 0.3
EN-GJS-600-10C	22	37	145	-	-
EN-GJS-600-10C	22	37	146	Spherix	0.05
EN-GJS-600-10C	22	37	147	Spherix	0.10
EN-GJS-600-10C	22	37	148	Spherix	0.15
EN-GJS-600-10C	22	37	W17	Te + S	0.4 + 0.3
EN-GJS-600-10C	22	38	149	-	-
EN-GJS-600-10C	22	38	150	Spherix	0.05
EN-GJS-600-10C	22	38	151	Spherix	0.10
EN-GJS-600-10C	22	38	152	Spherix	0.15
EN-GJS-600-10C	22	38	W18	Te + S	0.4 + 0.3
EN-GJS-600-10C	23	39	153	-	-
EN-GJS-600-10C	23	39	154	Spherix	0.05
EN-GJS-600-10C	23	39	155	Spherix	0.10
EN-GJS-600-10C	23	39	156	Spherix	0.15
EN-GJS-600-10C	23	39	W19	Te + S	0.4 + 0.3
EN-GJS-600-10C	23	40	157	-	-
EN-GJS-600-10C	23	40	158	Spherix	0.05
EN-GJS-600-10C	23	40	159	Spherix	0.10
EN-GJS-600-10C	23	40	160	Spherix	0.15
EN-GJS-600-10C	23	40	W20	Te + S	0.4 + 0.3

3.4. Metallographic Evaluation

After the sampling was made, samples from the thermal analysis cups were labeled indicating the heat number and the cup content. All the cups with grey solidification (160 cups) were subjected to metallographic sampling, specimen preparation and image analysis. After cleaning the sand from the sample's surface, it was cut from its horizontal plane from approximately 2 mm below the quartz tube of the thermocouple by using an abrasive cutter with boron-based cooling liquid. The lower part of each cut samples was used for the metallographic

investigation on the cut surface as presented in Figure 3.5. Since it has the microstructure most corresponding to the obtained cooling curve, the closest part possible without having quartz inclusions was chosen. After molding the samples into Epoxy, standard metallographic specimen preparation steps were followed. Grinding for 1 minute by 120 mesh grinding paper, for 1 minute by 200 mesh grinding paper, for 1 minute by 600 mesh grinding paper and for 2 minutes by 800 mesh grinding paper were applied respectively by washing the samples after each step. Polishing for 9 minutes by using 3 µm diamond suspension was applied, then the surface was cleaned with Ethanol and dried with hot air. The grinding and polishing operations were done by using Abramin™ machine, grinding papers and DiaProPlus™ polishing suspension all provided by Struers GmbH. Metallographic evaluation was done right after polishing and cleaning to observe the graphite phase clearly. Then, the specimens were etched for approximately 4 seconds by using 2vol% Nital Ethanol solution for the investigation of the matrix. The specimens were investigated under a 3-megapixel digital camera mounted to Nikon OptiPhot™ metallographic microscope using 5x, 10x, 20x or 50x magnifications. The metallographic evaluation of the specimens was conducted by using the image analysis software Micr-O-Phase™ provided by Heraeus Electr-Nite Intl. NV. The software gets the micrographs directly from the camera mounted to microscope which was calibrated by using a scale with 10 µm of sub-divisions, and the information of used magnification is shared by the software [40]. The pixel size in a micrograph is a function of camera's resolution and the used magnification [40]. Since the software has the necessary information, it is able to calculate distances and areas by counting the pixels and using the pixel size [40]. Then, by using several algorithms, the software analyses all the metallographic parameters such as nodularity, nodule count, phase area of graphite, graphite shape classification, ferrite and pearlite ratios all according to the norm EN-ISO-945-1 [40].

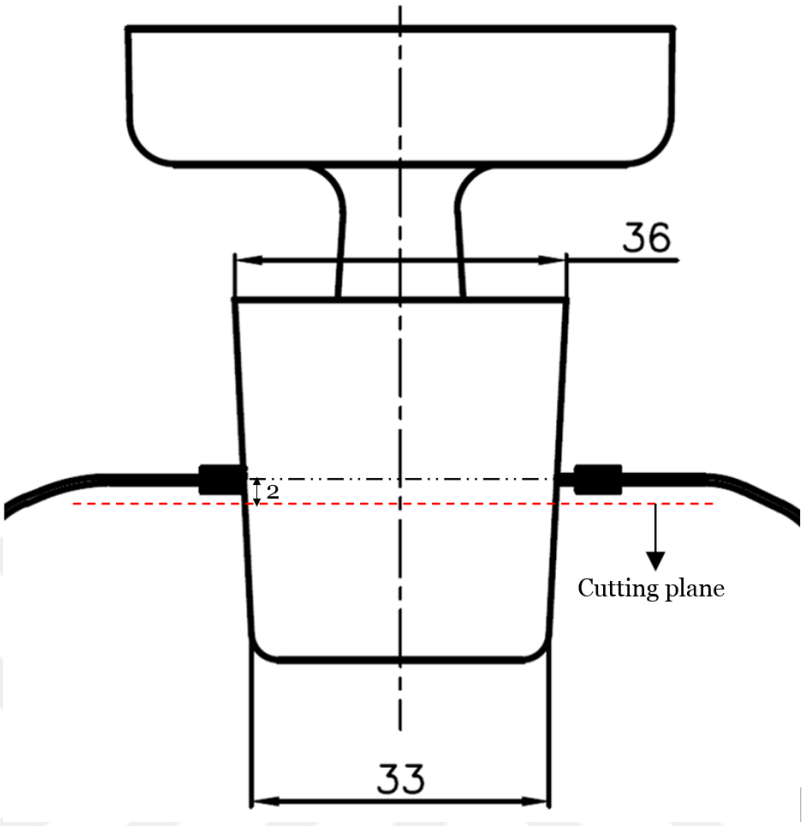

Figure 3.5. Drawing the QuiKCup Cover™ sample and scheme showing how the sample was cut (units: mm). [39]

3.5. Tensile Test

From each heat, one separate 25 mm Y2-block sample was poured to a sand mould after the deslagging, together with the thermal analysis cups. 40 Y2-blocks (1 for each heat, 20 for each grade) for the tensile test were collected. The bottom portion of Y2-block samples were cut and machined as tensile test specimens by using a CNC lathe machine. Schematic representation of an Y2-block is shown in Figure 3.6. Tensile tests were conducted according to EN-ISO-6892 Standards at room temperature by using an MTS Model 810 230 KN hydraulic tension tester.

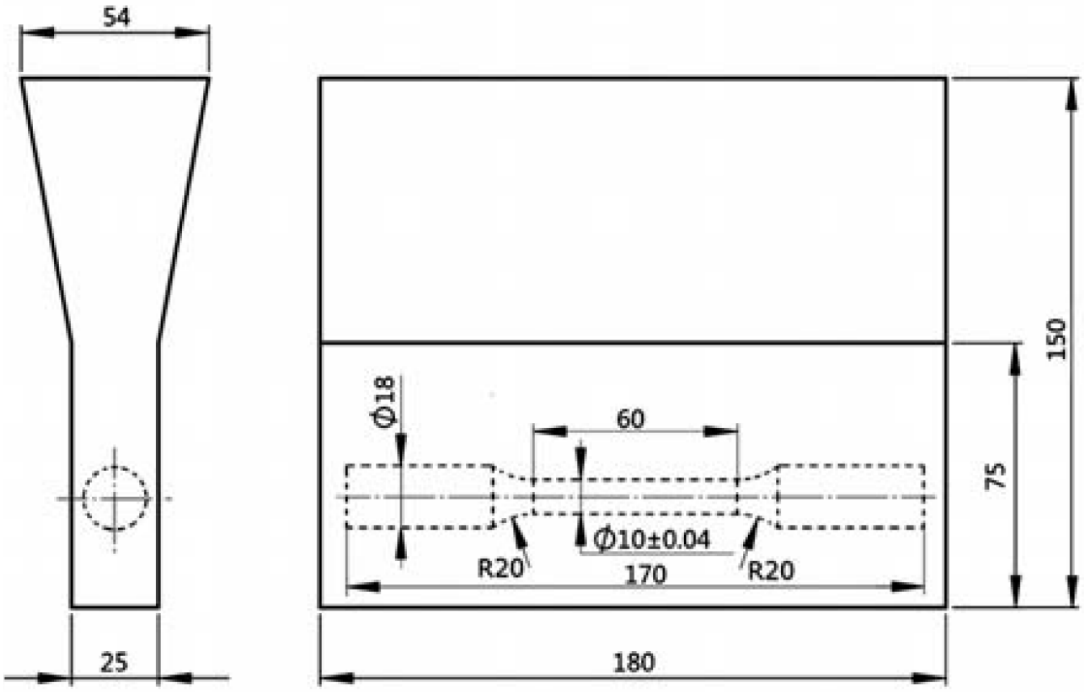

Figure 3.6. Schematic representation of a tensile test specimen (units: mm). [41]

3.6. Optical Emission Spectroscopy

From each heat, a coin sample was poured to a steel mold with copper die, ensuring unidirectional white (metastable) solidification, after the deslagging, together with the thermal analysis cups. 40 coin samples (1 for each heat, 20 for each alloy grade) for chemical analysis by using optical emission spectroscopy (OES) were collected. The coin samples were grinded and analyzed according to EN-ISO-1083 Standards by using an OBLF QSN 750-II OES.

3.7. Data Correlation

The data acquired from the mentioned methods of analysis (cooling curve thermal analysis, oxygen activity analysis, metallographic image analysis, optical emission spectroscopy analysis and tensile test) revealing the process variables and resulting

properties were stored in MS Office Excel sheets, and then imported to the linear regression software CSL™ developed by OCC GmbH. The linear regression software evaluates the existing correlations between process variables and resulting properties by analyzing the influence of one or more variables on a chosen parameter and lists the evaluated linear regressions by plotting calculated values versus measured values of the chosen parameter [42]. The software also calculates r-square, T-test and F-test values of each regression [42].

CHAPTER 4

RESULTS AND DISCUSSION

4.1. Chemical Analysis

Chemical analysis results from optical emission spectroscopy (OES) and active oxygen measurement results from Celox Foundry^{TM} were revealed in Table 4.1.

Table 4.1. *Chemical analysis results obtained by OES and Celox Foundry^{TM} conducted after the Mg treatment.*

Alloy	**Charge**	**Ladle**	**C**	**Si**	**S**	**Mn**	**Cu**	**Sn**	**Mg**	**aO**
EN-GJS	*#*	*#*	*%*	*%*	*%*	*%*	*%*	*%*	*%*	*ppb*
400-18	1	1	3.44	2.58	0.007	0.16	0.014	0.003	0.043	63
400-18	2	2	3.45	2.54	0.007	0.20	0.037	0.003	0.046	64
400-18	2	3	3.36	2.54	0.006	0.18	0.031	0.003	0.049	64
400-18	3	4	3.49	2.60	0.006	0.21	0.025	0.003	0.052	66
400-18	4	5	3.45	2.53	0.006	0.14	0.019	0.003	0.044	64
400-18	4	6	3.41	2.46	0.005	0.13	0.014	0.003	0.051	62
400-18	5	7	3.44	2.57	0.005	0.16	0.021	0.003	0.049	63
400-18	5	8	3.43	2.50	0.005	0.19	0.021	0.003	0.050	65
400-18	6	9	3.45	2.48	0.006	0.18	0.038	0.003	0.046	60
400-18	6	10	3.47	2.53	0.006	0.16	0.034	0.003	0.052	63
400-18	7	11	3.48	2.46	0.006	0.19	0.015	0.003	0.050	61
400-18	7	12	3.47	2.52	0.007	0.16	0.013	0.003	0.040	62
400-18	8	13	3.47	2.44	0.006	0.21	0.056	0.003	0.046	62
400-18	8	14	3.48	2.48	0.007	0.21	0.057	0.003	0.044	61
400-18	9	15	3.47	2.46	0.006	0.17	0.007	0.003	0.048	62
400-18	9	16	3.48	2.51	0.007	0.16	0.007	0.003	0.043	76
400-18	10	17	3.47	2.36	0.007	0.17	0.009	0.002	0.045	59
400-18	10	18	3.37	2.47	0.006	0.17	0.009	0.003	0.046	61
400-18	11	19	3.46	2.43	0.007	0.15	0.035	0.004	0.049	62
400-18	11	20	3.47	2.39	0.007	0.14	0.028	0.004	0.048	59

600-10C	12	21	2.90	4.20	0.007	0.16	0.010	0.005	0.050	65
600-10C	13	22	2.84	4.09	0.005	0.17	0.016	0.005	0.049	68
600-10C	13	23	2.83	4.20	0.006	0.17	0.015	0.005	0.047	61
600-10C	14	24	2.84	4.15	0.006	0.19	0.013	0.005	0.049	66
600-10C	15	25	2.85	4.08	0.005	0.15	0.018	0.005	0.054	61
600-10C	15	26	2.83	4.11	0.005	0.16	0.019	0.005	0.051	62
600-10C	16	27	2.85	4.19	0.006	0.18	0.026	0.005	0.050	63
600-10C	17	28	2.82	4.17	0.005	0.17	0.013	0.005	0.051	63
600-10C	17	29	2.88	4.11	0.006	0.16	0.015	0.005	0.046	65
600-10C	18	30	2.92	4.10	0.006	0.23	0.018	0.005	0.055	63
600-10C	19	31	2.77	4.13	0.006	0.17	0.009	0.005	0.044	67
600-10C	19	32	2.80	4.18	0.006	0.17	0.009	0.005	0.045	64
600-10C	20	33	2.95	4.10	0.006	0.17	0.035	0.006	0.052	66
600-10C	20	34	2.88	4.11	0.005	0.17	0.034	0.006	0.049	60
600-10C	21	35	2.76	4.01	0.005	0.16	0.058	0.006	0.040	74
600-10C	21	36	2.91	4.06	0.006	0.17	0.057	0.006	0.048	66
600-10C	22	37	2.92	4.06	0.006	0.21	0.033	0.006	0.056	59
600-10C	22	38	2.91	4.12	0.007	0.21	0.033	0.006	0.052	62
600-10C	23	39	2.95	4.12	0.006	0.20	0.031	0.006	0.050	69
600-10C	23	40	2.92	4.10	0.006	0.20	0.031	0.006	0.049	65

Carbon is the main alloying element for the regular cast iron grades. It forms the graphite phase which is characteristic for grey cast iron; and together with iron, it forms cementite (Fe_3C) which is characteristic for white cast iron, also a component of pearlite eutectoid phase mixture which is common for most of the cast iron and steel grades. For nodular cast iron grades, insufficient carbon content yields in a low amount of graphite phase which may result in high solidification shrinkage and high feeding needs because graphite formation provides a volume expansion during cast iron solidification. It may also yield in a low ductility of the resulting material because graphite phase in the structure provides elongation to ductile iron grades. Insufficient carbon content increases the tendency to have a metastable eutectic transformation forming carbides in the structure which result in a lower ductility and machinability. On the other hand, excessive carbon content results in a hyper-eutectic composition favoring some degenerated graphite forms and graphite floatation which have negative

effects on the resulting mechanical properties. Hyper-eutectic solidification provides a higher amount of graphite formation and volume expansion, but most of the graphite is formed before the eutectic transformation, and solid barrier formation on top of the risers, so most of the volume expansion is useless in terms of feeding needs. For the alloy EN-GJS-400-18, carbon is the main alloying element, and the target range for carbon content of this alloy that was set by the foundry is from 3.35% to 3.50%. As can be seen in Table 4.1, all the EN-GJS-400-18 specimens have carbon contents within the target range. Since the alloy EN-GJS-600-10C has silicon as the main alloying element, and it contributes to the carbon equivalent (C.E.), target range for carbon content of this alloy that was set by the foundry is from 2.80% to 2.95% in order to have a hypo-eutectic solidification. As can be seen in Table 4.1, the specimens from ladle 31 and 35 have carbon contents below the lower limit of the target range. In microstructural image analysis results (see Table 4.4), it can be seen that the specimens from ladle 31 and 35 have the lowest graphite phase area percentage among all the specimens which can be explained by the insufficient carbon content.

Silicon is a crucial alloying element for all grey cast iron grades. It increases the stable eutectic transformation temperature and decreases the metastable one so that those two transformation temperatures get farther from each other, and the possibility to have a stable eutectic solidification increases. Therefore, it is known as a graphite former. Since they both are necessary for graphite formation, silicon's being insufficient or excessive yields in similar tendencies as carbon's does. For solution strengthened ferritic ductile iron (SSFDI) grades, silicon content is even higher than carbon content because there, silicon has another function in addition to being graphite former. Silicon atoms act as solute atoms in ferrite structure resulting in lattice strains which impedes the dislocation movement, thus provide solution strengthening. Unlike ferritic-pearlitic matrix, solution strengthened ferritic matrix does not decrease the ductility dramatically while increasing the strength. Also, with solution strengthened ferritic matrix, strengthening is much more consistent among the sections with different level of cooling rate than it is with ferritic-pearlitic matrix. Therefore, for

SSFDI grades, in the case of insufficient silicon content, less strain to be formed in ferritic matrix structure may result in a lower strength. On the other hand, in the literature, there are some studies claiming that both strength and ductility of SSFDI grades make a peak at around 4.3%Si, then they drop dramatically due to the formation of some brittle forms and the graphite degeneration [43, 44]. For the alloy EN-GJS-400-18, the target range for silicon content that was set by the foundry is from 2.30% to 2.60%. For EN-GJS-600-10C which is an SSFDI grade, it is from 4.00% to 4.30%. As can be seen in Table 4.1, all the specimens from both alloys have silicon contents within the target ranges.

Sulphur and oxygen are the surface-active elements reducing the interface energy between iron and graphite. Therefore, decreasing their content in elemental form makes increasing the volume/surface-area ratio of the graphite particles thermodynamically more feasible, so it makes spherical graphite shape more stable. Therefore, excess amount of sulphur and oxygen may decrease the nodularity and affect the resulting mechanical properties negatively. On the other hand, according to T. Skaland et al., heterogeneous nucleation sites for graphite nucleation are complex, multi-layer sulphide-oxide inclusions [23]. Therefore, insufficient amount of sulphur and oxygen may limit the number of heterogeneous nucleation sites to be formed, thus the resulting graphite nodule count, and affect the mechanical properties negatively. For both alloys, the target range for sulphur content that was set by the foundry is from 0.005% to 0.008%. As can be seen in Table 4.1, all the specimens from both alloys have sulphur contents within the target range. For the active oxygen amount, the target range is from 60 ppb to 70 ppb. As can be seen in Table 4.1, the specimens from ladles 17, 20 and 37 have active oxygen contents below the lower limit where the ones from ladles 16 and 35 are above the upper limit. Since there are many parameters which may affect the nodularity and the nodule count, it is difficult to see the effect of slightly lower or higher active oxygen content on the resulting microstructure.

Magnesium is introduced to the base iron of the nodular cast iron melts by a process named as magnesium treatment, and its objective is to nodularize the graphite particle

shape by decreasing the content of surface active elements (sulphur and oxygen) and increasing the interface energy between iron and graphite, so its effect is basically reverse of the effect of sulphur and oxygen. Insufficient magnesium content decreases the stability of spherical shape of the graphite and decreases the nodularity which may affect the resulting mechanical properties negatively. On the other hand, excessive magnesium content lowers the contents of sulphur and oxygen excessively, and it may limit the nodule count in the resulting structure, thus the mechanical properties. Since magnesium is a carbide former, its excess content may also induce the carbide formation which has a negative effect on the ductility and machinability. For both alloys, the target range for magnesium content that was set by the foundry is from 0.040% to 0.055%. As can be seen in Table 4.1, only the specimen from ladle 37 has a magnesium content above the upper limit, and the rest are in the range. Since it is just above the limit, it is difficult see its effect on the resulting properties.

Manganese is an important alloying element for lamellar graphite cast iron because it prevents the formation of FeS which segregates at the grain boundaries, and it forms MnS which is distributed homogeneously. To produce nodular cast iron, the melt is treated by magnesium which bonds the sulphur, so there is no need for manganese. In addition, manganese favors the pearlite formation, also excessive content of manganese may result in metastable eutectic transformation. Since both alloys are fully ferritic, the maximum manganese content for both alloys that was set by the foundry is 0.25%. As can be seen in Table 4.1, all the specimens from both alloys have manganese contents below the limit.

Copper and tin are also pearlite stabilizers, so they decrease the resulting ductility while increasing the strength. Tin is a stronger pearlite stabilizer than that copper is, so that much less amount of tin enough to achieve the same pearlite content achieved by much more copper content. Since both alloys are fully ferritic, the maximum copper and tin contents for both alloys that were set by the foundry are 0.06% and 0.006% respectively. As can be seen in Table 4.1, all the specimens from both alloys have copper and tin contents within the target range.

Active oxygen amount versus alloy grade chart is revealed in Figure 4.1 as box chart. In the lamellar grey iron or the base iron of the nodular cast iron, amount of active oxygen is mainly determined by silicon because it has the highest oxygen affinity at a typical temperature of cast iron melt preparation. And, both alloy types were treated by the same ratio of Mg master alloy. Therefore, one could expect the high silicon alloy grade to have a lower content of active oxygen, but by looking at Figure 4.1, it can be said that this is not the case. The reason may be that an active oxygen content of 60 to 70 ppb is already too low so that the effect of having less oxygen before the treatment is not visible on these resulting values.

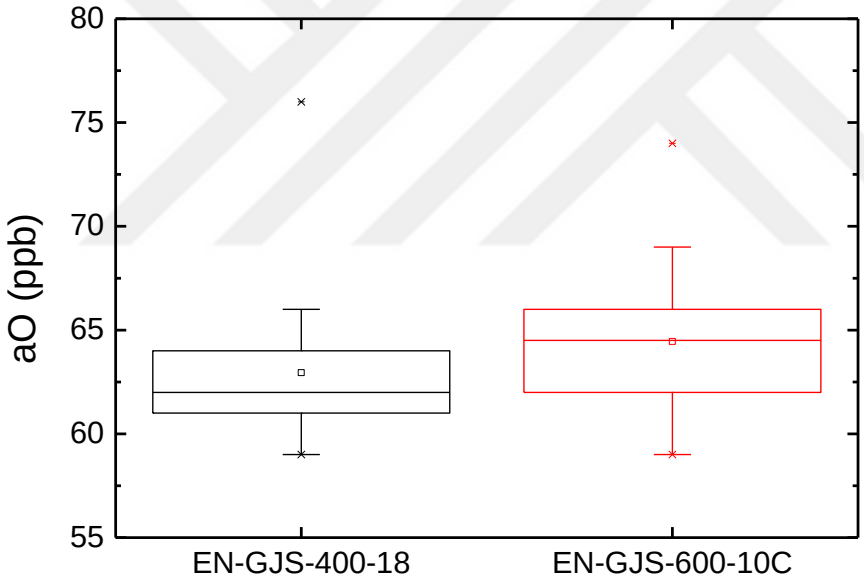

Figure 4.1. Active oxygen amount (aO) versus alloy grade.

4.2. Tensile Test

Tensile test results of the Y2-blocks poured separately and machined into standard test specimens are revealed in Table 4.2.

Table 4.2. *Tensile test results of the specimens obtained from each ladle.*

Alloy	**Charge**	**Ladle**	**UTS**	**R 0.2%**	**Elongation**
EN-GJS	*#*	*#*	*MPa*	*MPa*	*%*
400-18	1	1	435.7	299.9	22.2
400-18	2	2	436.9	296.6	22.1
400-18	2	3	440.8	302.8	24.4
400-18	3	4	421.9	296.1	25.7
400-18	4	5	436.5	302.6	21.5
400-18	4	6	429.2	291.5	23.1
400-18	5	7	429.5	291.9	22.9
400-18	5	8	412.9	284.9	22.1
400-18	6	9	411.4	282.7	24.5
400-18	6	10	432.6	295.9	19.8
400-18	7	11	400.1	284.6	23.3
400-18	7	12	463.1	307.1	18.4
400-18	8	13	410.1	287.0	23.8
400-18	8	14	419.6	297.4	23.8
400-18	9	15	396.2	272.6	23.3
400-18	9	16	427.8	299.9	23.1
400-18	10	17	458.7	309.2	15.7
400-18	10	18	452.5	307.3	17.5
400-18	11	19	404.0	281.3	23.1
400-18	11	20	468.7	313.4	18.2
600-10C	12	21	636.0	529.0	16.4
600-10C	13	22	601.1	497.5	16.5
600-10C	13	23	613.7	509.2	19.3
600-10C	14	24	600.6	500.1	14.4
600-10C	15	25	607.7	497.9	15.7
600-10C	15	26	610.6	507.5	19.8
600-10C	16	27	598.9	500.1	13.2
600-10C	17	28	618.0	510.0	17.1

600-10C	17	29	632.0	528.0	16.8
600-10C	18	30	605.0	501.0	18.0
600-10C	19	31	600.8	499.7	14.5
600-10C	19	32	610.0	515.0	13.2
600-10C	20	33	620.3	519.1	15.3
600-10C	20	34	621.1	519.7	15.1
600-10C	21	35	598.1	497.6	13.8
600-10C	21	36	610.0	507.9	17.3
600-10C	22	37	603.1	500.5	18.9
600-10C	22	38	600.9	501.8	18.6
600-10C	23	39	599.0	501.4	14.2
600-10C	23	40	600.2	501.9	14.1

Since design of the structures is done by considering the mechanical properties of the materials to be used, tensile test results are significant in defining the material performance, and they take place in the technical specifications of almost all engineering materials. As indicated by their names in the standards, for the grade EN-GJS-400-18, minimum ultimate tensile strength requirement is 400 MPa, and minimum total elongation requirement is 18%, where for the grade EN-GJS-600-10C, these values are 600 MPa and 10%. Alloy EN-GJS-400-18 is widely used in applications where high material elongation is required even at low ambient temperatures, and a mild strength is enough which is getting popular in wind energy industry. On the other hand, alloy EN-GJS-600-10C provides a high strength without a dramatic loss in ductility as a result of its solution strengthened ferritic matrix instead of pearlitic-ferritic matrix, and it is getting popular in heavy-duty machine industry to replace some of plain-carbon-steel grades. As can be seen in Table 4.2, the specimens from the ladles 15, 27, 35 and 39 have ultimate tensile strength values slightly below the minimum requirement, and the ones from the ladles 17 and 18 have total elongation values below the minimum requirement. Since the process defines the microstructure and the microstructure defines the performance, it could be expected to find explanations for the out of specification specimens by means of microstructural properties, thus the process parameters, but there could not be found, and this can be

explained by that the Y2-blocks samples for the tensile test were poured separately, and they had different cooling conditions, where the metallographic specimens were obtained from thermal analysis cup samples in order to observe the microstructures corresponding the cooling curves.

4.3. Cooling Curve Thermal Analysis

The main results obtained from the cooling curves by using thermal analysis cups with various contents are listed in Table 4.3.

Table 4.3. *The main results of cooling curve thermal analysis indicating contents of the analysis cups (Content types; 1-Spherix™ inoculant, 2-Sperix-Plus™ inoculant, 3-SMW605™ inoculant, 4-Te and S).*

Ladle	**Cup**	**Content**		**TL**	**TEmin**	**TE**	**TE/dt**	**TEmax**	**TF**	**TF/dt**
#	*#*	*Type*	*%*	*°C*	*°C*	*°C*	*°C/s*	*°C*	*°C*	*°C/s*
1	1	1	0.05	1166.4	1148.4	1149.4	0.6	1152.3	1100.0	-5.4
1	2	2	0.05	1167.6	1146.3	1148.6	0.7	1152.0	1088.2	-4.8
1	3	3	0.05	1166.1	1147.8	1149.1	0.4	1151.2	1122.3	-4.7
1	4	-	-	1166.2	1134.7	1138.4	0.9	1145.2	1085.8	-4.4
2	5	1	0.05	1166.5	1148.0	1149.1	0.5	1151.7	1098.0	-4.8
2	6	2	0.05	1167.4	1145.6	1148.0	0.8	1152.0	1089.4	-5.1
2	7	3	0.05	1166.8	1147.6	1148.4	0.4	1151.1	1093.7	-5.2
2	8	-	-	1164.3	1133.8	1138.3	1.1	1144.6	1085.4	-5.0
3	9	1	0.05	1169.5	1147.1	1148.9	0.6	1151.9	1099.5	-4.5
3	10	2	0.05	1170.0	1145.8	1148.0	0.7	1152.5	1092.7	-4.7
3	11	3	0.05	1169.5	1147.0	1148.7	0.6	1152.3	1100.8	-5.0
3	12	-	-	1168.3	1131.5	1136.5	1.1	1143.5	1086.2	-4.4
4	13	1	0.05	1158.4	1147.2	1148.5	0.6	1151.7	1112.8	-4.6
4	14	2	0.05	1158.8	1146.5	1148.3	0.7	1152.0	1087.4	-4.7
4	15	3	0.05	1158.7	1147.4	1148.7	0.5	1151.1	1119.5	-4.3
4	16	-	-	1157.2	1122.2	1127.5	1.5	1136.3	1106.8	-3.2
5	17	1	0.05	1166.5	1148.6	1149.8	0.4	1152.0	1097.1	-4.9
5	18	2	0.05	1166.3	1146.7	1148.7	0.6	1151.4	1089.8	-5.4
5	19	3	0.05	1166.5	1149.2	1150.1	0.4	1152.1	1098.6	-4.9

5	20	-	-	1166.3	1134.5	1138.3	1.0	1144.0	1081.6	-4.9
6	21	1	0.05	1171.3	1147.2	1148.2	0.5	1150.9	1092.0	-5.4
6	22	2	0.05	1173.8	1145.7	1148.3	0.7	1151.9	1089.3	-5.3
6	23	3	0.05	1172.2	1147.6	1149.3	0.6	1151.9	1095.7	-6.1
6	24	-	-	1172.8	1130.1	1135.8	1.3	1141.9	1089.1	-6.0
7	25	1	0.05	1161.5	1146.2	1147.8	0.6	1150.4	1089.9	-5.5
7	26	2	0.05	1162.4	1143.3	1145.7	0.8	1149.5	1085.4	-5.5
7	27	3	0.05	1161.3	1147.2	1148.3	0.6	1150.9	1097.9	-5.8
7	28	-	-	1161.2	1132.4	1137.3	1.2	1144.0	1088.7	-5.3
8	29	1	0.05	1164.8	1143.6	1145.8	0.8	1149.2	1090.1	-6.2
8	30	2	0.05	1163.9	1140.2	1143.8	0.9	1148.7	1086.9	-5.1
8	31	3	0.05	1163.0	1147.1	1148.2	0.5	1151.0	1095.7	-5.8
8	32	-	-	1161.7	1124.1	1129.4	1.4	1137.7	1080.8	-5.3
9	33	1	0.05	1168.0	1146.7	1148.8	0.7	1152.2	1099.7	-4.8
9	34	2	0.05	1166.8	1142.3	1145.1	0.9	1149.6	1087.8	-4.9
9	35	3	0.05	1167.8	1145.8	1147.5	0.7	1151.6	1093.9	-5.6
9	36	-	-	1167.9	1126.4	1132.4	1.4	1140.7	1087.2	-5.3
10	37	1	0.05	1162.0	1147.8	1149.9	0.6	1152.2	1089.8	-4.5
10	38	2	0.05	1164.7	1148.5	1150.1	0.7	1154.3	1097.3	-4.6
10	39	3	0.05	1162.5	1148.1	1149.8	0.4	1151.6	1119.7	-4.9
10	40	-	-	1163.2	1129.4	1134.1	1.3	1143.1	1086.9	-4.3
11	41	-	-	1159.1	1129.7	1133.8	1.1	1140.2	1076.9	-4.7
11	42	1	0.05	1161.5	1142.7	1144.3	0.6	1147.5	1088.1	-5.3
11	43	1	0.10	1161.0	1144.9	1145.8	0.4	1148.4	1089.9	-5.5
11	44	1	0.15	1161.2	1145.3	1146.7	0.6	1149.9	1088.7	-5.6
11	W1	4	0.70	1161.9	-	1108.4	-	-	-	-
12	45	-	-	1156.7	1132.9	1136.7	0.9	1142.6	1076.6	-4.2
12	46	1	0.05	1158.7	1148.1	1148.9	0.4	1151.4	1115.5	-4.9
12	47	1	0.10	1159.1	1148.8	1149.8	0.4	1151.9	1119.2	-5.0
12	48	1	0.15	1158.6	1147.9	1149.1	0.5	1151.4	1119.8	-5.0
12	W2	4	0.70	1158.9	-	1107.1	-	-	-	-
13	49	-	-	1161.9	1125.9	1129.4	1.0	1136.2	1097.1	-4.0
13	50	1	0.05	1163.5	1145.2	1147.3	0.7	1150.7	1103.1	-5.0
13	51	1	0.10	1162.6	1147.0	1148.5	0.5	1151.0	1095.4	-5.0
13	52	1	0.15	1161.6	1146.6	1147.7	0.5	1150.6	1092.0	-4.9
13	W3	4	0.70	1159.5	-	1108.4	-	-	-	-
14	53	-	-	1158.2	1125.1	1129.8	1.0	1136.0	1095.0	-3.9
14	54	1	0.05	1160.8	1146.2	1148.0	0.5	1150.9	1115.6	-4.5
14	55	1	0.10	1161.1	1149.5	1150.3	0.4	1152.0	1121.4	-4.6

14	56	1	0.15	1160.6	1145.6	1147.0	0.6	1150.2	1090.0	-5.0
14	W4	4	0.70	1156.9	-	1108.6	-	-	-	-
15	57	-	-	1156.1	1133.6	1137.6	1.0	1143.2	1082.4	-4.8
15	58	1	0.05	1158.9	1147.7	1148.4	0.4	1151.0	1090.6	-5.4
15	59	1	0.10	1158.9	1147.3	1148.4	0.4	1150.3	1089.2	-5.5
15	60	1	0.15	1158.8	1147.7	1148.7	0.4	1150.5	1096.7	-6.2
15	W5	4	0.70	1159.4	-	1108.5	-	-	-	-
16	61	-	-	1154.3	1133.3	1137.3	1.0	1142.9	1083.7	-4.5
16	62	1	0.05	1157.4	1148.3	1149.1	0.5	1150.4	1088.7	-5.1
16	63	1	0.10	1157.2	1149.2	1150.4	0.4	1152.3	1118.7	-4.9
16	64	1	0.15	1156.4	1149.2	1149.6	0.3	1150.5	1117.6	-5.3
16	W6	4	0.70	1152.1	-	1107.2	-	-	-	-
17	65	-	-	1166.3	1133.9	1138.3	0.9	1142.6	1082.6	-4.8
17	66	1	0.05	1166.8	1144.7	1146.2	0.6	1149.1	1090.0	-5.1
17	67	1	0.10	1166.4	1148.0	1149.0	0.4	1150.7	1090.0	-5.3
17	68	1	0.15	1167.4	1148.6	1149.4	0.4	1151.4	1115.7	-5.3
17	W7	4	0.70	1166.2	-	1109.0	-	-	-	-
18	69	-	-	1166.2	1132.6	1136.7	1.0	1142.1	1084.5	-4.6
18	70	1	0.05	1170.4	1148.3	1149.3	0.4	1151.6	1115.8	-5.1
18	71	1	0.10	1169.0	1149.1	1150.5	0.4	1151.9	1100.6	-5.2
18	72	1	0.15	1168.2	1148.9	1149.6	0.4	1151.5	1116.7	-5.5
18	W8	4	0.70	1163.6	-	1106.6	-	-	-	-
19	73	-	-	1165.7	1130.1	1134.2	1.0	1140.2	1073.1	-4.6
19	74	1	0.05	1164.4	1145.4	1146.8	0.6	1149.6	1088.5	-5.3
19	75	1	0.10	1166.3	1145.6	1147.0	0.6	1149.6	1090.2	-5.5
19	76	1	0.15	1166.9	1147.8	1149.1	0.5	1151.2	1091.2	-5.9
19	W9	4	0.70	1166.9	-	1109.0	-	-	-	-
20	77	-	-	1160.2	1129.9	1135.2	1.0	1140.4	1075.2	-4.2
20	78	1	0.05	1164.7	1145.9	1147.4	0.6	1150.6	1088.5	-5.0
20	79	1	0.10	1163.8	1147.1	1148.0	0.4	1150.3	1115.0	-4.9
20	80	1	0.15	1162.5	1146.0	1147.5	0.5	1149.7	1090.4	-5.3
20	W10	4	0.70	1157.5	-	1108.4	-	-	-	-
21	81	1	0.05	1180.4	1151.7	1153.2	0.5	1155.3	1102.0	-5.8
21	82	2	0.05	1181.5	1147.8	1150.1	0.7	1152.9	1089.5	-5.2
21	83	3	0.05	1179.3	1150.8	1152.9	0.5	1155.0	1103.6	-6.2
21	84	-	-	1179.2	1133.7	1138.4	1.0	1144.1	1085.8	-4.7
22	85	1	0.05	1185.6	1150.2	1152.4	0.6	1154.3	1098.0	-6.7
22	86	2	0.05	1187.3	1148.8	1150.7	0.7	1153.9	1092.5	-6.1
22	87	3	0.05	1186.3	1151.7	1153.8	0.6	1155.7	1108.2	-7.5

22	88	-	-	1185.8	1138.6	1142.0	0.9	1147.0	1090.3	-5.1
23	89	1	0.05	1180.8	1149.3	1151.5	0.7	1154.0	1098.0	-6.2
23	90	2	0.05	1181.8	1146.5	1148.9	0.8	1152.8	1095.7	-5.8
23	91	3	0.05	1181.9	1147.3	1149.5	0.8	1152.6	1097.4	-7.1
23	92	-	-	1180.7	1135.2	1139.3	1.3	1146.0	1087.7	-5.4
24	93	1	0.05	1183.5	1148.5	1151.0	0.7	1154.4	1101.6	-5.2
24	94	2	0.05	1184.4	1146.8	1148.8	0.7	1152.4	1090.2	-5.2
24	95	3	0.05	1184.0	1150.6	1152.3	0.5	1154.3	1098.7	-5.8
24	96	-	-	1183.4	1131.4	1136.7	1.3	1144.4	1090.4	-4.9
25	97	1	0.05	1185.0	1150.1	1151.7	0.7	1154.9	1105.5	-6.1
25	98	2	0.05	1186.0	1145.4	1147.6	0.7	1150.6	1086.9	-5.6
25	99	3	0.05	1185.8	1149.0	1151.2	0.7	1154.0	1102.5	-6.1
25	100	-	-	1184.6	1130.3	1135.2	1.4	1141.9	1086.3	-5.7
26	101	1	0.05	1186.7	1150.2	1151.9	0.6	1154.4	1096.8	-5.5
26	102	2	0.05	1187.1	1144.2	1146.6	0.7	1150.2	1087.8	-5.1
26	103	3	0.05	1186.9	1149.3	1151.3	0.7	1154.4	1099.6	-5.4
26	104	-	-	1184.8	1125.9	1132.0	1.4	1138.7	1078.8	-5.0
27	105	1	0.05	1183.9	1144.8	1147.5	0.9	1151.0	1090.9	-6.1
27	106	2	0.05	1184.9	1142.2	1144.9	0.9	1149.0	1086.1	-5.8
27	107	3	0.05	1184.0	1149.7	1152.3	0.7	1154.4	1101.7	-6.2
27	108	-	-	1183.1	1129.7	1135.6	1.4	1142.6	1087.2	-5.1
28	109	1	0.05	1184.2	1148.6	1150.7	0.7	1153.9	1096.2	-5.2
28	110	2	0.05	1185.1	1145.5	1146.9	0.6	1149.5	1083.0	-5.1
28	111	3	0.05	1184.7	1146.6	1149.4	0.9	1153.3	1102.1	-6.1
28	112	-	-	1183.7	1129.3	1134.2	1.5	1141.8	1084.2	-5.4
29	113	1	0.05	1175.4	1150.2	1152.0	0.5	1154.1	1104.0	-6.0
29	114	2	0.05	1176.0	1146.7	1149.3	0.8	1153.0	1099.5	-5.6
29	115	3	0.05	1174.3	1147.8	1150.0	0.8	1153.4	1093.0	-6.3
29	116	-	-	1174.2	1133.1	1138.7	1.5	1145.9	1092.9	-6.0
30	117	1	0.05	1176.7	1150.5	1152.0	0.5	1154.3	1092.6	-5.6
30	118	2	0.05	1176.9	1141.9	1144.0	0.7	1147.4	1080.8	-5.0
30	119	3	0.05	1176.0	1149.6	1151.6	0.7	1154.2	1093.5	-5.3
30	120	-	-	1176.0	1125.9	1133.1	1.5	1140.5	1083.8	-4.8
31	121	-	-	1181.3	1133.5	1137.8	1.1	1142.9	1084.0	-5.1
31	122	1	0.05	1183.3	1149.3	1150.9	0.6	1153.2	1089.8	-5.4
31	123	1	0.10	1184.1	1144.8	1147.0	0.6	1149.2	1087.8	-5.2
31	124	1	0.15	1183.0	1150.1	1151.7	0.5	1153.7	1092.8	-5.7
31	W11	4	0.70	1183.8	-	1074.3	-	-	-	-
32	125	-	-	1179.9	1134.8	1138.5	1.0	1143.5	1084.4	-5.1

32	126	1	0.05	1180.7	1142.2	1144.8	0.7	1147.7	1085.3	-5.2
32	127	1	0.10	1182.4	1147.7	1150.0	0.6	1152.3	1088.9	-5.6
32	128	1	0.15	1181.3	1149.5	1151.2	0.6	1153.8	1098.3	-6.0
32	W12	4	0.70	1184.7	-	1073.1	-	-	-	-
33	129	-	-	1167.0	1132.3	1137.0	1.2	1143.2	1073.2	-5.0
33	130	1	0.05	1169.4	1142.5	1145.1	0.8	1149.0	1084.8	-5.4
33	131	1	0.10	1169.1	1144.4	1146.8	0.8	1150.3	1085.2	-5.7
33	132	1	0.15	1168.8	1145.0	1147.2	0.7	1149.9	1086.4	-5.8
33	W13	4	0.70	1169.4	-	1075.2	-	-	-	-
34	133	-	-	1174.6	1133.7	1137.9	1.2	1144.8	1086.1	-4.9
34	134	1	0.05	1177.6	1142.6	1145.3	0.8	1149.2	1086.1	-5.3
34	135	1	0.10	1176.9	1143.3	1146.2	0.8	1149.6	1086.3	-5.6
34	136	1	0.15	1176.1	1149.6	1150.5	0.4	1152.3	1089.7	-5.3
34	W14	4	0.70	1177.1	-	1075.4	-	-	-	-
35	137	-	-	1174.3	1135.7	1140.1	1.2	1146.2	1088.8	-5.6
35	138	1	0.05	1176.4	1147.2	1149.4	0.8	1152.7	1089.8	-6.0
35	139	1	0.10	1175.1	1144.8	1147.1	0.8	1151.1	1089.9	-6.2
35	140	1	0.15	1175.1	1146.7	1148.5	0.8	1151.7	1091.0	-6.6
35	W15	4	0.70	1176.6	-	1075.9	-	-	-	-
36	141	-	-	1173.8	1137.8	1142.1	1.1	1147.5	1086.8	-5.4
36	142	1	0.05	1175.2	1147.7	1150.3	0.8	1153.2	1087.8	-6.0
36	143	1	0.10	1173.5	1144.1	1146.7	0.8	1150.3	-	-
36	144	1	0.15	1174.1	1143.2	1146.8	1.0	1150.2	1090.6	-6.5
36	W16	4	0.70	1175.9	-	1075.9	-	-	-	-
37	145	-	-	1175.2	1131.6	1136.4	1.2	1142.1	1082.2	-4.9
37	146	1	0.05	1176.8	1147.0	1149.1	0.7	1152.1	1087.7	-5.3
37	147	1	0.10	1175.7	1144.6	1147.0	0.7	1150.2	1087.0	-5.6
37	148	1	0.15	1175.4	1147.2	1149.3	0.6	1151.6	1088.1	-6.3
37	W17	4	0.70	1177.5	-	1077.0	-	-	-	-
38	149	-	-	1172.0	1130.1	1135.4	1.4	1142.5	1085.9	-5.0
38	150	1	0.05	1172.9	1143.6	1146.3	0.9	1150.1	1085.7	-5.7
38	151	1	0.10	1171.5	1145.4	1147.3	0.7	1150.5	1085.1	-5.8
38	152	1	0.15	1171.0	1145.9	1148.2	0.8	1151.7	1091.3	-6.1
38	W18	4	0.70	1174.6	-	1076.3	-	-	-	-
39	153	-	-	1167.0	1128.5	1133.7	1.4	1141.4	1077.4	-5.2
39	154	1	0.05	1169.2	1145.0	1147.4	0.8	1150.8	1086.7	-6.2
39	155	1	0.10	1167.5	1142.9	1145.8	1.0	1150.4	-	-
39	156	1	0.15	1168.2	1143.3	1145.4	0.8	1149.4	1087.6	-6.3
39	W19	4	0.70	1173.0	-	1076.3	-	-	-	-

40	157	-	-	1173.9	1128.1	1137.7	1.2	1143.8	1083.2	-5.1
40	158	1	0.05	1175.7	1147.4	1147.6	0.8	1150.9	1087.1	-5.6
40	159	1	0.10	1175.1	1148.4	1147.1	0.8	1150.4	1087.2	-5.7
40	160	1	0.15	1174.8	1148.6	1148.8	0.7	1151.6	1090.6	-6.1
40	W20	4	0.70	1176.9	-	1075.6	-	-	-	-

Liquidus temperature (TL) versus alloy grade chart is revealed in Figure 4.2 as box chart. In hypoeutectic part of Fe-C binary phase diagram, liquidus temperature is the temperature at which pro-eutectic austenite dendrites nucleate and start growing, and it is dependent on the carbon content or in this (cast iron) case carbon equivalent. As can be seen in Figure 4.2, in general, the specimens of EN-GJS-600-10C grade have a higher liquidus temperature than that the ones of EN-GJS-400-18 do. Average liquidus temperature difference among two alloys is 15.0^{o}C. When the average carbon equivalent difference among two alloys is calculated according to Equation 2.1, the specimens of EN-GJS-400-18 have 0.04% higher average carbon equivalent, and according to Equation 2.2, it is 0.17%. If we assume that slope of the hypoeutectic liquidus line is -91.6^{o}C / %C.E., 15.0^{o}C change in liquidus temperature requires 0.16% of change in carbon equivalent. Therefore, it is possible to say that Equation 2.2 gives a good estimation for the effect of silicon on the hypoeutectic liquidus line of Fe-C phase diagram.

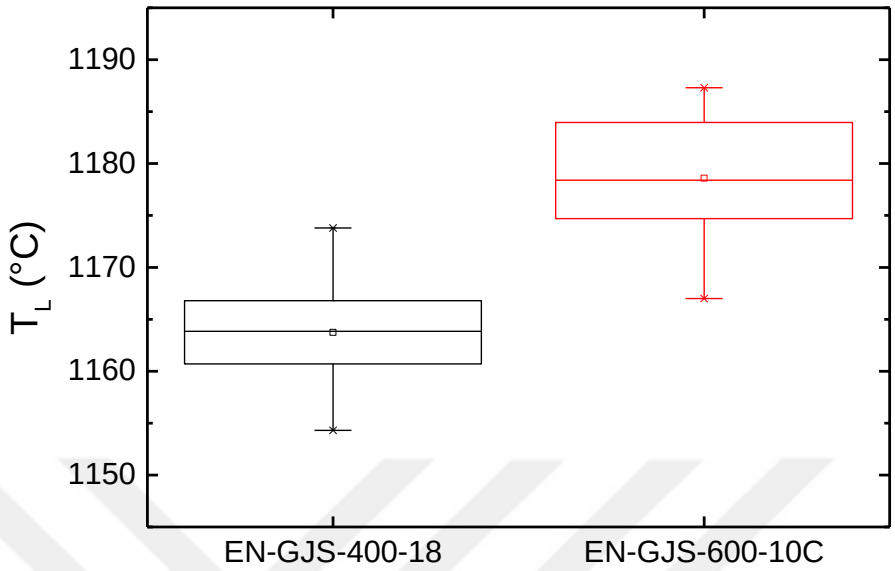

Figure 4.2. Liquidus temperature (TL) versus alloy grade.

Upper eutectic temperature (TEmax) versus alloy grade chart is revealed for plain and inoculated analysis cups separately in Figure 4.3 as box chart. Upper eutectic temperature is the point at which the recalescence ends up, and the cooling down starts back. Recalescence occurs due to heat evolved in a high rate as a result of high growth rate of the graphite particles, thus high rate of carbon dissociation. Therefore, it starts right after the nucleation of graphite particles which is represented by lower eutectic temperature (TEmin), and if there are enough heterogeneous nucleation sites for graphite, recalescence is limited by the stable eutectic transformation temperature because a high amount of (latent) heat needs be produced to go above that temperature or to melt back. If there are not enough heterogeneous nucleation sites for graphite, recalescence is limited by the density of the growing graphite particles in the matrix which defines the diffusion path. As can be seen in Figure 4.3, in general, for both alloy grades, the specimens from plain analysis cups have lower TEmax values, and

TEmax values of the specimens from inoculant containing cups mostly accumulated at top. This can be explained by that TEmax values of the specimens from plain cups are limited by the low density of graphite particles making the carbon diffusion path longer, and TEmax values of the ones from inoculant containing cups are limited by the stable eutectic transformation temperature which requires re-melting to go beyond. In Figure 4.3, it can also be seen that TEmax values of the EN-GJS-EN-400-18 specimens that are saturated in terms of heterogeneous nucleation sites are aligned at around 1152°C which is the stable eutectic transformation temperature. On the other hand, the ones of EN-GJS EN-GJS-600-10C are aligned at around 1154°C. This difference can be explained by the effect of silicon on the eutectic transformation temperatures such that it increases the stable eutectic transformation temperature while decreasing the metastable one. Since EN-GJS-600-10C grade has a higher silicon content, it is expected to have a higher stable eutectic transformation temperature. It is difficult to define the magnitude of the effect of silicon on the stable eutectic transformation temperature due to the variety of factors defining the diffusion kinetics for particle growth.

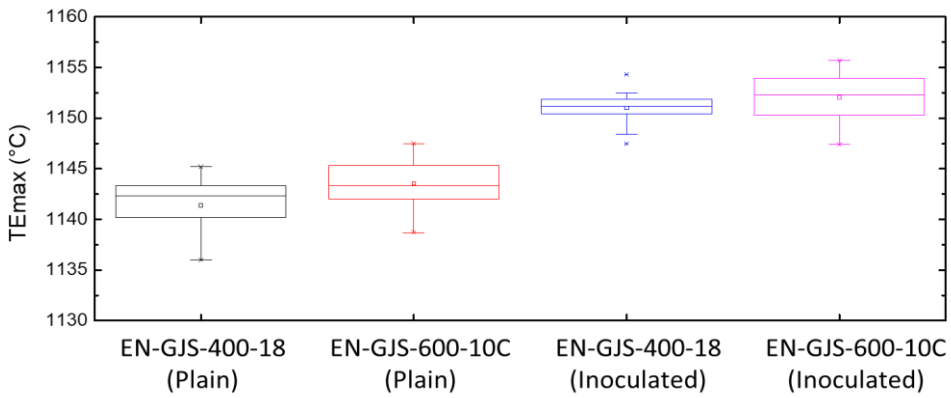

Figure 4.3. Upper eutectic temperature (TEmax) versus alloy grade for plain and inoculated analysis cups separately.

Time difference between the end of freezing (TF) and lower eutectic (TEmin) points of the cooling curve (TF_t – TEmin_t) versus alloy grade chart is revealed in Figure 4.4 as box chart. In cooling curve of hypoeutectic ductile iron; after the liquidus, temperature decreases until there is enough driving force for graphite particles to nucleate and grow, so eutectic transformation starts at the lower eutectic point, then the graphite growth rate is so high that the heat evolved is higher than the heat removed by the surroundings, and temperature increases until the upper eutectic point, then it starts cooling back but not as fast because the growth slowly continues until the end of freezing point where the cooling rate increases since the growth terminated, thus the eutectic transformation. Therefore, it is possible to say that growth of the graphite particles or the eutectic transformation starts around the lower eutectic point, and ends around the end of freezing point, so the time difference between these two points gives an idea on the total duration of graphite growth or eutectic transformation. As can be seen in Figure 4.4, in general, the specimens of EN-GJS-600-10C grade have a lower time difference between the end of freezing and the lower eutectic points than that the ones of EN-GJS-400-18 do. This can be explained by that the specimens of EN-GJS-600-10C grade have less amount of graphite in their microstructure (see Figure 4.7),

so graphite particle growth terminates earlier, and the amount of evolved heat is lower which results in a lower total duration of eutectic transformation.

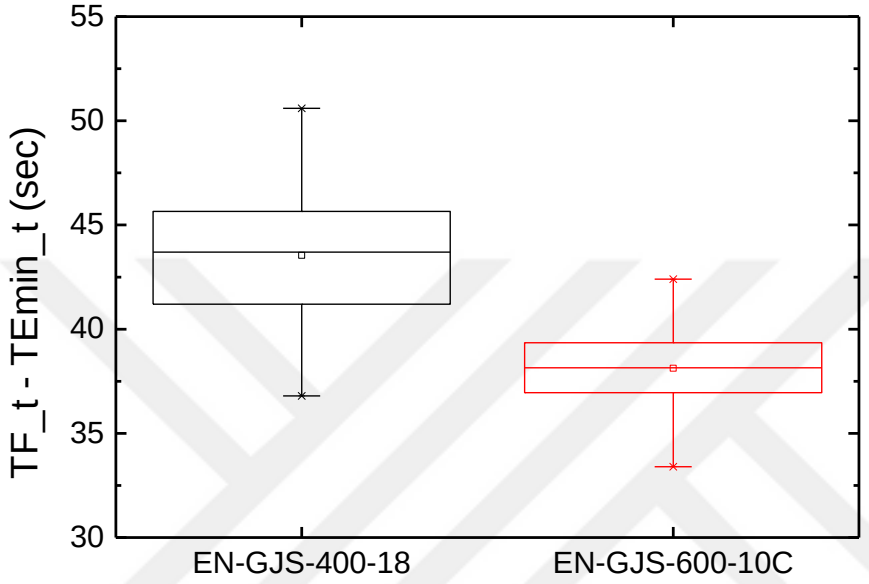

Figure 4.4. Time difference between the end of freezing and lower eutectic (TF_t – TEmin_t) versus alloy grade.

Liquidus temperature (TL) versus content of the analysis cup chart is revealed in Figure 4.5 as box chart. The difference in liquidus temperatures of two alloy grades was discussed before. For the hypoeutectic nodular cast iron melts, liquidus temperature represents the start of pro-eutectic austenite nucleation and growth, and it does not require a high energy as that graphite does, so there is no considerable amount of undercooling. By looking at Figure 4.5, it is be possible to say that the specimens from the cups with 0.05% of inoculant have liquidus temperatures in a similar level which may be slightly higher than the ones from the plain cups, and the ones from the cups with 0.10% and 0.15% inoculant have liquidus temperatures in a level which may

be slightly lower than the ones from the plain cups. Although it does not require a high energy, it is possible to say that inoculation which provides heterogeneous nucleation sites for graphite particles may help also to the nucleation of pro-eutectic austenite so that 0.05% of inoculant addition may increase the liquidus temperature slightly. Further addition of inoculant (0.10% and 0.15%) can give slight decreases in the liquidus temperature, and this may be explained by that more heterogeneous nucleation sites may not help to the nucleation of pro-eutectic austenite if it is saturated by the nucleation sites, and further inoculation may decrease the liquidus temperature slightly by increasing the carbon equivalent slightly due to the silicon content of the inoculant.

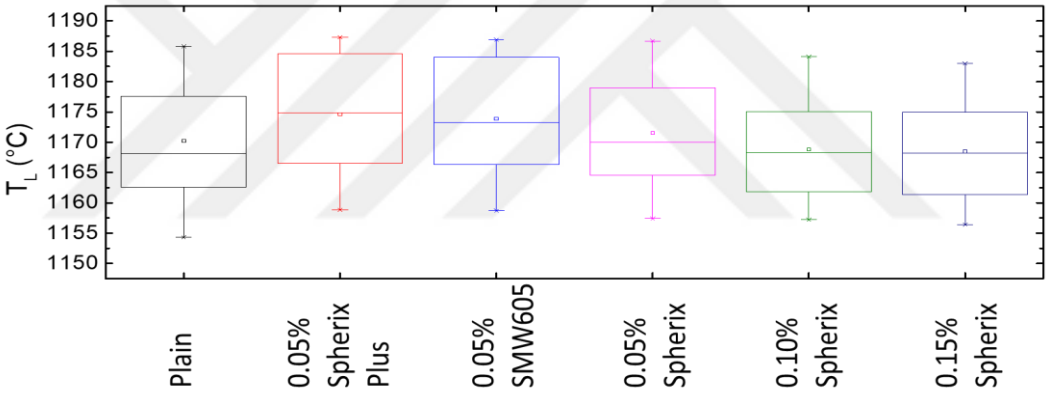

Figure 4.5. Liquidus temperature (TL) versus content of the analysis cup.

Lower eutectic temperature (TEmin) versus content of the analysis cup chart is revealed in Figure 4.6 as box chart. In cooling curve of hypoeutectic ductile iron; after reaching to the equilibrium eutectic transformation temperature, temperature keeps decreasing because graphite nucleation requires excess energy in non-equilibrium cooling conditions, so the melt gets undercooled until a point where there is enough driving force for the graphite particles to nucleate and grow, and that point is attributed as the lower eutectic point. As can be seen in Figure 4.6, the lower eutectic

temperatures of the specimens from the plain cups are considerably lower than the ones of the specimens from the cups with inoculant, and this can be explained by that inoculant provides heterogeneous nucleation sites for the graphite particles so that graphite nucleation requires a lower excess energy, thus less undercooling. By looking at Figure 4.6, it is also possible to say that the lower eutectic temperatures of the specimens from the cups with 0.05% Spherix-Plus™ inoculant may be slightly lower than the ones of the specimens from the other inoculated cups, and this may be explained by that Spherix-Plus™ has calcium, aluminum and antimony as active elements, where the others have calcium, aluminum and bismuth, so effect of bismuth on decreasing the required excess energy for the graphite nucleation may be higher than of antimony. In addition, there is no considerable difference in the lower eutectic temperatures of the specimens from the cups with 0.05%, 0.10% and 0.15% inoculant, so it is possible to say that the melts were saturated by heterogeneous nucleation sites when 0.05% inoculant is added.

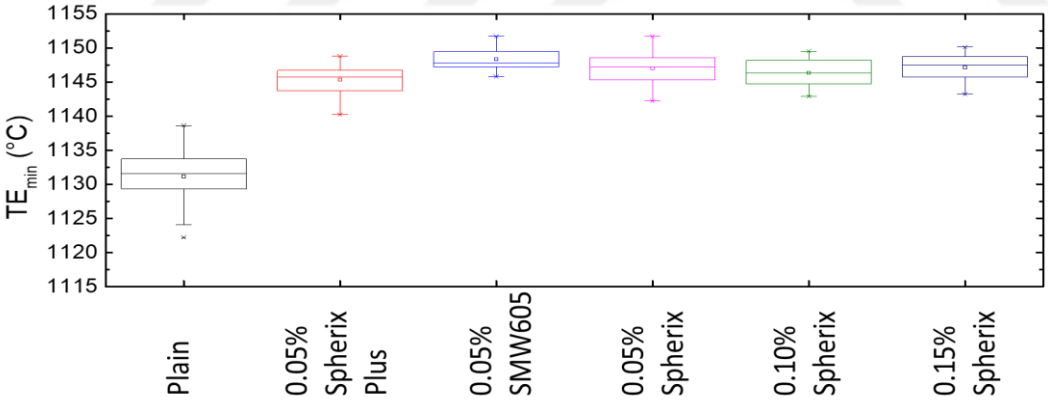

Figure 4.6. Lower eutectic temperature (TEmin) versus content of the analysis cup.

4.4. Metallographic Image Analysis

The main results obtained from the metallographic evaluation of the thermal analysis cup samples by using an image analysis software are listed in Table 4.4.

Table 4.4. *The main results of metallographic image analysis indicating contents of the analysis cups (Content types; 1-Spherix™ inoculant, 2-Sperix-Plus™ inoculant, 3-SMW605™ inoculant, 4-Te and S).*

Ladle	**Cup**	**Content**		**Graphite**	**Nodule Count**	**Nodularity**	**Pearlite**	**Ferrite**
#	*#*	*Type*	*%*	*%*	*1/mm²*	*%*	*%*	*%*
1	1	1	0.05	10.0	819.2	64.2	5.4	94.6
1	2	2	0.05	12.2	717.9	71.9	9.2	90.8
1	3	3	0.05	11.5	971.5	65.4	8.8	91.2
1	4	-	-	12.4	416.9	75.8	28.6	71.4
2	5	1	0.05	13.2	811.9	65.3	4.8	95.2
2	6	2	0.05	12.5	612.3	76.7	17.0	83.0
2	7	3	0.05	10.9	849.2	64.3	16.1	83.9
2	8	-	-	10.5	452.4	71.5	38.7	61.3
3	9	1	0.05	10.1	600.3	74.6	22.2	77.8
3	10	2	0.05	8.8	697.4	70.6	17.9	82.1
3	11	3	0.05	8.8	699.6	69.9	19.7	80.3
3	12	-	-	9.6	392.5	72.7	38.3	61.7
4	13	1	0.05	10.2	767.5	68.5	17.1	82.9
4	14	2	0.05	9.1	571.3	73.1	22.1	77.9
4	15	3	0.05	8.7	680.4	67.3	16.5	83.5
4	16	-	-	9.6	206.0	73.9	49.7	50.3
5	17	1	0.05	9.7	694.9	70.4	24.2	75.8
5	18	2	0.05	8.3	590.6	65.6	18.5	81.5
5	19	3	0.05	8.0	670.1	65.5	14.6	85.4
5	20	-	-	10.4	433.7	75.3	36.5	63.5
6	21	1	0.05	8.4	706.6	66.2	11.8	88.2
6	22	2	0.05	11.4	540.9	73.8	9.5	90.5
6	23	3	0.05	11.9	829.4	65.7	8.2	91.8
6	24	-	-	11.4	401.1	79.0	45.0	55.0
7	25	1	0.05	11.6	779.8	71.5	8.6	91.4
7	26	2	0.05	10.7	516.4	75.4	24.4	75.6
7	27	3	0.05	9.3	756.0	69.9	11.9	88.1
7	28	-	-	10.2	399.5	75.7	37.6	62.4

8	29	1	0.05	10.6	691.2	70.5	16.2	83.8
8	30	2	0.05	10.3	413.2	75.7	32.4	67.6
8	31	3	0.05	11.1	872.4	65.0	10.2	89.8
8	32	-	-	10.5	275.2	79.7	56.2	43.8
9	33	1	0.05	10.8	745.1	66.6	12.5	87.5
9	34	2	0.05	10.6	451.9	76.1	23.4	76.6
9	35	3	0.05	10.6	725.7	68.1	10.9	89.1
9	36	-	-	10.3	342.6	78.1	51.1	48.9
10	37	1	0.05	11.4	839.4	63.8	18.1	81.9
10	38	2	0.05	10.3	609.1	69.5	19.9	80.1
10	39	3	0.05	10.9	884.6	61.4	13.2	86.8
10	40	-	-	10.9	385.6	74.1	41.7	58.3
11	41	-	-	10.4	317.9	77.1	50.5	49.5
11	42	1	0.05	10.2	556.0	70.5	23.1	76.9
11	43	1	0.10	10.0	737.5	69.6	17.2	82.8
11	44	1	0.15	10.0	703.7	70.4	14.4	85.6
12	45	-	-	10.1	332.8	72.7	31.7	68.3
12	46	1	0.05	10.7	712.8	65.5	6.5	93.5
12	47	1	0.10	9.9	804.2	65.5	5.2	94.8
12	48	1	0.15	9.2	768.9	65.9	5.6	94.4
13	49	-	-	8.6	235.8	73.7	61.8	38.2
13	50	1	0.05	10.5	659.7	72.5	19.4	80.6
13	51	1	0.10	9.4	747.5	68.6	13.4	86.6
13	52	1	0.15	10.4	820.4	69.0	11.9	88.1
14	53	-	-	9.2	245.8	72.3	56.8	43.2
14	54	1	0.05	9.7	691.1	71.3	20.5	79.5
14	55	1	0.10	8.4	794.8	64.1	10.8	89.2
14	56	1	0.15	9.7	782.4	69.4	13.1	86.9
15	57	-	-	9.6	350.8	76.2	28.6	71.4
15	58	1	0.05	9.1	728.7	65.4	7.4	92.6
15	59	1	0.10	8.6	636.7	63.9	5.5	94.5
15	60	1	0.15	7.8	666.3	60.0	9.5	90.5
16	61	-	-	10.0	357.9	76.4	39.8	60.2
16	62	1	0.05	8.9	630.1	64.5	7.1	92.9
16	63	1	0.10	8.2	649.6	58.7	5.7	94.3
16	64	1	0.15	7.2	664.0	57.7	7.2	92.8
17	65	-	-	8.5	339.4	71.5	36.3	63.7
17	66	1	0.05	10.8	650.7	68.5	12.6	87.4
17	67	1	0.10	8.7	674.9	62.8	8.2	91.8

17	68	1	0.15	9.1	745.1	60.2	2.9	97.1
18	69	-	-	9.4	346.7	75.4	35.6	64.4
18	70	1	0.05	9.6	735.0	67.3	4.6	95.4
18	71	1	0.10	9.6	814.3	65.2	3.1	96.9
18	72	1	0.15	8.6	767.5	63.1	4.1	95.9
19	73	-	-	10.5	343.5	79.0	49.0	51.0
19	74	1	0.05	11.7	641.2	72.7	20.2	79.8
19	75	1	0.10	11.8	721.5	71.7	15.8	84.2
19	76	1	0.15	9.9	775.8	66.3	8.0	92.0
20	77	-	-	10.9	345.6	78.1	30.7	69.3
20	78	1	0.05	12.3	664.7	73.0	7.1	92.9
20	79	1	0.10	9.7	810.7	66.6	7.0	93.0
20	80	1	0.15	9.8	810.0	66.5	4.6	95.4
21	81	1	0.05	6.8	637.7	58.0	5.0	95.0
21	82	2	0.05	8.0	536.6	66.6	2.4	97.6
21	83	3	0.05	8.3	710.3	57.8	4.7	95.3
21	84	-	-	8.3	435.2	72.2	1.8	98.2
22	85	1	0.05	11.2	768.3	63.5	0.4	99.6
22	86	2	0.05	10.9	638.3	68.5	2.5	97.5
22	87	3	0.05	8.6	711.8	62.0	5.2	94.8
22	88	-	-	6.5	435.8	69.8	4.5	95.5
23	89	1	0.05	9.6	758.7	67.5	0.0	100.0
23	90	2	0.05	9.7	608.7	69.1	3.6	96.4
23	91	3	0.05	9.1	789.1	65.3	5.0	95.0
23	92	-	-	5.7	426.4	67.3	2.8	97.2
24	93	1	0.05	9.7	669.0	67.1	0.0	100.0
24	94	2	0.05	9.5	547.6	70.2	0.0	100.0
24	95	3	0.05	10.7	864.0	63.3	0.0	100.0
24	96	-	-	6.4	387.1	70.9	3.9	96.1
25	97	1	0.05	10.9	812.7	62.3	0.0	100.0
25	98	2	0.05	9.8	535.5	75.3	2.0	98.0
25	99	3	0.05	9.8	753.7	66.4	1.0	99.0
25	100	-	-	6.2	410.7	72.4	3.9	96.1
26	101	1	0.05	9.6	830.5	60.4	0.3	99.7
26	102	2	0.05	9.5	501.7	74.3	1.9	98.1
26	103	3	0.05	11.5	846.9	59.3	0.0	100.0
26	104	-	-	6.6	310.3	70.2	5.4	94.6
27	105	1	0.05	9.4	637.2	71.5	0.7	99.3
27	106	2	0.05	9.7	520.8	77.8	0.4	99.6

27	107	3	0.05	9.6	867.9	63.4	0.0	100.0
27	108	-	-	6.6	416.5	68.2	4.4	95.6
28	109	1	0.05	9.5	695.9	68.5	1.8	98.2
28	110	2	0.05	9.3	546.6	73.7	2.8	97.2
28	111	3	0.05	9.4	683.5	68.1	2.9	97.1
28	112	-	-	7.2	402.8	74.7	2.7	97.3
29	113	1	0.05	9.7	789.1	66.7	0.7	99.3
29	114	2	0.05	9.6	540.0	77.2	1.6	98.4
29	115	3	0.05	9.6	791.6	66.0	2.0	98.0
29	116	-	-	6.8	384.1	70.5	4.6	95.4
30	117	1	0.05	10.6	902.7	60.4	0.9	99.1
30	118	2	0.05	10.3	460.0	77.1	2.2	97.8
30	119	3	0.05	9.2	860.7	58.0	0.3	99.7
30	120	-	-	7.0	283.1	72.5	6.1	93.9
31	121	-	-	6.3	380.2	68.4	5.6	94.4
31	122	1	0.05	5.1	523.5	62.4	3.7	96.3
31	123	1	0.10	5.5	448.0	63.9	3.0	97.0
31	124	1	0.15	6.4	631.4	65.0	2.9	97.1
32	125	-	-	6.5	371.1	70.1	5.4	94.6
32	126	1	0.05	7.0	468.8	70.0	2.8	97.2
32	127	1	0.10	5.4	518.7	66.1	3.1	96.9
32	128	1	0.15	4.9	525.8	61.1	3.7	96.3
33	129	-	-	6.4	349.4	69.8	6.0	94.0
33	130	1	0.05	7.4	458.9	75.9	3.1	96.9
33	131	1	0.10	6.5	503.1	72.2	3.0	97.0
33	132	1	0.15	7.1	563.0	73.3	2.7	97.3
34	133	-	-	7.5	402.4	73.5	4.3	95.7
34	134	1	0.05	6.8	468.3	74.1	3.7	96.3
34	135	1	0.10	6.3	475.0	70.4	4.1	95.9
34	136	1	0.15	6.4	637.6	68.6	3.5	96.5
35	137	-	-	6.7	432.1	71.0	2.8	97.2
35	138	1	0.05	5.8	484.5	65.6	2.2	97.8
35	139	1	0.10	5.3	467.5	66.8	3.1	96.9
35	140	1	0.15	5.8	537.9	69.1	3.5	96.5
36	141	-	-	6.4	451.5	71.1	2.0	98.0
36	142	1	0.05	5.8	529.5	68.7	2.4	97.6
36	143	1	0.10	6.8	521.4	73.8	3.0	97.0
36	144	1	0.15	7.6	540.0	75.4	2.3	97.7
37	145	-	-	7.0	373.4	75.2	4.1	95.9

37	146	1	0.05	6.2	464.8	70.6	3.1	96.9
37	147	1	0.10	6.0	501.4	71.0	2.5	97.5
37	148	1	0.15	5.3	514.2	67.2	3.1	96.9
38	149	-	-	6.3	355.4	68.5	3.8	96.2
38	150	1	0.05	6.6	465.5	73.8	4.4	95.6
38	151	1	0.10	6.4	525.6	65.0	2.3	97.7
38	152	1	0.15	6.0	517.1	66.3	2.4	97.6
39	153	-	-	7.2	382.0	73.2	6.8	93.2
39	154	1	0.05	6.6	533.8	73.1	3.8	96.2
39	155	1	0.10	7.3	540.8	75.2	2.7	97.3
39	156	1	0.15	6.9	569.7	72.5	2.9	97.1
40	157	-	-	6.7	337.3	71.2	4.5	95.5
40	158	1	0.05	6.4	569.1	69.2	3.2	96.8
40	159	1	0.10	6.2	591.3	69.4	3.1	96.9
40	160	1	0.15	6.3	599.9	68.7	3.0	97.0

Graphite phase area percentage versus alloy grade chart is revealed in Figure 4.7 as box chart. As can be seen in Figure 4.8, in general, the specimens of EN-GJS-600-10C grade may have a lower percentage of graphite phase than that the ones of EN-GJS-400-18 do. This may be explained by the lower carbon content of EN-GJS-600-10C grade. Although silicon is a graphite former and this grade has a high silicon content, if the carbon content is low, the amount of graphite that can be formed is limited.

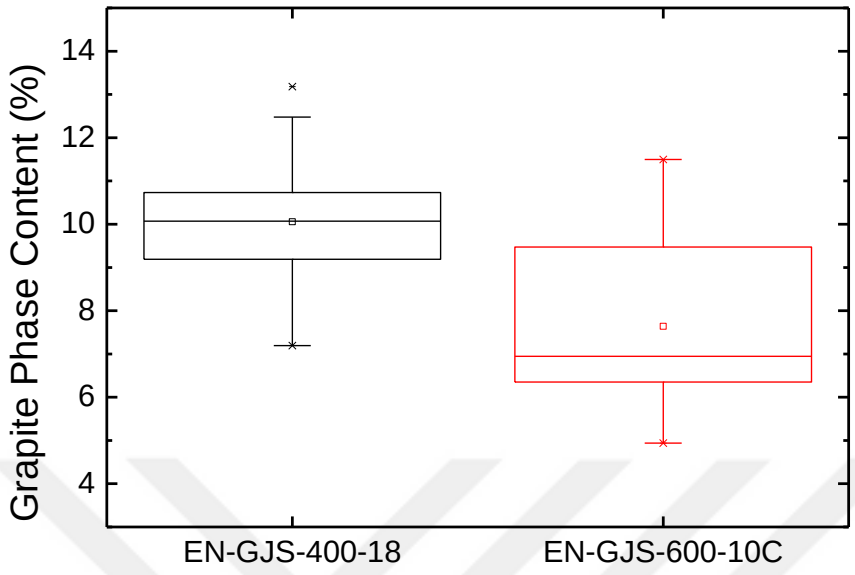

Figure 4.7. Graphite phase area percentage versus alloy grade.

Graphite nodule count per unit area versus content of the analysis cup chart is revealed in Figure 4.9 as box chart. The aim of the inoculant addition is to provide heterogeneous nucleation sites for the graphite nucleation. As can be seen in Figure 4.9, the nodule counts of the specimens from the plain cups are considerably lower than the ones of the specimens from the cups with inoculant, and this can be explained by that inoculant provides heterogeneous nucleation sites for the graphite particles, so a higher number of graphite nucleus forms and becomes graphite nodules as a result of growth. By looking at Figure 4.9, it is also possible to say that the nodule counts of the specimens from the cups with 0.05% Spherix-Plus^{TM} inoculant may be slightly lower than the ones of the specimens from the other inoculated cups, and this may be explained by that Spherix-Plus^{TM} has calcium, aluminum and antimony as active elements, where the others have calcium, aluminum and bismuth, so effect of bismuth on providing heterogeneous nucleation sites for the graphite particles may be higher than of antimony. In addition, there is no considerable difference in the nodule counts

of the specimens from the cups with 0.05%, 0.10% and 0.15% Spherix^{TM} inoculant, but the ones from the cups with 0.05% SMW605 inoculant may have slightly higher nodule counts. Therefore, it is possible to say that the melts were saturated by heterogeneous nucleation sites when 0.05% inoculant is added, and SMW605 inoculant may increase the nodule count slightly more than that Spherix^{TM} inoculant does which may be a result of higher calcium and rare earth metals content of SMW605^{TM} (see Table 3.4).

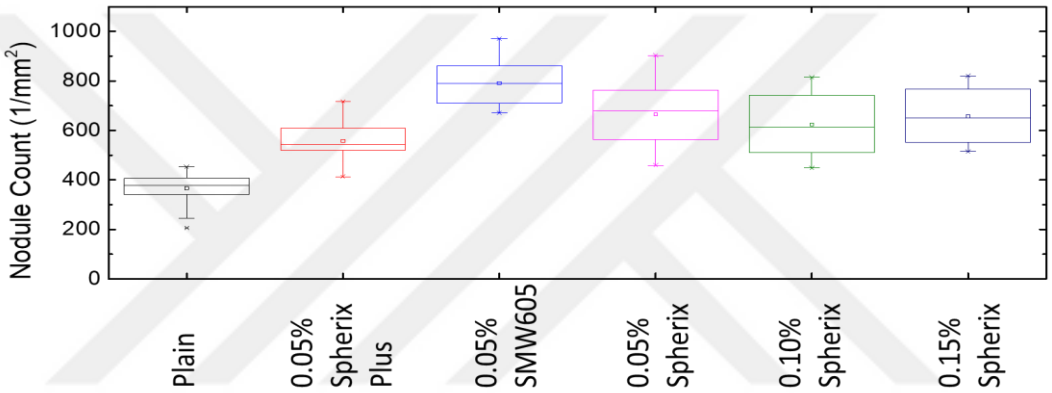

Figure 4.8. Graphite nodule count per unit area versus content of the analysis cup.

Graphite shape nodularity percentage versus content of the analysis cup chart is revealed in Figure 4.10 as box chart. By the magnesium treatment, content of the surface-active elements (oxygen and sulphur) reduces, and this increases the interface energy between graphite and iron which makes increasing the volume/surface-area ratio of the graphite particles thermodynamically more feasible, so it makes the high nodularity graphite shape more stable. According to the solidification model suggested by J. Zhou et al., when the diameter of graphite nodule exceeds a certain value, it gets surrounded by austenite dendrite arms terminating its contact with liquid phase, and that limits further growth of graphite nodule by the limited rate of solid state diffusion [26]. In addition, since during the austenite envelopment, the parts of

the graphite nodule which have not been enveloped will be in contact with liquid and will grow much faster than the enveloped parts due to the much higher diffusion rate, the speed that graphite nodule gets enveloped by austenite has a significant effect on the graphite shape [26]. Therefore, it is possible to say that content of the surface-active elements defines the thermodynamic feasibility of high nodularity graphite shape, where the speed that graphite nodule gets enveloped by austenite defines the kinetic limitation of it. As can be seen in Figure 4.10, the nodularity of the specimens from the plain cups is higher than the nodularity of the specimens from the cups with inoculant. While inoculant master alloys are creating heterogeneous nucleation sites, they bond oxygen and sulphur chemically, so content of the surface-active elements decreases further, and thermodynamic stability of high nodularity increases further. Therefore, it is expected the inoculants to have a positive effect on the nodularity which is the opposite of the observed effect. On the other hand, if we consider the kinetic factors, J. Zhou et al. claims that bismuth and antimony are two of the elements that favor the slower envelopment of graphite by decreasing the growth rate of austenite dendrites [26]. Since the inoculants that were used contain either bismuth or antimony, the negative effect on the nodularity may be explained by this kinetic limitation. By looking at Figure 4.10, it is also possible to say that the nodularity of the specimens from the cups with 0.05% Spherix-Plus™ inoculant is slightly higher than the nodularity of the specimens from the other inoculated cups. Although there is no study found for such a comparison, this observation may indicate that bismuth may have a higher effect on lowering the envelopment speed than that antimony does.

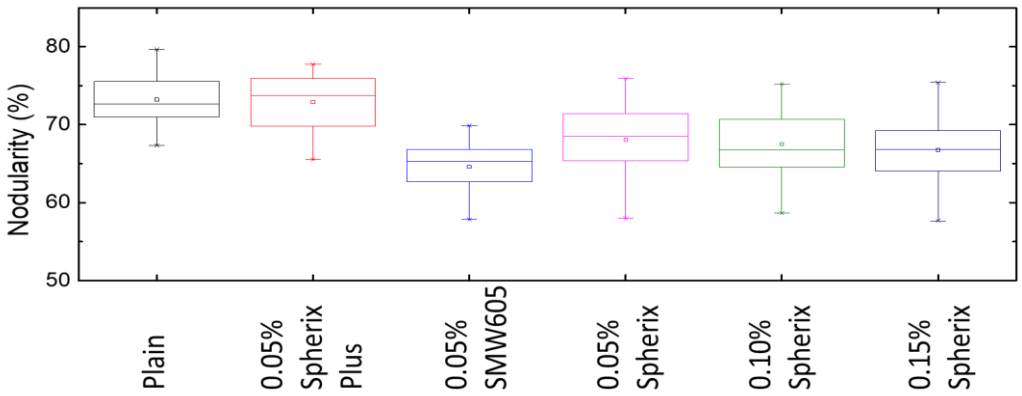

Figure 4.9. Graphite shape nodularity percentage versus content of the analysis cup.

4.5. Regression Analysis

Ferrite phase area percentage versus graphite nodule count per unit are graph is revealed in Figure 4.11 as point scatter. Blue points indicate the cups with the alloy EN-GJS-400-18, where the orange ones indicate the cups with the alloy EN-GJS-600-10C. As can be seen in Figure 4.11, for both alloy grades, the ferrite content increases when the nodule count increases, and this can be explained by that higher number of graphite nodules per unit area decreases the length of the diffusion path of carbon atoms to reach to the graphite phase, and this decreases the carbon content in the matrix, thus the possibility to form pearlite. Equation and r-square value of the found linear regression for the grade EN-GJS-400-18 are also revealed in Figure 4.11, and it estimates around 7% increase in the ferrite content as the nodule count increases 100 $1/mm^2$. For the grade EN-GJS-600-10C, there could not be found a considerable correlation since its specimens have almost no pearlite.

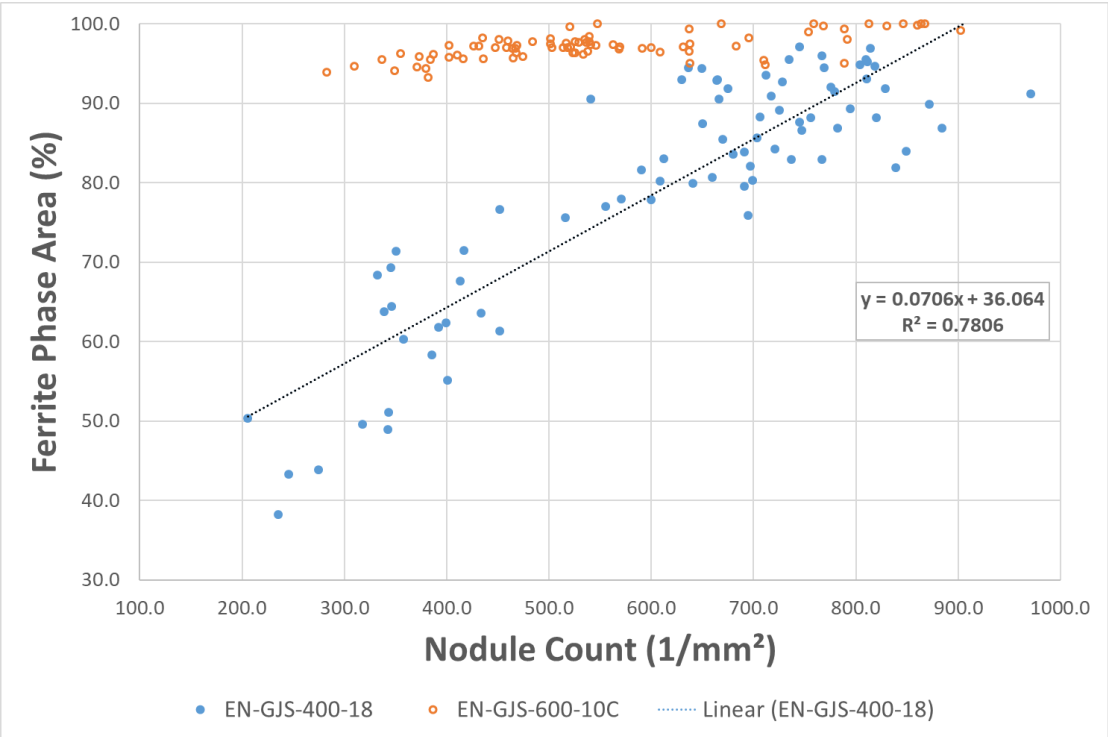

Figure 4.10. Ferrite phase area percentage versus graphite nodule count per unit area graph indicating the alloy grades and linear regression found for the grade EN-GJS-400-18.

The etched specimen micrographs at 100X magnification; from the ladle 2, sample numbers a) 5 (with 0.05% Spherix^{TM}) and b) 8 (Plain); from the ladle 6, sample numbers c) 23 (with 0.05% SMW605^{TM}) and d) 24 (Plain); from the ladle 9, sample numbers e) 35 (with 0.05% SMW605^{TM}) and f) 36 (Plain) were revealed in Figure 4.11. Since the samples from the same ladle have the similar chemical compositions but different inoculation conditions, they can reveal the effect of graphite nodule count per unit area on the ferrite phase content. A) sample 5 has 811.9 nodules per mm^2 and 95.2% of ferrite content where b) sample 8 has 452.4 nodules per mm^2 and 61.3% of ferrite content; c) sample 23 has 829.4 nodules per mm^2 and 91.8% of ferrite content where d) sample 24 has 401.1 nodules per mm^2 and 55.0% of ferrite content; e) sample 35 has 725.7 nodules per mm^2 and 89.1% of ferrite content where f) sample 36 has 342.6 nodules per mm^2 and 48.9% of ferrite content. It can be seen clearly in Figure 4.11 that as the graphite nodule count per unit area decreases, ferrite phase content decreases too.

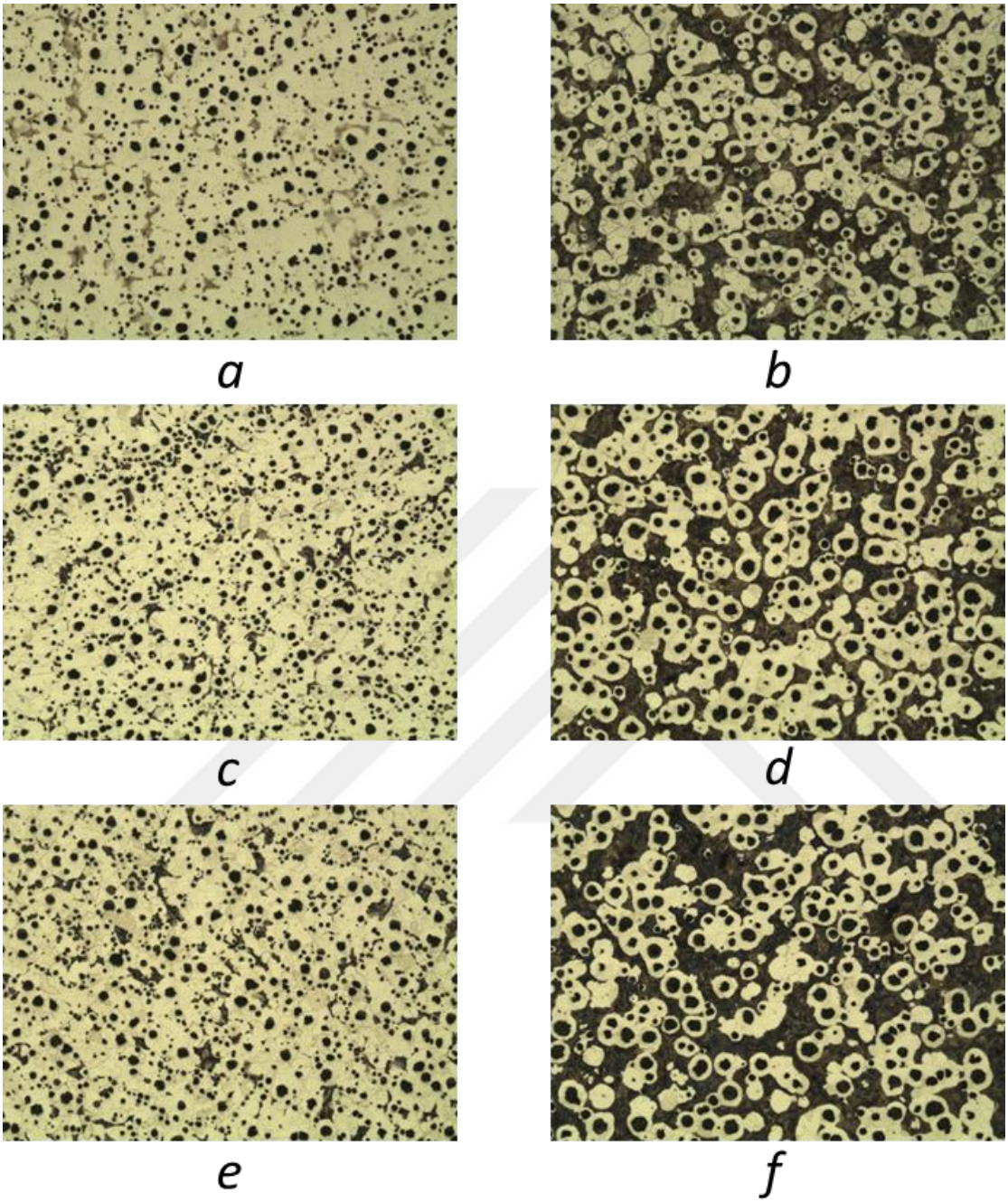

Figure 4.11. Micrographs of some of the etched specimens at 100X magnification. a) Cup ID = 5, PD = 811.9, %Fer = 95.2. b) Cup ID = 8, PD = 452.4, %Fer = 61.3. c) Cup ID = 23, PD = 829.4, %Fer = 91.8. d) Cup ID = 24, PD = 401.1, %Fer = 55.0. e) Cup ID = 35, PD = 725.7, %Fer = 89.1. f) Cup ID = 36, PD = 342.6, %Fer = 48.9.

Since two alloy grades have a high difference in silicon content which affects both stable and metastable eutectic transformation temperatures, the regression analysis corresponding the eutectic part parameters of the cooling curves are conducted separately for two grades.

Lower eutectic temperature (TEmin) and graphite nodule count per unit area are two of the parameters expected to be related. Although there is a linear relationship between those two parameters, it is not valid for the higher TEmin values due to the saturation. Therefore, applying a non-linear fit could make more sense. Lower eutectic temperature (TEmin) versus graphite nodule count per unit area graphs for the grades EN-GJS-400-18 and EN-GJS-600-10C are revealed in Figure 4.12 and Figure 4.13 indicating content of the analysis cup and logistic function fits which give sigmoid curves. Logistic functions giving the sigmoid curves are also revealed on the related graphs. In Figure 4.14 and Figure 4.15, lower eutectic temperature calculated by logistic function fit versus measured lower eutectic temperature graphs revealing the r-square values for the grades EN-GJS-400-18 and EN-GJS-600-10C are given in order to check success of the logistic function fits on linear basis. Effects of content of the analysis cup on lower eutectic temperature and graphite nodule count per unit area were discussed before. As can be seen in Figure 4.12 and Figure 4.13, when the nodule count goes from zero to the infinity, sigmoid curve assumes for the lower eutectic temperature; first an exponential-like increase, then a nearly linear increase followed by a logarithmic-like path. If the heterogeneous nucleation sites are insufficient, the melt undercools until there is enough driving force for the graphite nucleation, but there is a lowest possible TEmin level at which metastable eutectic transformation temperature is reached, and instead of graphite, cementite forms which does not require excess energy to nucleate. As the sigmoid curve suggests, at this lowest TEmin level, the nodule count is expected to be zero, since there will be no graphite phase in the structure. Then, when TEmin increases slightly, there will be a mottled iron structure which is a hybrid of grey and white cast iron where there are both graphite and cementite in the structure, and there the sigmoid curve suggests an

exponential-like relation between TEmin and the nodule count since TEmin will increase rapidly as white cast iron content decreases, graphite content increases. After the mottled iron zone terminates and fully grey iron structure starts, the sigmoid curve suggests a nearly linear relation, since both TEmin and nodule count are dependent on the number of heterogeneous nucleation sites for the graphite particles. As the number of heterogeneous nucleation sites increases, there will be less and less undercooling required for the graphite nucleation, and TEmin will approach to the stable eutectic transformation temperature by following a logarithmic-like relation with the nodule count which means that it loses its effect on the nodule count because the number of heterogeneous nucleation sites is not the limiting factor for the nodule count any more. After TEmin reaches to the stable eutectic transformation temperature, number of the graphite nucleus formed is not the limiting factor for the nodule count, and it is mainly controlled by the possibility of the growing graphite nucleus to join one another due to the low distance in between. At the lower (white and mottled iron) part of the sigmoid curves, there are not much data points, since the foundry at which the data were collected, has a cored-wire inoculation practice in the ladle simultaneously with the Mg treatment, and it introduces heterogeneous nucleation sites preventing white or mottled iron formation.

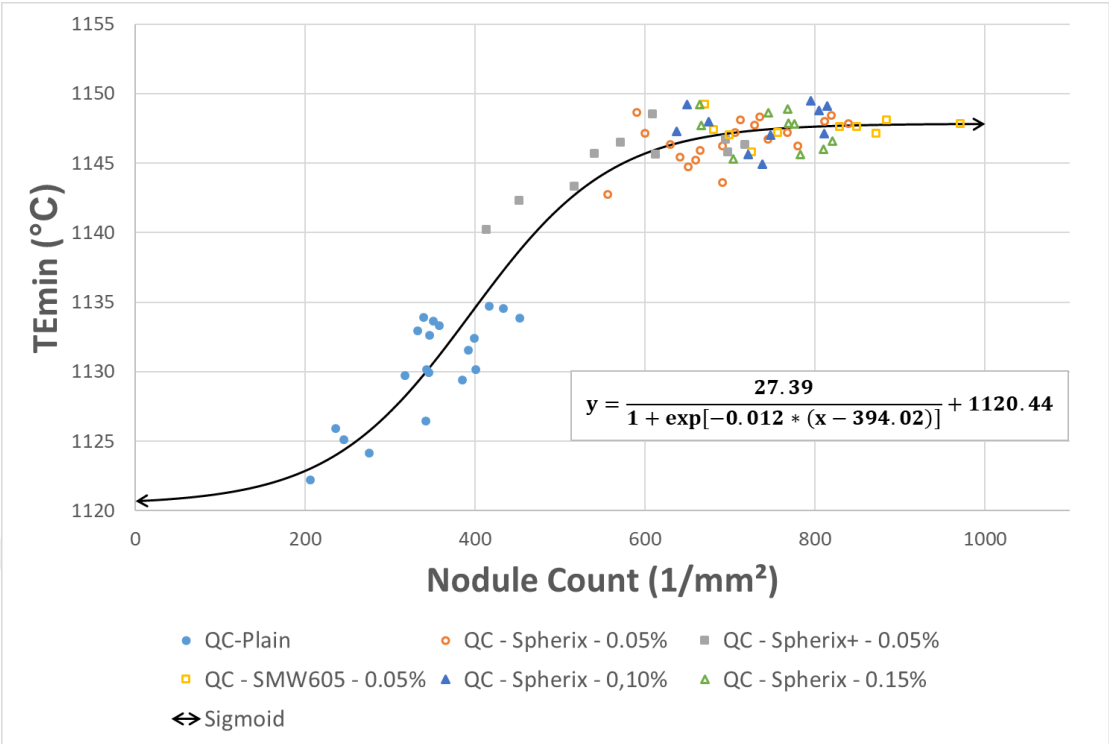

Figure 4.12. Lower eutectic temperature (TEmin) versus graphite nodule count per unit area graph for the grade EN-GJS-400-18 indicating content of the analysis cup and logistic function fit.

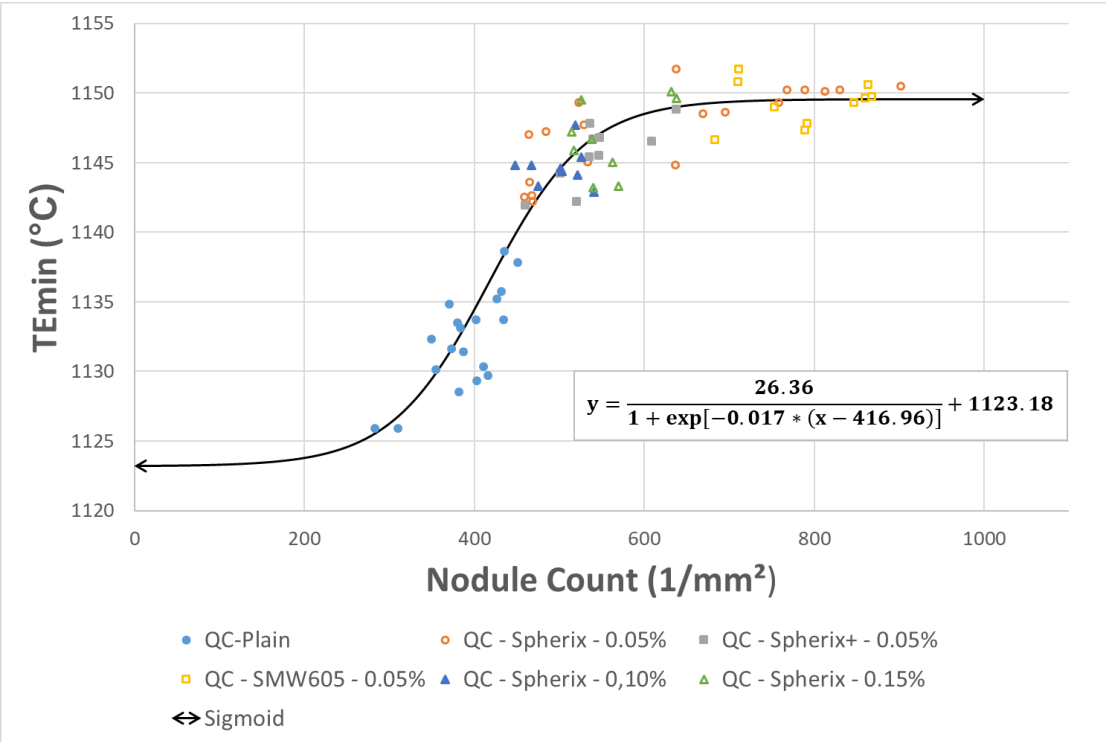

Figure 4.13. Lower eutectic temperature (TEmin) versus graphite nodule count per unit area graph for the grade EN-GJS-600-10C indicating content of the analysis cup and logistic function fit.

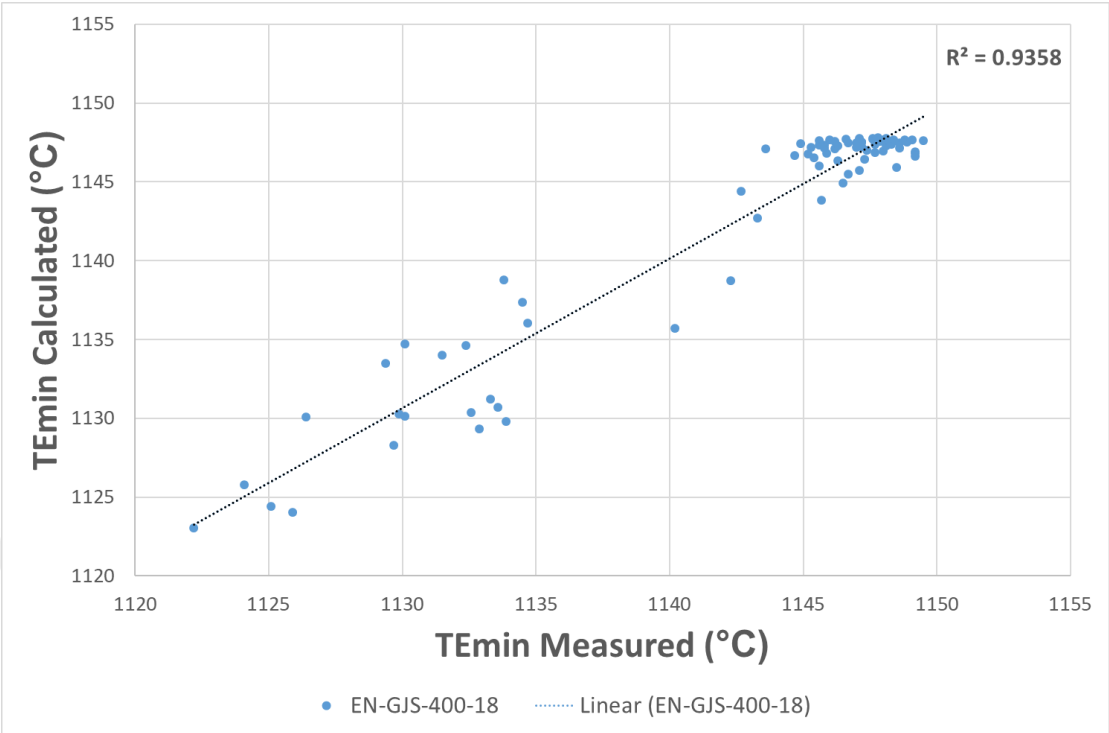

Figure 4.14. Lower eutectic temperature calculated by logistic function fit versus measured lower eutectic temperature graph for the grade EN-GJS-400-18.

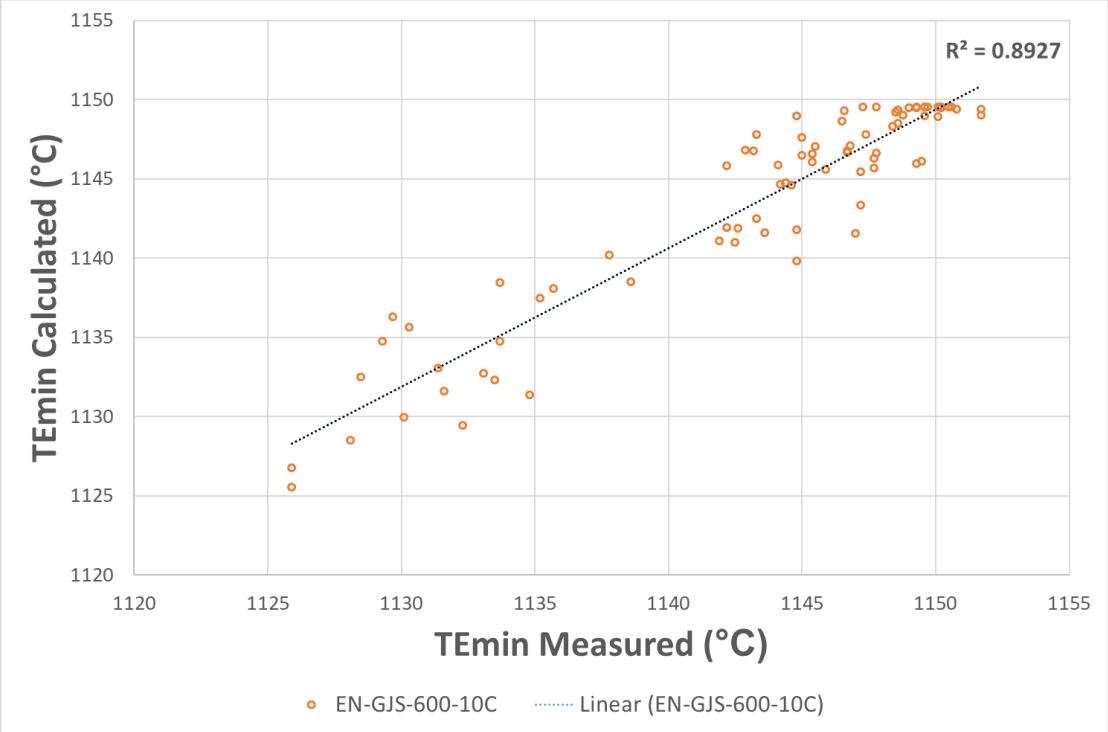

Figure 4.15. Lower eutectic temperature calculated by logistic function fit versus measured lower eutectic temperature graph for the grade EN-GJS-600-10C.

The unetched specimen micrographs at 100X magnification; for the alloy EN-GJS-400-18, from the ladle 8, sample numbers a) 29 (with 0.05% Spherix^{TM}), b) 30 (with 0.05% SpherixPlus^{TM}), c) 31 (with 0.05% SMW605^{TM}) and d) 32 (Plain); for the alloy EN-GJS-600-10C, from the ladle 24, sample numbers e) 93 (with 0.05% Spherix^{TM}), f) 94 (with 0.05% SpherixPlus^{TM}), g) 95 (with 0.05% SMW605^{TM}) and h) 96 (Plain) were revealed in Figure 4.16. As EN-GJS-400-18 samples; a) sample 29 has 691.2 nodules per mm^2 and its TEmin value is 1143.6°C, b) sample 30 has 413.2 nodules per mm^2 and its TEmin value is 1140.2°C, c) sample 31 has 872.4 nodules per mm^2 and its TEmin value is 1147.1°C and d) sample 32 has 275.2 nodules per mm^2 and its TEmin value is 1124.1°C. As EN-GJS-600-10C samples; e) sample 93 has 669.0 nodules per mm^2 and its TEmin value is 1148.5°C, f) sample 94 has 547.6 nodules per mm^2 and its TEmin value is 1146.8°C, g) sample 95 has 864.0 nodules per mm^2 and its TEmin value is 1150.6°C and h) sample 96 has 387.1 nodules per mm^2 and its

TEmin value is 1131.4°C. It can be seen in Figure 4.16 that for both alloy types, as lower eutectic temperature (TEmin) increases, the graphite nodule count per unit area increases too.

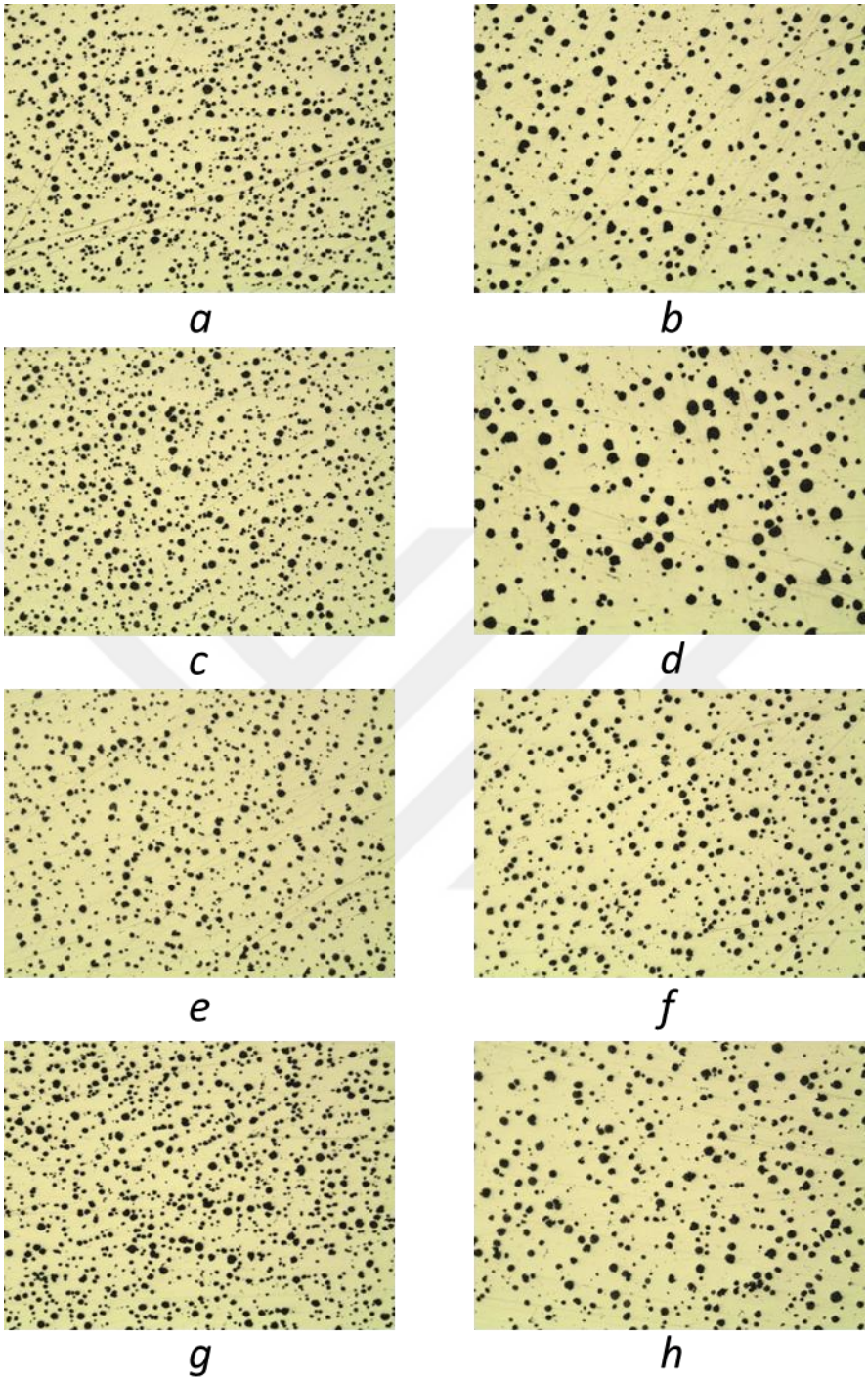

Figure 4.16. Micrographs of some of the unetched specimens at 100X magnification. a) Cup ID = 29, TEmin = 1143.6, PD = 691.2. b) Cup ID = 30, TEmin = 1140.2, PD = 413.2. c) Cup ID = 31, TEmin = 1147.1, PD = 872.4. d) Cup ID = 32, TEmin = 1124.1, PD = 275.2. e) Cup ID = 93, TEmin = 1148.5, PD = 669.0. f) Cup ID = 94, TEmin = 1146.8, PD = 547.6. g) Cup ID = 95, TEmin = 1150.6, PD = 864.0. h) Cup ID = 96, TEmin = 1131.4, PD = 387.1.

Since oxygen is a surface active element decreasing the interface energy between iron and graphite, active oxygen amount representing the free or not chemically bonded oxygen which is the one acting as surface active element is expected to have an effect on the graphite shape such that lower amount of active oxygen provides a higher interface energy between iron and graphite, thus a better graphite shape nodularity. In Figure 4.16, Graphite shape nodularity percentage of the specimens from plain cups versus active oxygen amount (aO) measured in the ladle graph is given as point scatter. Blue points indicate the cups with the alloy EN-GJS-400-18, where the orange ones indicate the cups with the alloy EN-GJS-600-10C. The specimens from plain cups are chosen because they are the ones representing the melt whose active oxygen amount was measured in the ladle, since further inoculant addition in the analysis cup decreases the active oxygen amount further by bonding it chemically to form heterogeneous nucleation sites. As can be seen in Figure 4.16, there could not be found any clear relation between active oxygen content and the nodularity. As discussed previously, content of the surface-active elements defines the thermodynamic feasibility of forming sphere-like graphite particles, but there are also kinetic (diffusion-dependent) factors like the speed at which graphite particles are enveloped by austenite dendrite arms affecting the graphite shape nodularity. In addition, since the data were collected in a real production environment, both active oxygen content and the nodularity values are in narrow ranges giving optimal performance for the resulting products, and in the case, all the specimens have a similar thermodynamic stability level for the high nodularity, so kinetic factors are expected to play the key role in defining the nodularity. Manipulating the active oxygen content by changing the magnesium level introduced by the treatment might reveal its effect on the nodularity. The results of the study conducted by F. Mampaey et al. which were revealed in Figure 2.18 also proves that such a low amount of variation in active oxygen content does not create a considerable effect on the nodularity [37].

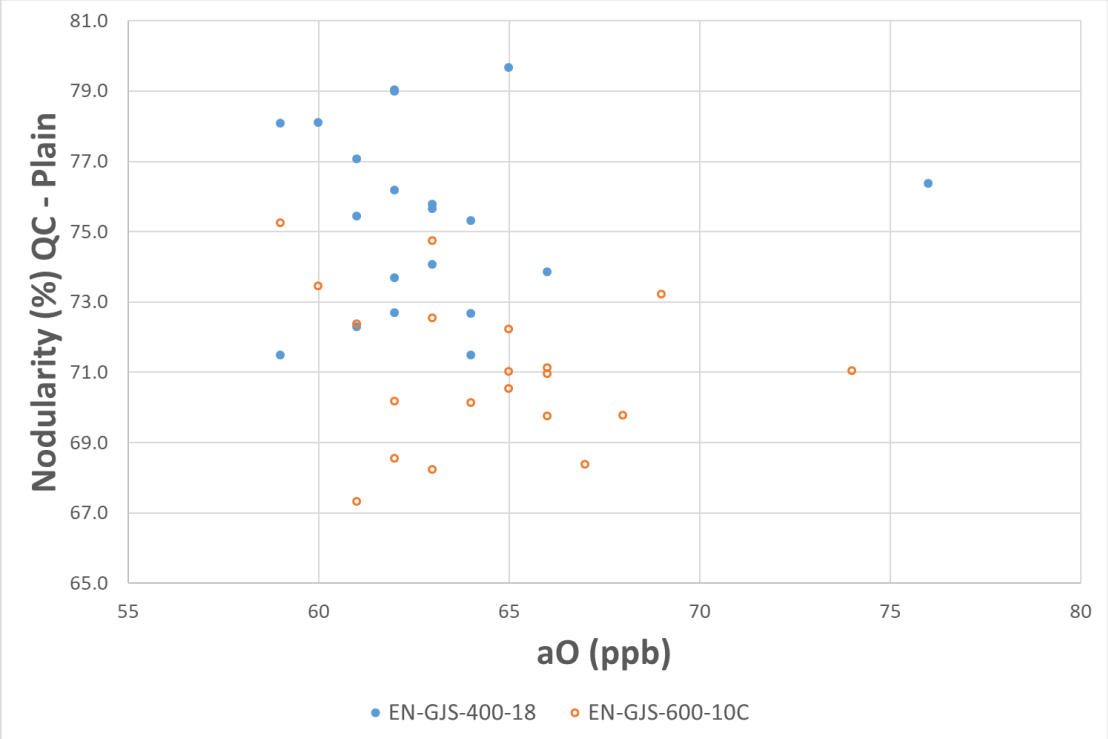

Figure 4.17. Graphite shape nodularity percentage of the specimens from plain cups versus active oxygen amount (aO) measured in the ladle graph indicating the alloy grades.

The unetched specimen micrographs at 100X magnification; for the alloy EN-GJS-400-18, a) from the ladle 12, sample 45 (Plain), b) from the ladle 15, sample 57 (Plain) and c) from the ladle 6, sample 24 (Plain); for the alloy EN-GJS-600-10C, d) from the ladle 27, sample 108 (Plain), e) from the ladle 30, sample 120 (Plain) and f) from the ladle 28, sample 112 (Plain) were revealed in Figure 4.18. Since the active oxygen content measurements were done in the ladle, and the samples from the plain analysis cups represent the melt in the ladle, only the samples from the plain cups were chosen for the active oxygen content comparison. For the alloy EN-GJS-400-18, although the ladles 12, 15 and 6 have the same amount of active oxygen content which is 62 ppb; a) sample 45 has 72.7% of graphite shape nodularity, b) sample 57 has 76.2% of graphite shape nodularity and c) sample 24 has 79.0%. of graphite shape nodularity. For the alloy EN-GJS-600-10C, although the ladles 27, 30 and 28 have the same

amount of active oxygen content which is 63 ppb; d) sample 108 has 68.2% of graphite shape nodularity, e) sample 120 has 72.5% of graphite shape nodularity and f) sample 112 has 74.7%. of graphite shape nodularity. On the other hand, as it can be seen in Figure 4.18, there is no significant difference in nodule shapes because the variation in graphite shape nodularity is not as high as that it can be seen clearly.

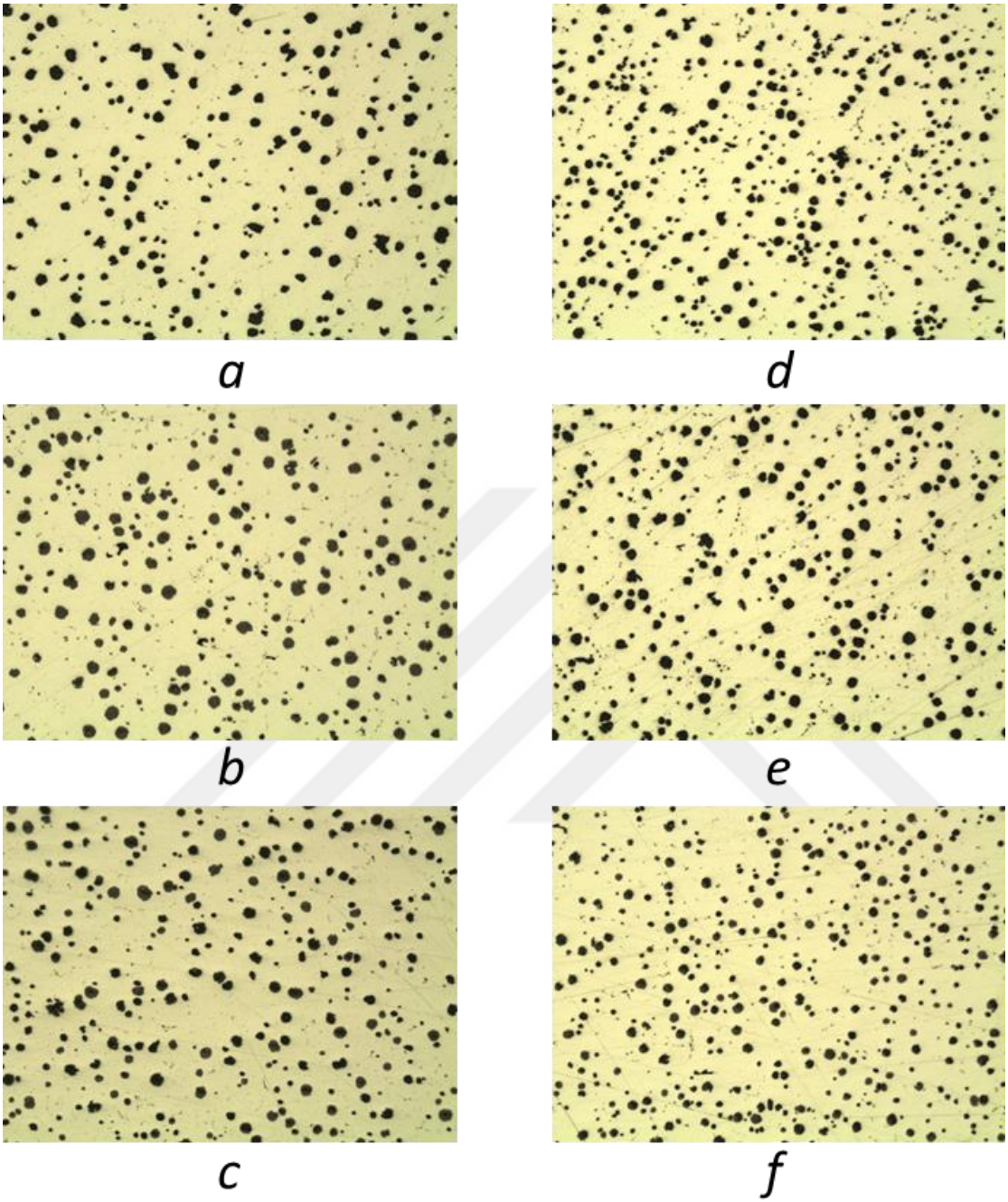

Figure 4.18. Micrographs of some of the unetched specimens at 100X magnification. a) Cup ID = 45, aO = 62 ppb, %Nod = 72.7. b) Cup ID = 57, aO = 62 ppb, %Nod = 76.2. c) Cup ID = 24, aO = 62 ppb, %Nod = 79.0%. d) Cup ID = 108, aO = 63 ppb, %Nod = 68.2. e) Cup ID = 120, aO = 63 ppb, %Nod = 72.5. f) Cup ID = 112, aO = 63, %Nod = 74.7.

CHAPTER 5

CONCLUSIONS

By this study on the cooling curve thermal analyses and oxygen activity analyses for the estimation of microstructural properties of nodular cast iron, the following main conclusions have been pointed out:

1. It was observed that the specimens of EN-GJS-600-10C grade have a higher liquidus temperature level compared to EN-GJS-400-18 which is an expected effect of the difference in their carbon equivalents. Average liquidus temperature difference among two alloys was 15.0^{o}C, and the average carbon equivalent difference among two alloys was 0.17%.

2. It was observed that the specimens from plain analysis cups have lower upper eutectic temperature (TEmax) values compared to the inoculant containing analysis cups. Moreover, TEmax values of the specimens from inoculant containing cups are mostly accumulated in a narrow range. For non-inoculated cups, TEmax is limited by the low density of graphite particles. On the other hand, TEmax values of the inoculated specimens are limited by the stable eutectic transformation temperature. Therefore, TEmax values of inoculated EN-GJS-EN-400-18 specimens are aligned at around 1152°C which is the stable eutectic transformation temperature. On the other hand, the inoculated EN-GJS EN-GJS-600-10C specimens have TEmax values aligned at around 1154°C. That 2°C of difference can be explained by the effect of silicon content on the stable eutectic transformation temperature.

3. It was observed that the cooling curves of EN-GJS-600-10C specimens have less time differences between the lower eutectic point and the end of freezing point compared to EN-GJS-400-18 grade. These two points correspond to the start and the end of graphite phase growth. Moreover, according to metallographic image analysis

results, the specimens of EN-GJS-600-10C grade have lower quantity of graphite phase in their structure. Therefore, the lower total duration of eutectic transformation arises from earlier termination of graphite phase growth.

4. It was observed that the specimens from the cups having 0.05% of inoculant have liquidus temperatures in a similar level which is slightly higher compared to the plain cups. In addition, the specimens from the cups having 0.10% and 0.15% inoculant have liquidus temperatures in a level which is slightly lower compared to the plain cups. Although pro-eutectic austenite nucleation does not require a high quantity of excess energy, inoculant seems to help to the nucleation of pro-eutectic austenite so that 0.05% of inoculant addition increases the liquidus temperature slightly. Further addition of inoculant (0.10% and 0.15%) gave slight decrease in the liquidus temperatures, and this can be explained by that the melt was saturated by the nucleation sites, and further inoculation decreased the liquidus temperature by increasing the carbon equivalent due to the silicon content of the inoculant.

5. It was observed that lower eutectic temperature (TEmin) values of the specimens from plain cups are considerably lower compared to the inoculated cups. Due to the presence of inclusion forming elements such as Ca, Al, Ce, Bi and Sb, inoculant provides heterogeneous nucleation sites for the graphite phase so that graphite nucleation requires a lower excess energy, thus less undercooling. In addition, TEmin values of the specimens from the cups having Sb containing inoculant are slightly lower compared to Bi containing inoculant. Therefore, inoculation effect of Bi may be higher compared to Sb.

6. It was observed that the specimens of EN-GJS-600-10C grade have a lower percentage of graphite phase compared to EN-GJS-400-18 which is a result of the lower carbon content of EN-GJS-600-10C grade. Although silicon is a graphite former and this grade has a high silicon content, if the carbon content is low, the amount of graphite that can be formed is limited.

7. It was observed that graphite nodule count per unit area values of the specimens from plain cups are considerably lower compared to the inoculated cups. It is because heterogeneous nucleation sites provided by the inoculant yield in a higher quantity of graphite nucleus formation which become graphite nodules as a result of growth. In addition, the nodule counts of the specimens from the cups having Sb containing inoculant are slightly lower compared to Bi containing inoculant. Therefore, inoculation effect of Bi may be higher compared to Sb.

8. It was observed that graphite shape nodularity percentage values of the specimens from plain cups are considerably higher compared to the inoculated cups. The theory proposed by Zhou et al. claims a negative effect of Bi and Sb on the graphite shape nodularity [26]. Since the inoculants that were used contain either Bi or Sb, the negative effect claimed by the theory was observed on the structure of the inoculated cup specimens.

9. It was observed that for both alloy grades, ferrite phase area percentage increases when graphite nodule count per unit area increases. Higher number of graphite nodules per unit area decreases the length of the diffusion path of carbon atoms to reach to the graphite phase. Therefore, as the nodule count increases, carbon content in the matrix decreases, and ferrite content increases. For the grade EN-GJS-400-18, as a result of linear regression analysis, it was found that each 100 nodules per mm^2 yields in 7% increase in the ferrite content. For the grade EN-GJS-600-10C, there could not be found a considerable regression since its specimens had almost no pearlite.

10. It was observed that lower eutectic temperature (TEmin) versus graphite nodule count per unit area graph follows a logistic function trend giving an S-shaped (sigmoid) curve. As the nodule count goes from zero to infinity, TEmin follows; first an exponential-like path, then an almost linear trend followed by a logarithmic-like path.

The equation obtained from the data of EN-GJS-400-18 is given as;

$$TEmin = \frac{27.39}{1+exp[-0.012*(Nodule\ Count-394.02)]} + 1120.44$$

where TEmin is in ^{o}C, and Nodule Count is in 1/mm^2.

The equation obtained from the data of EN-GJS-600-10C is given as;

$$TEmin = \frac{26.36}{1+exp[-0.017*(Nodule\ Count-416.96)]} + 1123.18$$

where TEmin is in ^{o}C, and Nodule Count is in 1/mm^2.

These two correlations achieved by the regression analysis had satisfying r-square values such that 0.94 for the data of EN-GJS-400-18 and 0.89 for the data of EN-GJS-600-10C.

REFERENCES

1. G. Peter, D. B. Wagner, “Iron and Steel in Ancient China”, 1995, Bulletin de l’Ecole française d’Extreme-Orient, Volume 82: pp. 426 - 428.

2. ASM International, “ASM Metals Handbook”, 2008, Volume 15: pp. 1445 - 1484.

3. T. Elbel, J. Senberger, A. Zadera, J. Hampl, “Behavior of Oxygen in Cast Irons”, 2008, Archives of Materials Science and Engineering, Volume 33: pp. 111 - 116.

4. W. D. Callister, D. G. Rethwisch, “Fundamentals of Materials Science and Engineering an Introduction”, 2010, 8th Edition: pp. 391 - 450.

5. DIN EN ISO 945-1:2009, “Graphitklassifizierung durch visuelle Auswertung”, 2009, Mikrostruktur von Gusseisen.

6. Bundesverband der Deutschen Giesserei Industrie, “Gusseisen mit Kugelgraphit: Herstellung - Eigenschaften – Anwendung”, 2007, Duesseldorf.

7. American Foundry Society, “Modern Casting”, 2012, 47th Census of World Casting Production – Handbook: pp. 19.

8. J. Radzikowska, “Metallography and Microstructures of Cast Iron”, 2004, ASM Metal Handbook, Volume 9: pp. 565 - 587.

9. V. Anjos, C. S. Ribeiro, J. Cunha, C. Gomes, “The Use of Thermal Analysis to Compare Solidification Pattern and Evaluate Performance of Several Inoculants in SG”, 2014, 71st World Foundry Congress, Spain.

10. DIN EN ISO 1563-3:2012, “Gusseisen mit Kugelgraphit”, 2012, Giessereiwesen.

11. V. Anjos, “Use of Thermal Analysis to Control the Solidification Morphology of Nodular Cast Irons and Reduce Feeding Needs”, 2015, University of Duisburg, Germany.

12. R. D. Forrest, “What is the Optimum Base Iron Sulphur Content Prior to Nodularization?”, 2006, Sorelmetal Technical Service - Rio Tinto Iron & Titanium Inc.

13. G. M. Hansen, C. Hartung, D. White, “The Ductile Iron Treatment Process Revisited”, 2014, 71st World Foundry Congress, Spain.

14. P. Cabanne, “Magnesium Cored Wire Treatment Advantages and Disadvantages Vis-À-Vis Other Processes”, 2006, Sorelmetal Technical Service - Rio Tinto Iron & Titanium Inc.

15. J. R. Brown, “Foundryman's Handbook”, 2000, Foseco Ferrous, UK.

16. W. Baumgart, J. Cunha, V. Anjos, “Het Enten van Gietijzer”, 2010, Gietwerk Perspectief Magazine, Volume 5: pp. 5 - 12.

17. G. Lesoult, M. Castro, J. Lacaze, “Physical Modelling”, 1998, Solidification of Spheroidal Graphite Cast Irons – Acta Metallurgica, Volume 46, Issue 3: pp. 983-995.

18. W. Van der Perre: “Thermal Analysis of Cast Iron”, 2006, Heraeus Electro-Nite International – Handbook.

19. W. F. Smith, “Structure and Properties of Engineering Alloys”, 1993, McGraw Hill International: pp. 340.

20. J. Zhou, “Colour Metallography of Cast Iron”, 2009, China Foundry, Volume 6: pp. 57 - 65.

21. L. Svensson, A. Diószegi, K. Z. Liu, “Inoculation of Primary Austenite in Grey Cast Iron”, 2006, Science and Processing of Cast Iron, Volume 8.

22. D. M. Stefanescu, “Science and Engineering of Casting Solidification”, 2009, Springer Science + Business Media: pp. 1 - 4.

23. T. Skaland, F. Grong, T. Grong, “A Model for the Graphite Formation in Ductile Cast Iron”, 1993, Metallurgical Transactions, Volume 24: pp. 2321 - 2347.

24. D. D. Double, A. Hellawell, “The Nucleation and Growth of Graphite”, 1994, Modification of Cast Iron – Acta Metallurgica, Volume 43, Issue 6: pp. 2435 - 2442.

25. D. M. Stefanescu, “State of the Art in Solidification Modeling of Cast Iron”, 2006, Science and Processing of Cast Iron, Volume 8.

26. J. Zhou, S. Engler, W. Schmitz, “Formation of Austenite Shell around Nodular Graphite and its Effect on Deterioration of Graphite”, 1990, AFS Transactions, Volume 98: pp. 783 - 786.

27. W. Baumgart, “Untersuchung des Phasenübergangs von Flüssig nach fest am Tertiären System Fe-C-Si unter Nichtgleichgewichtsbedingungen”, 2013, Lehrstuhl für das Gesamte Giessereiwesen und Giesserei-Institut der RWTH Aachen, Germany.

28. C. R. Loper, R. W. Heine, M. D. Chaudhari, “Principles Involved in the Use of Cooling Curves in Ductile Iron Process Control”, 1974, AFS Transactions, Volume 82: pp. 431 - 440.

29. V. Anjos, W. Baumgart, J. Cunha, “Grundlagen der Thermischen Analyse”, 2014, Seminar in OCC GmbH - Metallurgishe Regelkreise, Mönchengladbach.

30. D. M. Stefanescu, “The Physical Metallurgy of Cast Iron”, 1985: pp. 151.

31. W. Baumgart, V. Anjos, “Thermal Analysis of Ductile Iron”, 2009, Seminar in OCC GmbH - Metallurgishe Regelkreise, Mönchengladbach.

32. I. G. Chen, D. M. Stefanescu, “Computer-Aided Differential Thermal Analysis of Spheroidal and Compacted Graphite Cast Irons”, 1984, AFS Transactions, Volume 92: pp. 947 - 964.

33. D. M. Stefanescu, “Thermal Analysis – Theory and Application in Metalcasting”, 2015 International Journal of Metalcasting, Volume 9: pp. 7 - 22.

34. R. Hummer, “Oxygen Activity of Ductile Iron Melts”, 1997, Advanced Materials Research: pp. 269 - 276.

35. T. Elbel, J. Senberger, A. Zadera, R. Vladik, “State of the Art of Metal Reoxidation Study of Iron Castings”, 2007, Archives of Materials Science and Engineering, Volume 11: pp. 649 - 652.

36. J. Hampl, T. Valek, P. Lichy, T. Elbel, “Control of the Metallurgical Processing of ICDP Cast Irons”, 2013, VSB Technical University of Ostrava, Czech Republic.

37. F. Mampaey, D. Habets, F. Seutens, “The Use of Oxygen Activity Measurement to Determine Optimal Properties of Ductile Iron during Production”, 2008, Foundry Research / Giessereiforschung, Volume 60, Issue 1: pp. 2 - 19.

38. Heraeus Electro-Nite International, "Oxygen Activity Measurement in Cast Iron", 2015, Celox Foundry – Handbook: pp. 1 - 3.

39. F. Seutens, “Thermal Analysis of Cast Iron – Improvements in Measurement Equipment”, 2017, Heraeus Electro-Nite International – Product and Application Training, Belgium.

40. OCC GmbH, “Micr-O-Phase – Image Analyzer”, 2008, Handbook, Germany.

41. L. Rao, W. Tao, S. Wang, M. Geng, G. Cheng, “Influence of the Composition Ratio of Manganese and Copper on the Mechanical Properties and the Machining Performance of Ductile Iron”, 2014, Indian Journal of Materials Engineering & Sciences, Volume 21: pp. 574 - 579.

42. OCC GmbH, “CSL – Regression Analysis Tool”, 2002, Handbook, Germany.

43. W. Stets, H. Löblich, G. Gassner, P. Schumacher, “Solution Strengthened Ferritic Ductile Cast Irons – Properties, Production and Application”, 2014, International Journal of Metalcasting, Volume 8, Issue 2: pp. 35 - 40.

44. Componenta Dokum A.Ş., “New Generation Ductile Irons”, 2014, 7th International Ankiros Foundry congress.